Friedrich-Alexander Universität
Erlangen-Nürnberg

Diplomarbeit

Pattern formation in a horizontally vibrated granular submonolayer

Dominik Krengel

am

Institut für Theoretische Physik I
und
Institut für Multiscale Simulation of Particulate Systems

January 26, 2012

Contents

Abstract

1995 führten Strassburger et al. [27] ein Experiment durch, bei dem sie eine Submonolage aus Teilchen horizontal schüttelten. Ihre Untersuchungen ergaben, dass sich Teilchen unter Einfluss des Schüttelns in Streifen anordneten. Um dieses Verhalten zu beschreiben, entwickelten sie ein einfaches zelluläres Automaten Modell: Während eines Stoßes springen alle Teilchen gleichzeitig in Stoßrichtung, bis sie auf einem linken und einem rechten Nachbarn zur Ruhe kommen. Experimentell lies sich das Springen jedoch nie beobachten, was vermuten ließ, dass die Streifenbildung eine andere Ursache hat.

Ziel dieser Arbeit ist, den Schlüsselmechanismus für Streifenbildung in einer horizontal geschüttelten Submonolage Teilchen zu identifizieren. Dazu wird das Experiment von Strassburger et al. wiederholt um den Effekt zu bestätigen. Basierend auf dem Experiment wird eine kraftbasierte Vielteilchensimulation durchgeführt, um gezielt das System zu untersuchen.

Es zeigt sich, dass Teilchen während der Simulation zwar springen können, dies jedoch nicht essentiell für ihre Streifenbildung ist. Als Grundlage für Streifenbildung lässt sich Reibung zwischen Teilchen identifizieren, die dazu führt, dass Teilchen in Kontakt nicht mehr frei rollen können, und sich zusammen mit dem Boden des Schüttelbehälters bewegen. Weiterhin findet sich, dass Streifenbildung nur bei höheren Anregungsamplituden, und geringeren Anregungsfrequenzen auftritt. Andere Kombinationen führen dazu, dass den Teilchen im System entweder nicht genügend Energie zugeführt wird um Streifen zu bilden, oder aber zu viel Energie bekommen und einen gas ähnlichen Zustand einnimmt.

Im Vergleich zwischen Experiment und Simulation zeigt sich, dass die im Experiment genutzten, nicht runden Teilchen, die nur eingeschränkt rollen können, zu deformierten Streifen führen, innerhalb derer die Teilchen quasi stationär sind. In der Simulation hingegen wurden perfekt runde Kugeln genutzt, und Streifen mit geringer Deformation erzeugt, innerhalb derer die Teilchen hohe Mobilität aufweisen.

Während der Vorbereitung der Simulation wurden Stöße dreidimensionaler Teilchen untersucht. Dabei ergab sich, dass der normale Restitutionskoeffizient negative Werte annehmen kann. Dieser Effekt war bereits für Hochgeschwindigkeits-Einschläge von Nanoteilchen bekannt [52]. Es lässt sich jedoch zeigen, dass dieser Effekt ein allgemeines Phänomen ist, das aus der Geometrie des Stoßes resultiert. Negative Restitutionskoeffizienten können für alle Arten von Kollisionen beobachtet werden, die von finiten Wechselwirkungskräften bestimmt werden.

1. Stratification in granular media

Granular media subjected to external agitation have a tendency to segregate, rather than to mix. This phenomenon is widespread in nature and is of enormous importance in industrial applications [79, 54, 40]. Used since millennia by peasants to separate chaff from grains or potatoes from earth, it is now widely used to sort materials in the mineral industry [36]. Segregation can be found for most types of mechanical agitation, like convection [38], hopper flows [29, 46, 7, 6] or flows in rotating drums [67, 44, 50]. One typical phenomenon associated with segregation of particles in granular media is the so-called "Brazil-nut effect", which consists of larger particles emerging on top of smaller particles when vertically shaken. Segregation can create interesting patterns, as for example a petal like structure in the centre of a binary mixture which is placed in a rotating drum [46].

1.1. Mechanisms of granular segregation [36]

The basic mechanisms of segregation are still not fully understood and subject of active research [47, 5, 35].
One type of segregation mechanism is called kinetic sieving [39, 4, 82]. In a shaken granular medium, voids between grains are constantly created, and smaller or heavier particles are more likely to fall into them than larger or lighter particles. This was shown by Rosato et al. [4] with a Monte-Carlo simulation of a vertically shaken box filled with mono-disperse disks and one large intruder near the bottom. After each vertical shake the system finds a new local equilibrium configuration by letting the individual particles move down- and sidewards. During this process voids between particles can appear, and voids below the large particles are likely to be filled with smaller particles, before the large particle returns to its initial position. Thus, the large particle gradually rises upwards.
A different explanation for the Brazil-nut effect based on granular convection was proposed by Knight et al. [38, 37, 93] in 1993. When the particles move up, they are compacted and frictional forces from the wall penetrate deep into the bulk of grains. When the particles move down again, the bulk is diluted and wall friction affects only particles close to the wall. This leads to a convective motion with larger particles being able to move up in the large channel in the centre. However, due to conservation of mass and symmetry of the convection cells, the channels on the side of the walls are smaller than the channel in the centre. Therefore, the large particles are not able to move down and get stuck on the top.
Dilute granular systems show different segregation mechanisms. Inelastic collisions can let the granular temperature vary across the system. The granular temperature T is defined [66] as the average kinetic energy of the particles

$$\frac{3}{2}T = \frac{1}{N}\sum_{i=1}^{N}\frac{1}{2}m\mathbf{v}_i^2, \tag{1.1}$$

where N is the number of particles, m the mass of the particle and $\mathbf{v}_i$ its velocity. Thermal diffusion of particles results from the temperature gradient, but diffusion

rates depend on particle properties like mass and size. This leads to large particles clustering in "cold" regions and small particles accumulating in "hot" regions [51, 11, 83].
Condensation of grains in a gravity field may also lead to granular segregation. For each species of particles, a critical temperature

$$T_c \sim M d^2 g, \tag{1.2}$$

can be introduced [14, 15], where M is the total mass of the gas per unit area at the bottom of the system, d is the particle diameter and g is gravity. Particles whose critical temperature is above the system temperature will condense on the bottom of the system, while particles with smaller critical temperature is below will not. Since larger or heavier particles have a higher critical temperature they condense first, thus creating a vertical segregation of particles.

1.2. Segregation in a rotating drum [36]

Motion of particles in a rotating drum, whose axis is perpendicular to the direction of gravity constitutes a topic of active research in the area of granular media [85, 36]. In fact, many applications related to mixing or milling of granular materials involve particle motion in a rotating drum.
If the materials in the drum slightly differ in physical or geometric properties, then axial or radial segregation effects can occur, which may pose a problem in situations where homogeneous mixtures are desired.

Segregation in radial direction

A drum filled with particles of two different radii or densities shows segregation in the radial direction [85, 47, 5]. The major factor for segregation is the so-called 'random fluctuating sieve', first described by Savage and Lun for particle flow on an inclined chute [82]: Small or heavy particles get stuck in the spaces between larger particles during their flow down the chute. A similar effect can be seen in rock slides, where large rocks are always found at the base of the avalanche. The maximum particle radius that can be trapped in a specific niche in an avalanche without momentum transfer was analysed by Baumann, Jánosi and Wolf [22]: if the radius of the rotating drum is sufficiently large, then every particle will find a niche that stops it. They observed in numerical simulations that large particles gather at the centre of the drum while small particles accumulate on the rim of the system, in less than one turn. Segregation in a rotating drum does not only occur if particles have different sizes, but also in mixtures of particles of different densities. After a short time, accumulation of dense particles in the centre of the drum can be observed [23].
At low rotation velocities the flow is confined to the free surface. The bulk shows solid-body rotation and transfers the particle distribution from the bottom to the top. A core is formed by small, heavy particles, surrounded by lighter, bigger grains. For

higher rotation velocities, the segregation pattern reverses: bigger particles assemble in the core while small particles remain in the periphery.
Depending on the initial conditions petal-like patterns appear at low rotation velocities (Fig 1.1).

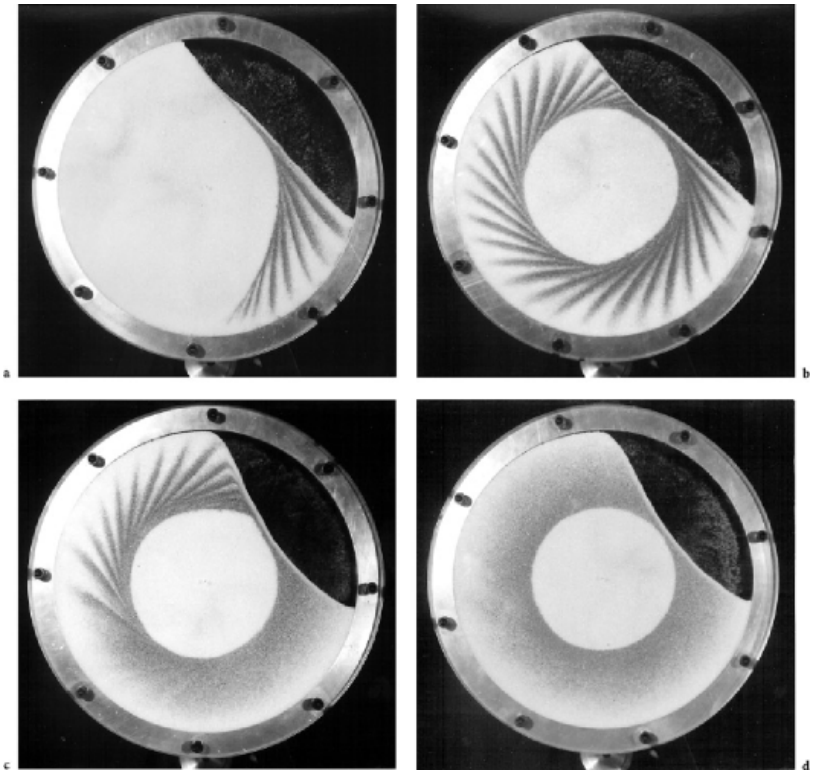

Figure 1.1.: Radial petal patterns in a rotating drum [46].

Segregation in axial direction

In 1939 Oyama described an experiment, in which axial segregation occurred in a three-dimensional drum [40].

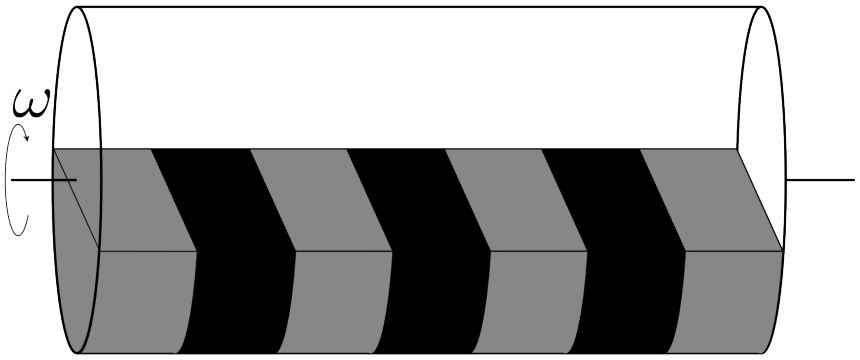

Figure 1.2.: Schematic view of Oyama's experiment after segregation has occurred.

His experiment consisted of a long cylindrical drum filled homogeneously with two types of grain of the same material, but of different sizes and colours. The cylinder was then rotated horizontally around its axis. Oyama observed that, at small rotational velocities, the small and the large beads arrange themselves in segregated stripes perpendicular to the rotation axis (fig 1.3).

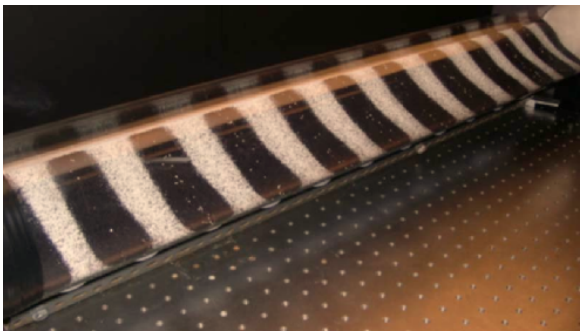

Figure 1.3.: Axial segregation in a rotating long drum [35].

The reason for this effect are the different angles of repose of the different species. Subsequent investigation by Savage [81] of systems with two different species of particles at high angular velocities showed segregation effects as well. These experiments showed that, at high rotation velocities, the angle of repose plays a minor role, as the material is in the flow regime. For low rotation rates no stable bands emerge, but smaller grains can assemble in irregular non-stationary "clouds" [36].
Stripes of different materials can merge into fewer, broader stripes, with the number of stripes decreasing or separating into more, smaller, stripes in time. The decay rate of the number of stripes $S(t)$ is basically independent of the rotation speed in the

range of $\omega \in [10, 22.5]$ rpm, and can be fitted with a logarithmic function,

$$S(t) = S_0 \left[1 - s \log \left(\frac{\omega t}{2\pi} \right) \right], \tag{1.3}$$

where $S_0 = 55$ and $s = 0.092$ are fitting constants [35]. Stripes may even completely disappear upon change of the angular velocity.

1.3. Stratification [36]

Granular stratification produces layered structures like those shown in figure 1.4. The layers appear in near surface flows of binary mixtures, like in sand piles or rotating drums [46, 28, 48], where particles differ in size and roughness, thus having different angles of repose. The main mechanism behind this phenomenon has been attributed to kinetic sieving in avalanches on the surface [81, 45]. During such an avalanche, voids open between particles in the flowing layer and smaller particles are more likely to fill these voids. This results in a net downward flux of small particles, which is compensated by an upward flux of larger particles to maintain a zero total particle flux across the flowing layer. Large particles roll on top of small particles, giving the avalanche the form of a rolling double layer. Upon reaching the bottom, the avalanche creates a kink, that stops the incoming particles and moves upwards to the top of the system. A double layer of small and large particles is then left behind (fig 1.4), after which a new avalanche forms, and the process begins anew.

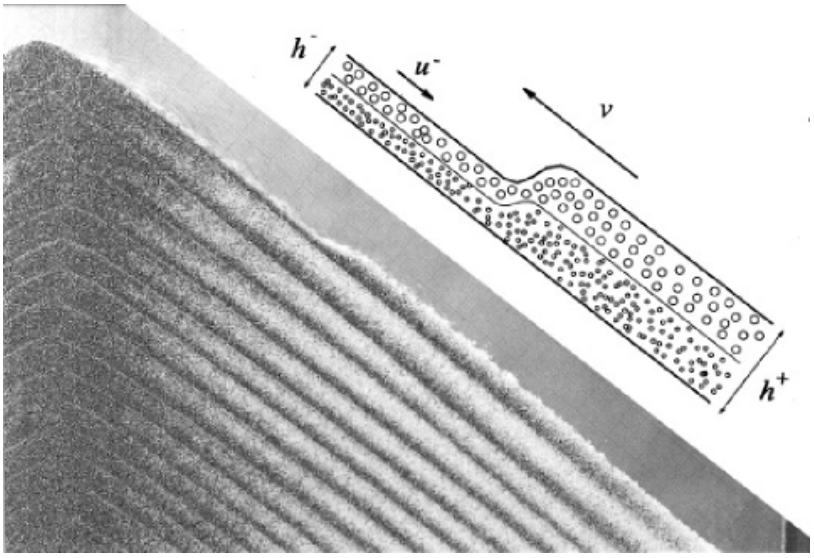

Figure 1.4.: Stratification in a granular avalanche [46].

2. Stratification in in a horizontal submonolayer

2.1. Horizontally vibrated granular media

Granular media can develop a rich variety of segregation patterns when subjected to horizontal shaking. Segregation effects of two- and three-dimensional horizontally vibrating granular systems have been reported both experimentally [84, 72] and in simulations [71, 73]. Simple models have been proposed to explain the physics behind the origin and evolution of the observed patterns [58, 12]. In experiments, agitation results from either shaking a tray, which serves as a substrate for an ensemble of particles, or oscillating a fluid, in which the grains are immersed [59].
Starting from an initially homogeneous state, a horizontally shaken binary mixture evolves into a pattern of segregated stripes perpendicular to the shaking direction (fig 2.1). Dry systems then display coarsening, diffusing the stripes due to the presence of tray noise, whereas wet systems reach a steady state since in this case adjacent stripes emerging in the system have enough space to oscillate without interacting [59].

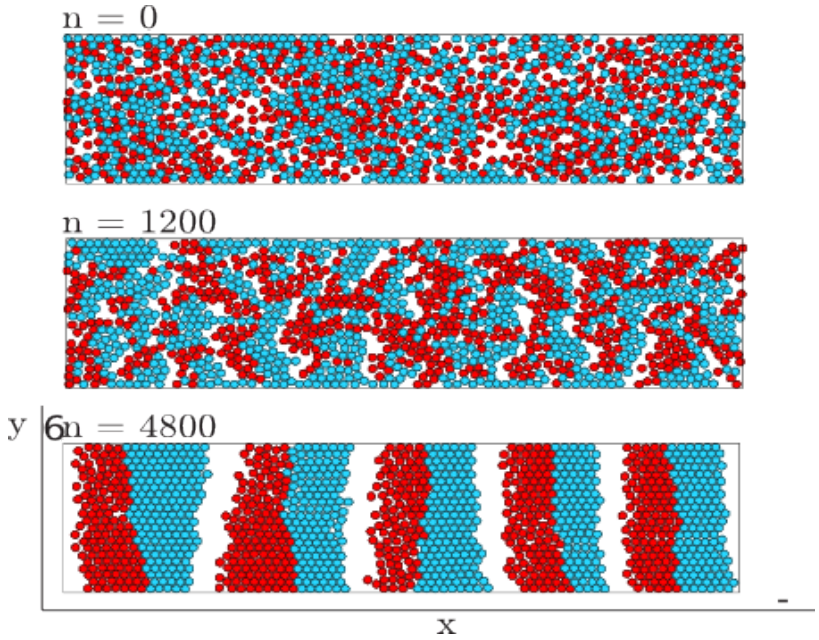

Figure 2.1.: Evolution of a binary mixture on a horizontally oscillating tray [59].

Ciamarra et al. investigated a binary mixture of large-heavy mono-disperse disks with an area fraction ϕ_h and small-light poly-disperse disks with area fraction ϕ_l. These authors found, that, when the system segregates into stripe patterns due to horizontal shaking, the light particles are always in a disordered configuration, resulting from their diversity, whereas the heavy particles can be found in ordered crystal-like configurations as well as in disordered fluid-like configurations. Furthermore, the authors found that the area fraction of the species is crucial for stripe formation: stripes form only for high enough concentrations (fig 2.2). Segregation into stripes appears at higher concentrations of particles. Increasing the concentration even further leads to crystallisation of the stripes. At sufficiently high concentrations the initial config-

uration jams, and the system assumes a glassy state. From their results, Ciamarra et al. concluded that the area fraction of the grains can be interpreted as an inverse temperature as the system moves from an disordered to a segregated state when the area fraction increases [59]. Further investigation by Reis and Mullin has shown that the segregation transition exhibits features of a continuous phase transition [72, 71].

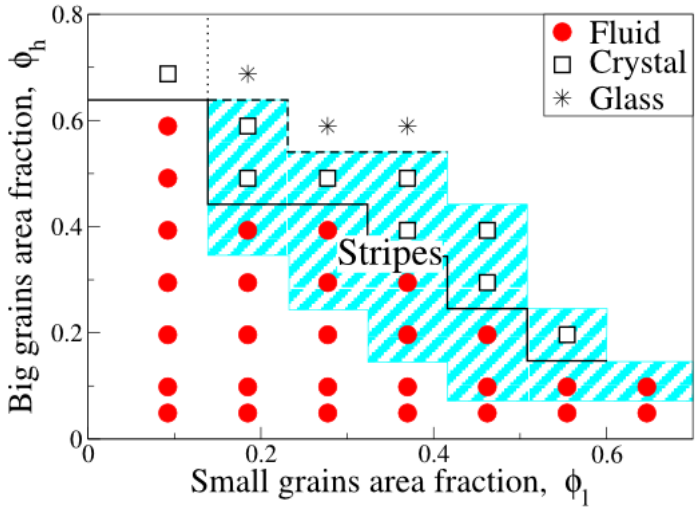

Figure 2.2.: State of a binary mixture as a function of the area fraction of the components [59].

Letting the binary system start from an ordered state in which the two components are separated into two bands, and subjecting it to horizontal oscillations, growing wavy patterns appear. Over time, this surface modulation leads to the evolution of alternating bands of segregated stripes (fig 2.3) [58].

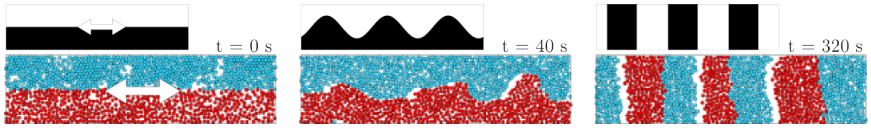

Figure 2.3.: Evolution of a mixture of heavy (red) and light (blue) particles subject to horizontal oscillation [58].

Each particle species is associated with a different characteristic time-scales and thus oscillates at different amplitudes and phases. The initially flat surface between the two components then develops surface modulations with growing amplitude, resulting in segregated stripes perpendicular to the driving direction [58].
Stripe formation in horizontally oscillated media not based on segregation was investigated by Strassburger et al. [27] using a tray filled with one to three monolayers of poly-disperse glass beads and shaking it horizontally. They observed ripple like patterns, perpendicular to the direction of motion, when the shaking frequency is lowered below a critical frequency (fig: 2.4).

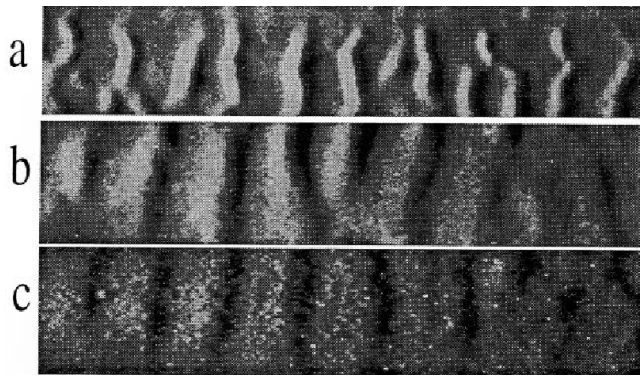

Figure 2.4.: Stripe formation in 3, 2, and 1 monolayers of grains under horizontal oscillation [27].

To describe this effect, they proposed a cellular automaton, based on all particles in the top layer simultaneously jumping in the same direction[1].
Segregation in an fluid immersed system was investigated by Sánchez et al. [77]. Their experiment consisted of a mixture of equal-sized glass and bronze spheres, fully immersed in a water filled tube, which was horizontally shaken. They observed, that, as the mixture became fluidised, the heavier bronze particles slowly sank to the bottom and accumulated there. These bronze rich regions at the bottom then slowly merged and formed stripes perpendicular to the direction of vibration. After a few minutes the entire system had separated into distinct regions of bronze spheres and regions of glass spheres (fig 2.5).

[1]This model is further explained in 3.1

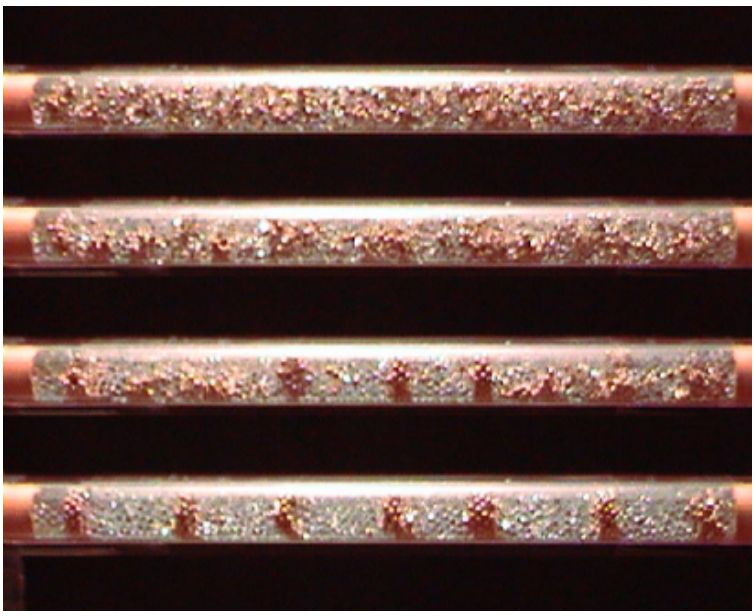

Figure 2.5.: Stripe formation in a horizontally oscillated fluid immersed granular mixture as observed by Sanchez et al. [77].

Using MD-simulation Sánchez et al. showed, that the stripe forming mechanism is closely related to that of fluid-driven separation in vertically vibrated granular mixtures [77, 63, 62]. Based on these results a microscopic separation mechanism was proposed. Its two key features are: (1) the container vibration drives the fluid back and forth through the system, (2) the two components of the mixture are differently affected by the fluid. Consequently one species will move with respect to the other and is dragged out of regions rich with particles of the other species. Clusters of same particles have little tendency to break apart as they are moved in the same way by the fluid. This process repeats until a stable configuration is reached [77].

2.2. Experimental investigation of a horizontally vibrated submonolayer

Based on the experiment by Strassburger et al. [27], a granular submonolayer, subjected to horizontal oscillation, is investigated experimentally. The behaviour of the bulk of grains is recorded and its density field is calculated. During the observation, the system reveals the formation of stripes which merge in the course of time into bigger clusters. This effect is robust enough with respect to the forcing, that it appears even when the container is shaken by hand.

2.2.1. Setup

The experiment consists of a horizontal, smooth aluminium tray of dimensions $(x, y, z) = 500 \times 100 \times 50\,\mathrm{mm}^3$ (fig 2.6, 2.7a and fig 2.7b), in which the grains are vibrated horizontally. The tray is mounted on a OSP-E linear driver by Origa Systems Plus, powered by a stepper motor, whose amplitude and frequency of the sinusoidal movement can be controlled via a PC.

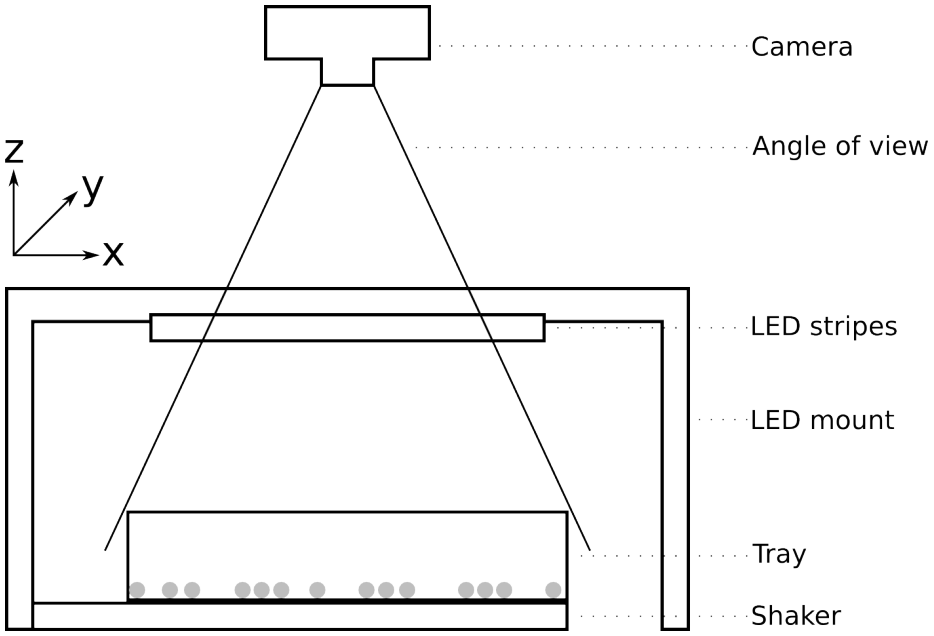

Figure 2.6.: Sketch of the setup.

The motor controller is connected with a camera to allow phase triggered image recording. The motion of the shaker is unidirectional in x and sinusoidal. After the initial fluidisation (section 2.2.5), amplitude and frequency are kept constant during the experiment. Images are recorded with a Luminera Lucam-camera mounted above the tray (fig 2.7d). The tray is filled with a sub-monolayer of mustard seeds with an average diameter of $(2.14 \pm 0.22)\,\mathrm{mm}$.

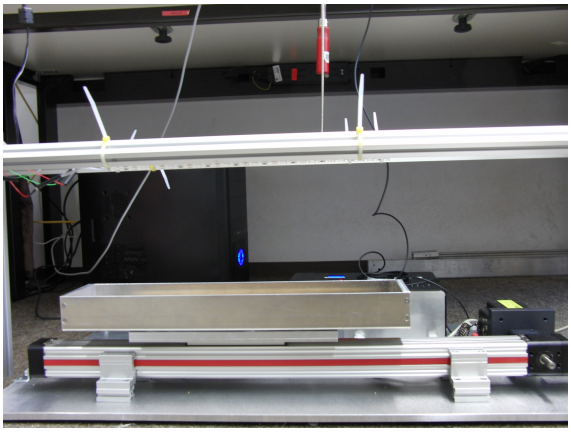

(a) Side view

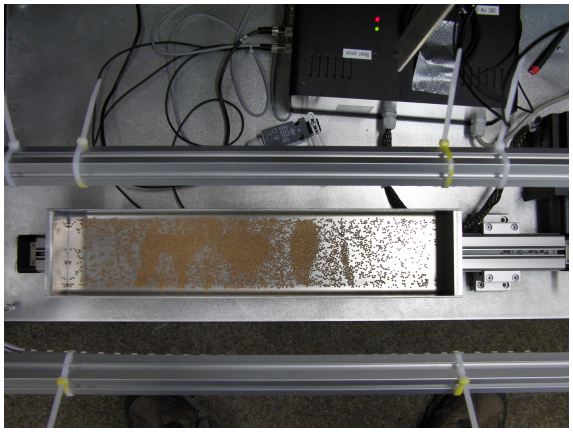

(b) Top view

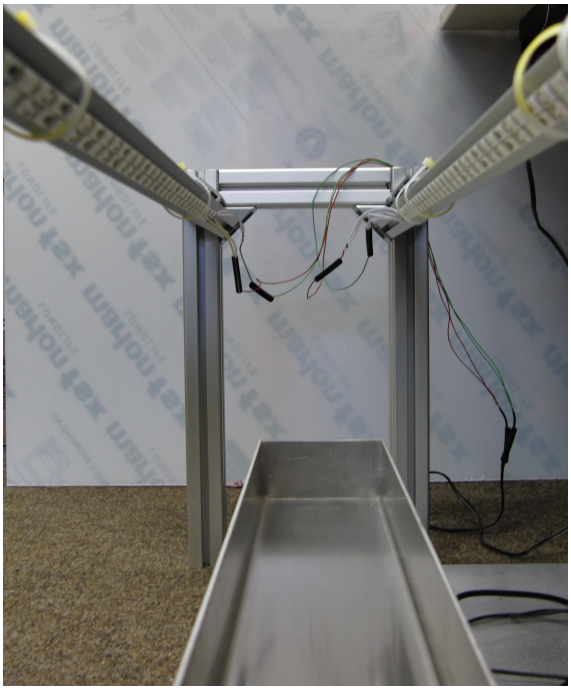

(c) LED mount

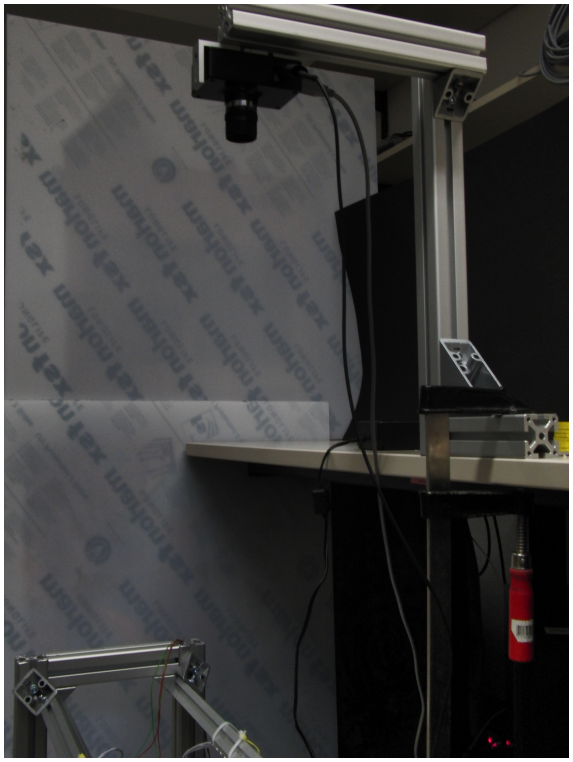

(d) Camera mount

Figure 2.7.: Setup of the experiment. Figure (a) shows the apparatus from the side, figure (b) from the top, figure (c) the illumination of the experiment and figure (d) the camera position in the experiment.

2.2.2. Image acquisition

Image acquisition is done by a Luminera Lucam 125C Camera mounted top down above the experiment (fig 2.7d). The maximum resolution of the camera is 1280×1024 pixels. The camera has a hardware I/O-interface, which serves as an input for an external trigger signal from the shaker. The camera is equipped with a lens with a focal length of 16 mm. The field of view is chosen such that the entire length of the box at one of its reversal points can be observed. Images are taken in bitmap format, converted into grayscale and cropped to only include the area within the tray. A background image is created by averaging over 30 sample images taken with the experiment running without grains.

2.2.3. Illumination

The experiment is illuminated with four 45 cm long red LED stripes, mounted on metal bars parallel to the long sides of the box (fig 2.7c), and with a maximum luminous flux of 400 lm. This arrangement was chosen to evenly illuminate the tray.

2.2.4. Material

About 4800 mustard seeds are used as grains (fig 2.8). The number of particles has been determined by filling a box with length 12.5 cm and width 6.6 cm and dividing the resulting volume by the average volume of the particles.

Figure 2.8.: Small sample of the mustard seeds used in the experiment.

To filter out particles with high deviations in form or size, a Grimm-type [41] manual sorting mechanism is used. The average diameter of the grains is $\overline{d} = 2.14 \pm 0.22$ mm calculated from the diameter of 20 randomly selected seeds. The diameters are determined by measuring the longest axis of the particle with a slide gauge.

Table 2.1.: Measured diameter of the mustard seeds in mm

Particle	1	2	3	4	5	6	7	8	9	10
diameter d [mm]	2.32	2.04	1.85	2.30	2.42	1.80	2.23	2.36	2.17	2.34
	11	12	13	14	15	16	17	18	19	20
	2.12	2.11	2.53	1.90	1.79	2.15	2.34	2.19	1.85	2.05

2.2.5. Experimental method and image processing

The particles are placed inside the tray and manually stirred until they appear homogeneously distributed. The apparatus is then set into motion with a driving frequency of 5 Hz and an amplitude of 2 cm. This fluidises and further homogenises the system. Image recording is started and shaking frequency and amplitude are lowered to 3 Hz and 1 cm. Images are recorded at a framerate of about 3 images per second for one hour after which the experiment is stopped.
The recorded images are read as grayscale matrices in Matlab. From these matrices the grayscale matrix of the background image is subtracted to remove the background and only the particles remain (fig 2.9).

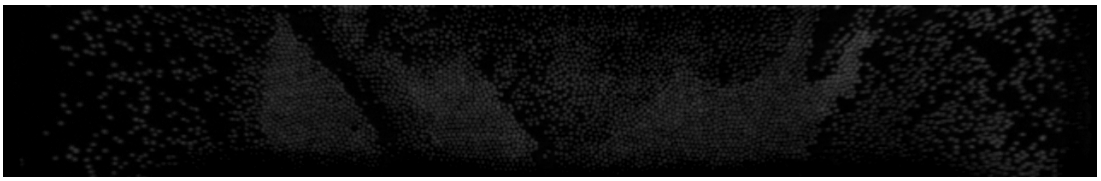

(a) The image as recorded.

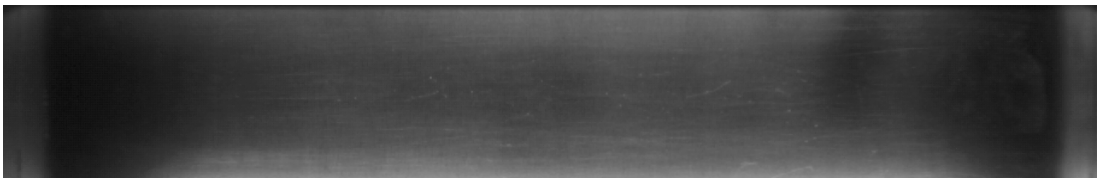

(b) The averaged background image.

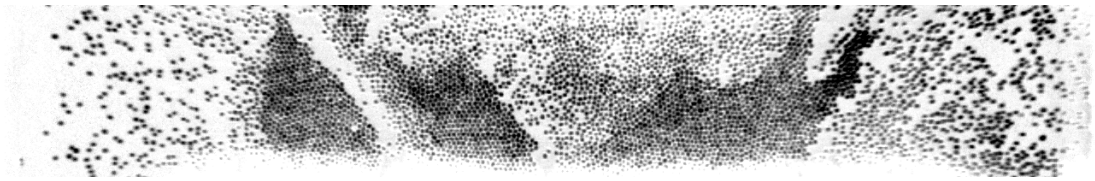

(c) After subtracting the background only the particles remain in the image.

Figure 2.9.: An example of image processing. At first the image (2.9a) and background (2.9b) are recorded. Then the background is subtracted from the image (2.9c). For clarity the colours of the last image are inverted.

The columns of the resulting matrix, representing the width y of the system, are averaged to create a vector containing the brightness distribution of the image in

x-direction (fig 2.10). With the assumption that brighter spots represent a higher density of the seeds, the resulting vector contains the density profile of the system.

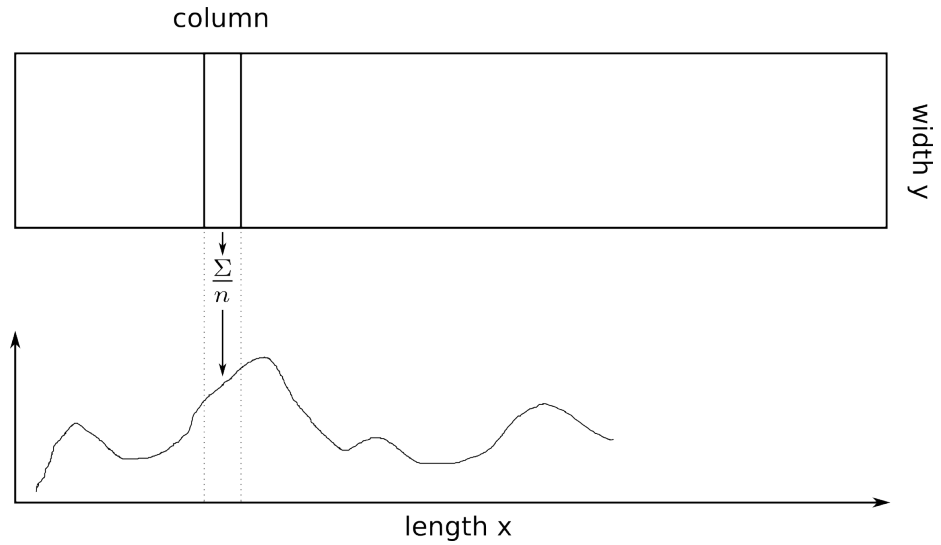

Figure 2.10.: Sketch of Evaluation procedure.

Since the LED-stripes are shorter than the box, the sides of the box are less illuminated than the centre. This leads to a brightness gradient, which is visible in the images of the experiment as brighter areas in the left and right sides of the pictures.

2.2.6. Observation

Short term: Formation of stripes

During the first 60 seconds of the experiment, images are taken every 25 ms (fig 2.12). The camera exposure is set to 4.0 ms. The initially homogeneous distribution (2.12(a)) shows formation of irregular clusters in the central area of the box after about 1 second (2.12(c)). During the next seconds more clusters appear over the whole box (2.12(e)) approximately equally distanced from each other, and begin to merge into stripes perpendicular to the direction of shaking, until the system shows distinct stripes (2.12(g)-(j), 2.11).

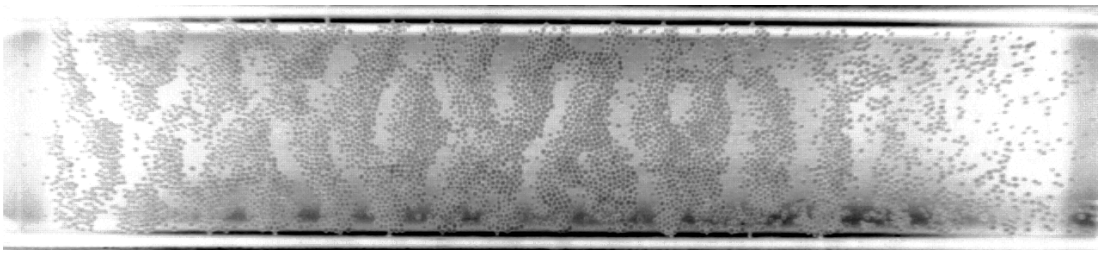

Figure 2.11.: Clearly distinguishable stripe patterns after 10 seconds. For clarity, the image is presented with inverted colours.

The particles in the cluster appear to be static relative to the bottom plate, while the particles outside the stripes are very active. The mustard seeds used in the experiment have flattened sides. If they come to rest this can lead to a higher amount of energy being required to get them moving again compared to round objects. Likewise if two seed touch each other with their flat surfaces their rotational and translational freedom will be more constrained than two spheres in contact, again leading to an increased jamming rate. At no point, the particle were observed to jump over each other.

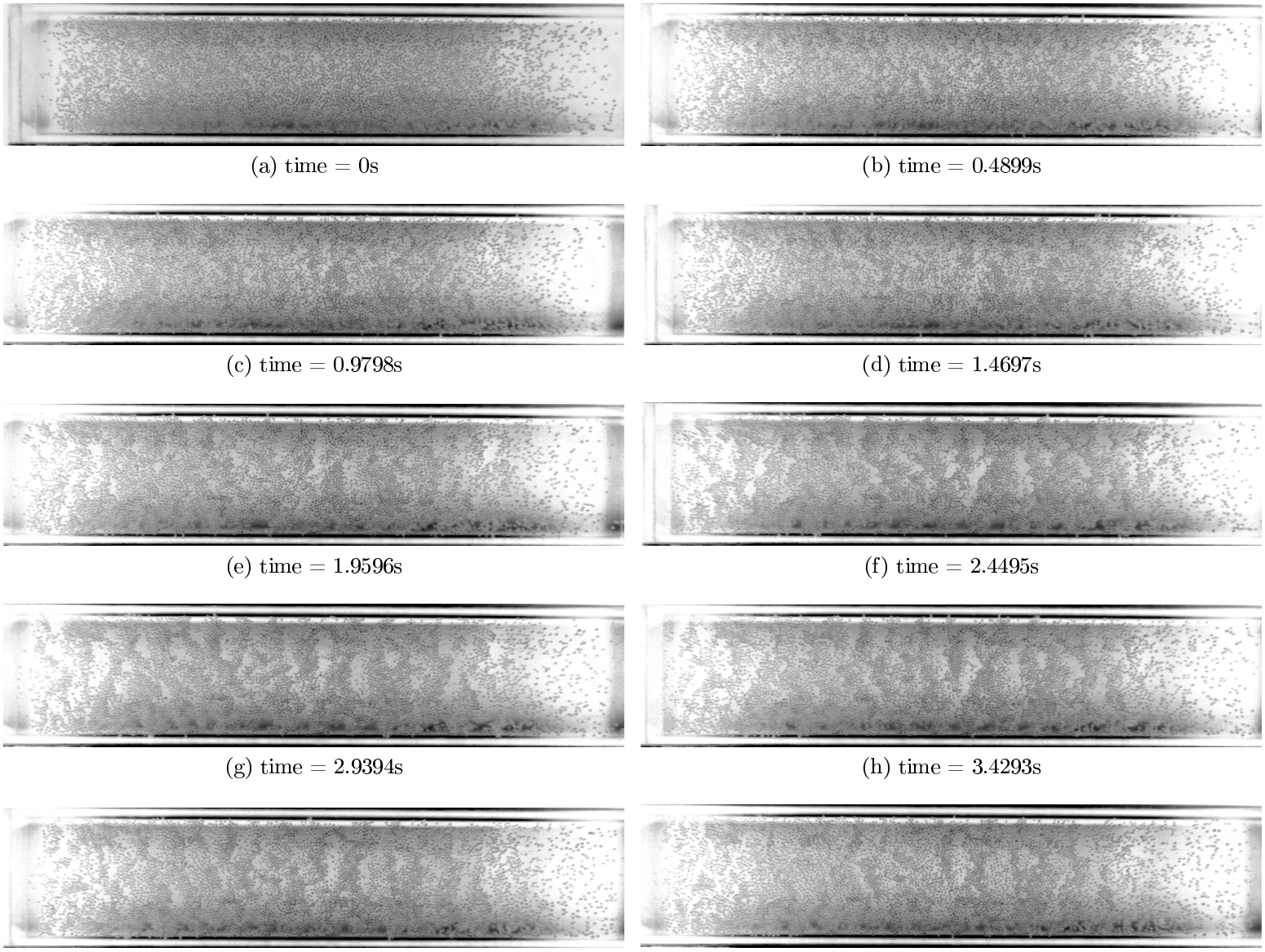

(a) time = 0s (b) time = 0.4899s

(c) time = 0.9798s (d) time = 1.4697s

(e) time = 1.9596s (f) time = 2.4495s

(g) time = 2.9394s (h) time = 3.4293s

(i) time = 3.9192s (j) time = 4.4092s

Figure 2.12.: The first five seconds during the experiment showing the initial stripe formation out of a homogeneous distribution. For clarity, the images are presented with inverted colours.

A single phase

After stripes have emerged and stabilised (50 seconds), a single phase of oscillation is investigated. Figure 2.13 shows that the stripes themselves remain stable in position, but particles not belonging to any stripe move with relative velocity with respect to the stripes, similar to particles in a gas.

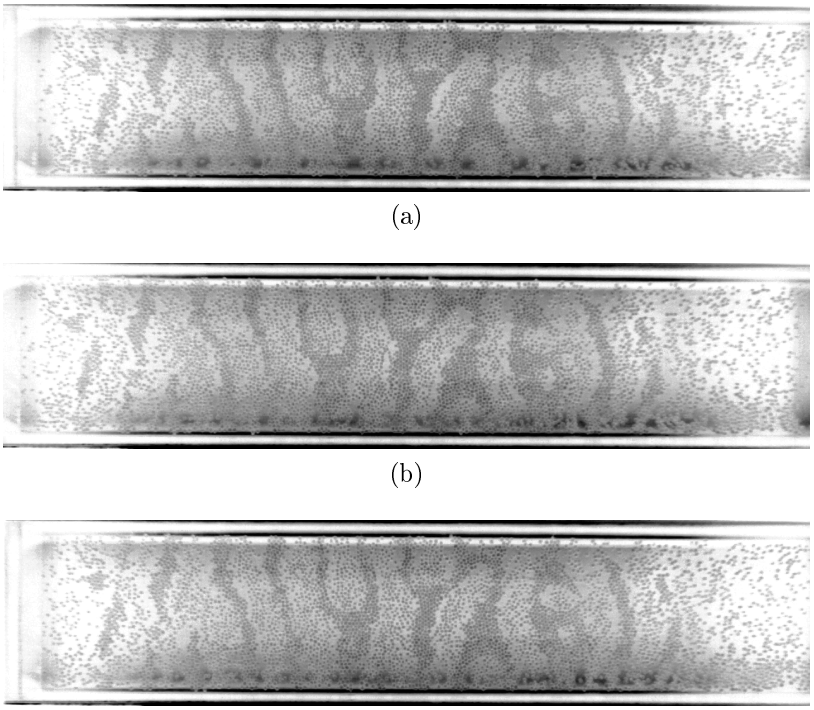

(a)

(b)

(c)

Figure 2.13.: Behaviour of the system during a single phase of shaking. For clarity, the images are presented with inverted colours.

Furthermore, it can be seen, that, when reverting the direction (fig 2.13(b)), particles on the sides of the stripes facing the incoming wall can leave the stripes to join the free particles in-between (fig 2.14). Free particles beyond the stripes can be caught by these and join the stripes (fig 2.14).

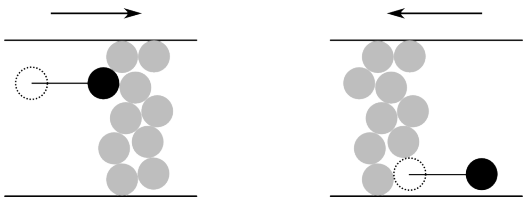

Figure 2.14.: On the left side, the particle is captured by the stripe. When reverting the direction, the particle is released from the stripe, as shown on the right side.

Long term behaviour of stripes

Images are recorded for one hour at every second turning point of the shaker. Exposure is set to 11 ms. During the experimental run, the system transforms from an initially homogeneous state into stripes. The system begins with many stripes and then gradually reduces the number of stripes. In the right and left hand sides of the system (between $x = 0.0\,\mathrm{m}$ and $0.1\,\mathrm{m}$ and between $x = 0.4\,\mathrm{m}$ and $0.5\,\mathrm{m}$) the particles try to form in stripes, but fail due to agitation from the walls. However, it is observed that the stripes at $x = 0.1\,\mathrm{m}$ and $0.4\,\mathrm{m}$ absorb parts of the free particles (e.g. at 2400 seconds). The density profiles (figures 2.16) show, that the system starts with about 12 stripes which after about 100 seconds are reduced to 9 stripes, then after 1400 seconds to 5 stripes and finally after 3400 seconds to 4 stripes. Comparing the recorded images with the density field, it shows, that the form of the stripes changes when stripes merge, and stretched amorph accumulations appear(fig 2.15b). These deformed accumulations may show up as multiple stripes in density, but actually are connected. Particles formerly belonging to those stripes are released as free particles again, moving between the deformed stripes and the side walls. During the first 200 seconds all stripes move about 5 cm in the direction of shaking, but remain effectively stationary from then on. At 1400 seconds it is observed that two smaller stripes merge into one bigger stripe. Another effect that is observed, for example at 3200 seconds, is that stripes can fall apart again and distribute their particles over a larger area.

(a) after 0 seconds

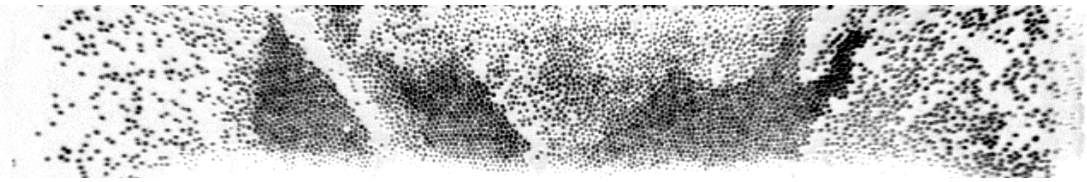

(b) after 3600 seconds

Figure 2.15.: The particle distribution after 0 seconds and after 3600 seconds. It is clearly seen, that the stripes become distorted. For clarity, the images are presented with inverted colours.

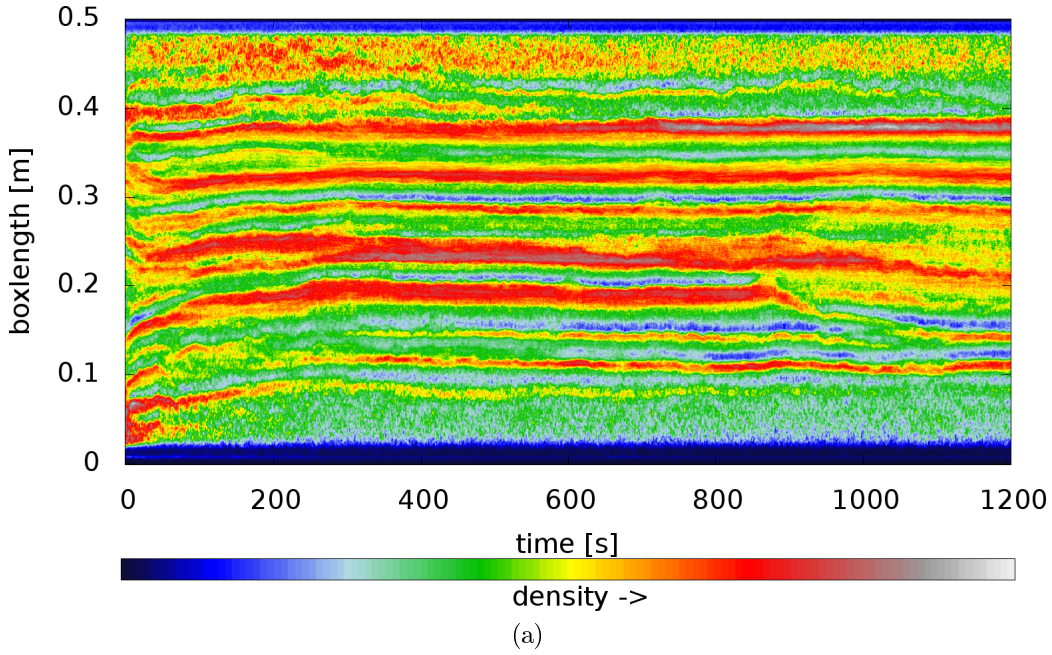

Figure 2.16.: Density evolution of the experiment during one hour. For clarity the plot has been split into three pieces.

3. Modelling

3.1. A cellular automaton model [27]

To model the dynamics in shallow horizontally shaken sand, Strassburger et al. created a simple cellular automaton. This model consists of two rules, applied to the top layer of the medium to describe the evolution of the system from time T_n to time T_{n+1}:

1. Simultaneously every particle in the top-layer flies alternatively to the left or to the right until it contacts with another particle.

2. Particles fall until they come to rest on a left and a right neighbour.

These rules are illustrated in figure 3.1.

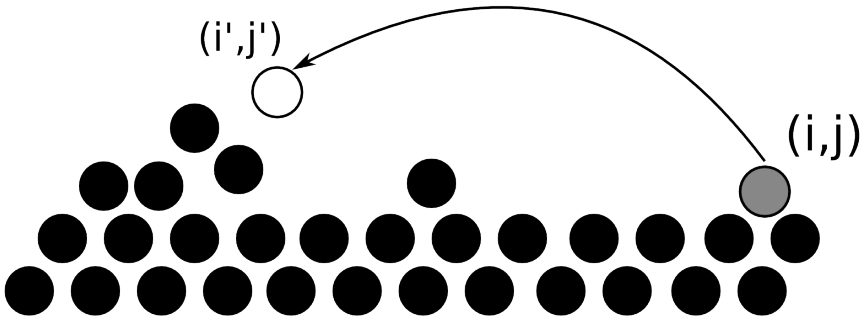

Figure 3.1.: Illustration of the idea of the cellular automaton.

First step: The quasi-simultaneous flying phase At the beginning of each iteration $\mathcal{I}$, two identical matrices $\widetilde{L}$ and $\widetilde{M}$ hold the positions of all particles in the system. The matrix $\widetilde{L}$ remains unaltered and is used to test if any particles collide during the flying phase.

Second step: The resting phase Element $\widetilde{M}_{ij}$, which corresponds to the starting position (i, j) of the particle currently watched, is decremented and element $\widetilde{M}_{i'j'}$ of the new position (i', j') is incremented. The new configuration $\mathcal{I}+1$ is calculated and $\widetilde{L}$ is updated: $\widetilde{L} = \widetilde{M}$

Here, the indices of the elements represent the location of the particles in the model. The values of the elements indicate the height of the pile of grains above the initial surface.

3.2. Particle Simulation

3.2.1. Idea of Molecular Dynamics Simulations

Granular systems consist of large numbers of particles, that ideally interact only via short ranged mechanical contacts[1]. The system dynamics are determined by Newtons equation of motion for the centre-of-mass coordinates and the Euler angles of the particles:

$$\frac{\partial^2 \mathbf{r}_i}{\partial t^2} = \frac{1}{m_i}\mathbf{F}_i(\mathbf{r}_j, \mathbf{v}_j, \boldsymbol{\phi}_j, \boldsymbol{\omega}_j) \tag{3.1}$$

$$\frac{\partial^2 \phi_i}{\partial t^2} = \frac{1}{\hat{I}_i}\mathbf{M}_j(\mathbf{r}_j, \mathbf{v}_j, \boldsymbol{\phi}_j, \boldsymbol{\omega}_j) \tag{3.2}$$

$\mathbf{F}_i$ and $\mathbf{M}_i$ are the force and the torque acting on particle i with mass m_i and tensor of inertia $\hat{I}_i$.
In the absence of long-ranged interactions $\mathbf{F}_i$ and $\mathbf{M}_i$ are determined by the sum of pairwise interaction forces acting on particle i:

$$\mathbf{F}_i = \textstyle\sum_{j\neq i} \mathbf{F}_{ij} \tag{3.3}$$

$$\mathbf{M}_i = \textstyle\sum_{j\neq i} \mathbf{M}_{ij} \tag{3.4}$$

If the forces $\mathbf{F}_{ij}(\mathbf{r}_i, \mathbf{r}_j, \mathbf{v}_i, \mathbf{v}_j, \boldsymbol{\phi}_i, \boldsymbol{\phi}_j, \boldsymbol{\omega}_i, \boldsymbol{\omega}_j)$ and the torques $\mathbf{M}_i(\mathbf{r}_i, \mathbf{r}_j, \mathbf{v}_i, \mathbf{v}_j, \boldsymbol{\phi}_i, \boldsymbol{\phi}_j, \boldsymbol{\omega}_i, \boldsymbol{\omega}_j)$ are given, the equations of motion can be integrated numerically.

3.2.2. Forces

The most simple model of a particle is a sphere with a radius R. Particles in contact can then be identified if the sum of their radii exceeds the distance of their centres:

$$\xi_{ij} = R_i + R_j - |\mathbf{r}_i - \mathbf{r}_j| > 0, \tag{3.5}$$

where ξ_{ij} is called overlap or compression of particles i and j with radii R_i, R_j and positions $\mathbf{r}_i$ and $\mathbf{r}_j$.
The force acting between i and j then is described by

$$\mathbf{F}_{ij} = \begin{cases} \mathbf{F}_{ij}^n + \mathbf{F}_{ij}^t & \text{if } \xi_{ij} > 0 \\ 0 & \text{otherwise} \end{cases} \tag{3.6}$$

Normal Forces

Heinrich Hertz first described the interaction force of elastic spheres as a function of deformation ξ and material parameters Young modulus Y and Poisson ratio ν [30]:

$$F_{\text{el}}^n = \frac{2Y\sqrt{R_{\text{eff}}}}{3(1-\nu^2)}\xi^{3/2}, \tag{3.7}$$

[1]For sufficient small particles long ranged interactions like electrostatics may play a significant role.

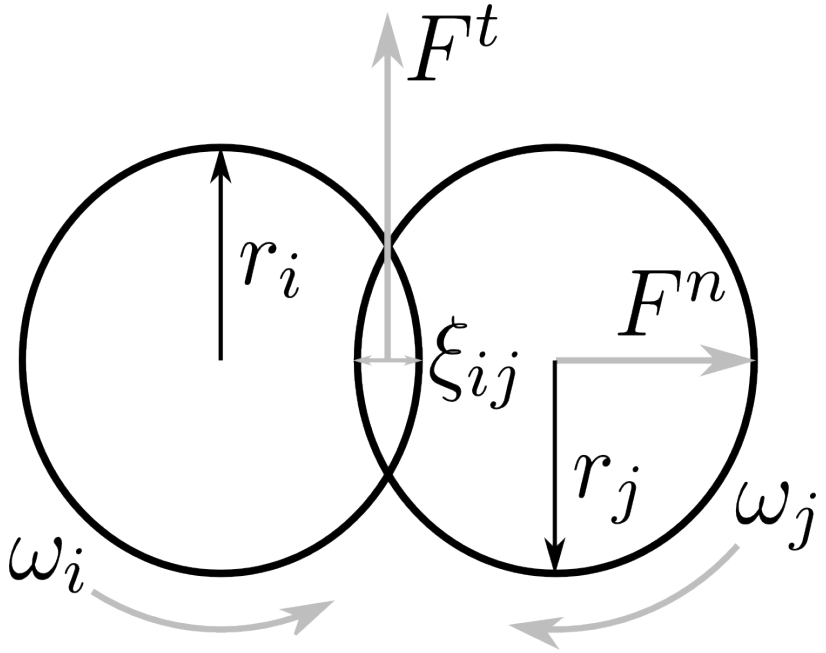

Figure 3.2.: Two-dimensional illustration of the forces acting on particle i in contact with particle j.

where $R_{\text{eff}} = \frac{R_i R_j}{R_i + R_j}$ is the effective radius of the colliding spheres.
A generalised form, including viscous damping parameter A, was found later [64]:

$$F^n = \frac{2Y\sqrt{R_{\text{eff}}}}{3(1-\nu^2)}(\xi^{3/2} + A\sqrt{\xi}\frac{\mathrm{d}\xi}{\mathrm{d}t}) \tag{3.8}$$

Here, A is a function of the material viscosity. In case that the colliding particles are of different materials, the collision force has to be adjusted to fit the different parameters using the arithmetic mean of the individual parameters:

$$A \to \frac{1}{2}(A_i + A_j) \tag{3.9}$$

$$\left(\frac{1-\nu^2}{Y}\right)^{-1} \to \left(\frac{1-\nu_i^2}{Y_i} + \frac{1-\nu_j^2}{Y_j}\right)^{-1} \tag{3.10}$$

Tangential Forces

Modelling tangential forces relates the resulting force on the particles to their relative tangential surface velocities v_{rel}^t at the point of contact. However, since the model for the normal forces assumes a deformation of the particles, the point of contact is only an approximation and the tangential forces are inconsistent with the normal forces. For hard enough particles the deformation becomes sufficiently small compared to the radii of the particles so that this inconsistency can be ignored.

The point of contact thus is defined as the intersection of the undeformed surface of sphere i with the vector $\mathbf{r}_{ij}$ connecting the centres of the spheres $\mathbf{r}_{ij} = \mathbf{r}_i - \mathbf{r}_j$. The relative tangential velocity at the point of contact consists of the relative tangential linear velocity and the contribution of the particles' rotation:

$$v_{\text{rel}}^t = (\mathbf{v}_i - \mathbf{v}_j)\mathbf{e}_{ij}^t + (R_i\mathbf{e}_{ij}^t \times \boldsymbol{\omega}_i + R_j\mathbf{e}_{ij}^t \times \boldsymbol{\omega}_j). \tag{3.11}$$

Using the model by Haff and Werner [70], the tangential force then can be written as:

$$F^t = -\text{sgn}(v_{\text{rel}}^t)\min\left(\gamma^t \left|v_{\text{rel}}^t\right|, \mu\left|F^n\right|\right), \tag{3.12}$$

where γ^t is the tangential damping coefficient, and μ the Coulomb friction parameter. For small relative velocities v_{rel}^t or large normal forces F^n, the tangential force is a linear shear damping that grows with the relative velocity. It is limited by Coulomb's friction law:

$$\left|F^t\right| \leq \mu\left|F^n\right|. \tag{3.13}$$

Since the tangential force is determined by surface properties of the particles, there is no experimentally measurable material constant from which γ^t could be derived. It can only be determined á posteriori from comparison of simulation results and experiments. Furthermore, this model does not include static friction, since the relative velocities v_{rel}^t at the point of contact and, hence F^t vanish. It is therefore only valid for dynamic systems.

3.2.3. Friction forces

Friction forces are dissipative forces, that appear if two bodies in contact move relative to each other. Two different kinds of frictional forces are distinguished: sliding friction and rolling friction [53]. If friction is neglectable during sliding, the surface is called totally smooth, if only pure rolling without sliding is possible and friction is neglectable, then the surface is called totally rough.

Sliding Friction

Sliding friction occurs when two bodies in contact slide relative to each other. It is described by the Coulomb friction law

$$\mathbf{F}_{\text{fr}} = -\mu_s F_\perp \mathbf{e}_v, \tag{3.14}$$

where μ_s is the material-dependant friction coefficient and $F_\perp$ the magnitude of the force acting between the sliding bodies. The friction force counteracts the sliding motion of the bodies.

Rolling Friction

Pure rolling is characterised, in that no relative motion exists at the point of contact, i.e. rolling bodies are fixed in their point of contact at any moment in time [53]. Rolling friction leads to an additional torque that counteracts the rolling motion. According to Brilliantov and Pöschel [65] the friction torque for a viscoelastic particle is given by

$$\mathbf{M}_i = -\mu_r v_{\omega,ij} F^n \mathbf{e}_{\omega_i}, \tag{3.15}$$

where $\mathbf{e}_{\omega_i} = \frac{\boldsymbol{\omega}_i}{\omega_i}$, F^n is the normal force acting between the particles and $v_{\omega,ij}$ is the magnitude of the relative tangential velocity resulting from the relative angular velocity ω_{ij} at the point of contact $v_{\omega,ij} = |\omega_i \times \mathbf{R}_i - \omega_j \times \mathbf{R}_j|$. μ_r, the coefficient of rolling friction, is a function of the material parameters and is given by [65]:

$$\mu_r = \frac{1}{3}\frac{(3\eta_j - \eta_i)^2}{(3\eta_j + \eta_i)^2}\left[\frac{(1-\nu^2)(1-2\nu)}{Y\nu^2}\right] \equiv A, \tag{3.16}$$

which can be identified with the dissipative constant A for two colliding spheres.

3.2.4. Boundaries

Walls

Rough walls can be modelled out of regular particles that follow a predetermined trajectory and do not interact with each other. The roughness of the surface can be controlled by the size of the wall particles and their distance to each other.

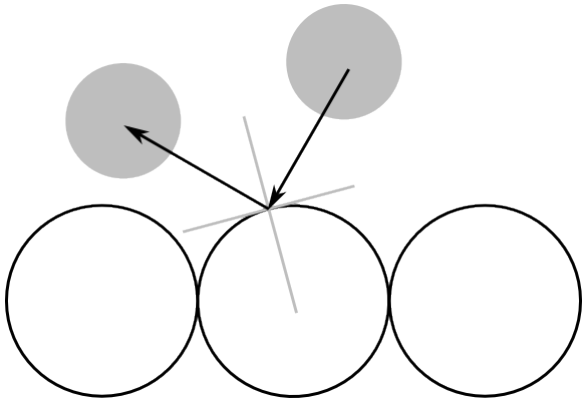

Figure 3.3.: 2D-example of an impact on a rough wall.

Smooth walls are defined by an origin $\mathbf{r}_{\text{wall}}$, a surface normal $\mathbf{n}_{\text{wall}}$, and a velocity $\mathbf{v}_{\text{wall}}$. They can be imagined as particles with an infinite radius $R_{\text{wall}} = \infty$, therefore the effective radius becomes $R_{\text{eff}} = R_{\text{particle}}$. Particle-wall collision are then modelled with equations 3.8 and 3.12, where

$$\xi = R_{\text{particle}} - (\mathbf{r}_{\text{particle}} - \mathbf{r}_{\text{wall}}) \cdot \mathbf{n}_{\text{wall}} \tag{3.17}$$

$$\dot{\xi} = (\mathbf{v}_{\text{particle}} - \mathbf{v}_{\text{wall}}) \cdot \mathbf{n}_{\text{wall}} \tag{3.18}$$

Since this method does not need to store information about particles creating the wall, it is faster than the previously discussed method. As the collision is central collision in any case, the walls are always smooth.

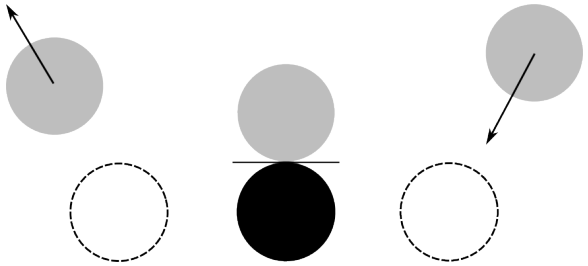

Figure 3.4.: 2D-example of an impact on a smooth wall.

Periodic boundary conditions

To mimic larger systems periodic boundaries are used in the x-direction and, in some cases, in the y-direction as well.
Particles are contained inside a box, and those who leave the box are inserted on the opposite side of the central area again, effectively giving the system a toroidal structure. For the force summation, particles on one boundary of the system also interact with particles on the opposite side of the system.

3.2.5. Duration of Collisions

For an undamped binary collision, its duration can be estimated via the time $\tau^0_{\max} \approx 1.609$, that it takes the particles to reach their maximal compression [89], The total duration of the undamped collision then is $\tau^0_c = 2\tau^0_{\max}$ in reduced units. Transforming back to unscaled units, one obtains [89],

$$t = \frac{\tau^0_c}{\frac{\zeta}{m_{\text{eff}}}^{2/5} v^{1/5}}, \tag{3.19}$$

where $\zeta = \frac{2Y\sqrt{R_{\text{eff}}}}{3(1-\nu^2)}$ and v is the impact velocity of the particles
For a damped collision, the equation of motion for the deformation ξ reads

$$\ddot{\xi} + \frac{\zeta}{m_{\text{eff}}}\xi^{3/2} + \frac{\zeta A}{m_{\text{eff}}}\sqrt{\xi}\dot{\xi} = 0. \tag{3.20}$$

An analytical solution for the contact time of equation 3.20 exists [89],

$$\tau_{\max} = \tau^0_{\max} + \sum_{k=1}^{\infty} a_k \beta^k v^{k/5}, \tag{3.21}$$

but is rather complicated. In the following four figures equation 3.20 is solved numerically for different material parameters.

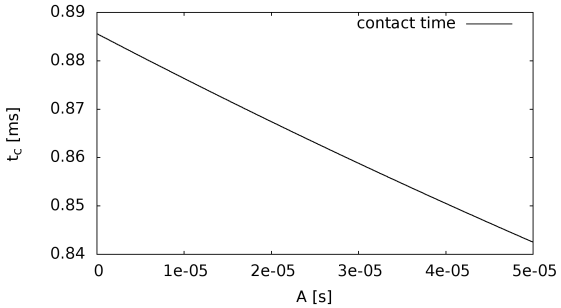

(a) $r = 0.0005\,\mathrm{m}$; $Y = 1e^6\,\mathrm{kg/(ms^2)}$; $v = 0.002\,\mathrm{m/s}$

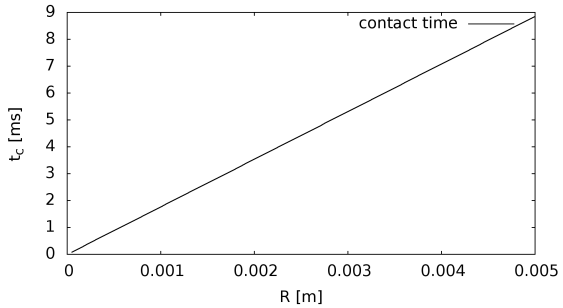

(b) $A = 8.5e^{-6}\,1/\mathrm{s}$; $Y = 1e^6\,\mathrm{kg/(ms^2)}$; $v = 0.002\,\mathrm{m/s}$

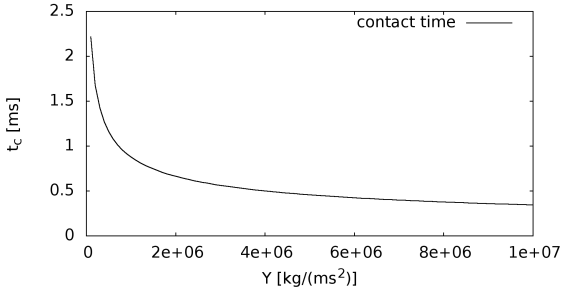

(c) $A = 8.5e^{-6}\,1/\mathrm{s}$; $r = 0.0005\,\mathrm{m}$; $v = 0.002\,\mathrm{m/s}$

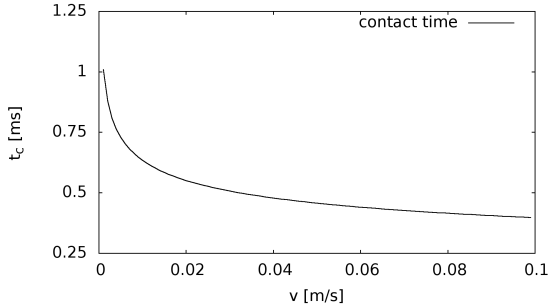

(d) $A = 8.5e^{-6}\,1/\mathrm{s}$; $r = 0.0005\,\mathrm{m}$; $Y = 1e^6\,\mathrm{kg/(ms^2)}$

Figure 3.5.: Dependence of the contact time t_c on dissipation A (a), radius r (b), Youngs modulus Y (c) and impact velocity v (d).

It shows, that the dissipative parameter has weak influence on the contact time of the collision, compared to Youngs modulus and impact velocity. The contact time increases with bigger radius of the collision partners.

3.3. One Particle System

The ripple like patterns, observed in the experiment 2.2 and by [27], are the result of the collective behaviour of many particles. To properly identify the underlying reason for stratification, understanding of the behaviour of a single particle is required. This section describes how the behaviour of a single sphere on an oscillating plane is influenced by its material parameters by means of a molecular-dynamics simulation.

Coordinate system

The coordinate system in these and all following simulations is as aligned follows (fig 3.6).

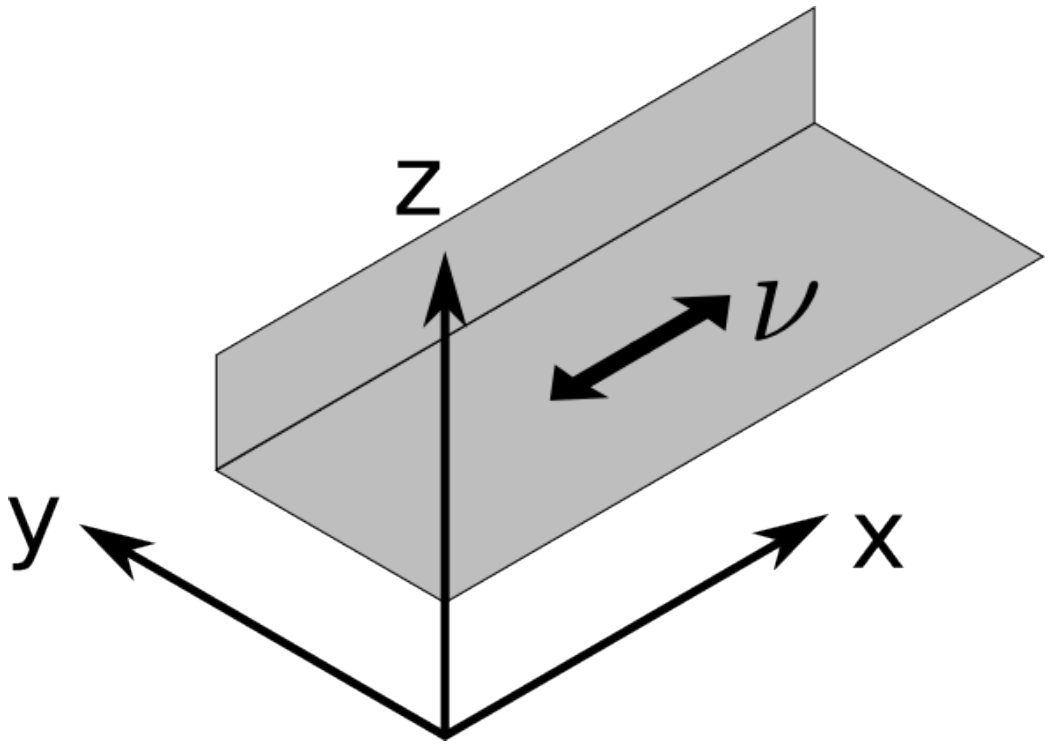

Figure 3.6.: Orientation of the coordinate system used in all simulations. To visualise the interior of the tray only one wall is shown in the figure.

The plane in which the motion takes place is the x-y-plane. The x-direction is parallel to the direction of shaking, the y-direction is perpendicular to this direction. Perpendicular to both x- and y-direction is the z-direction, to which gravity is parallel. The bottom of the system extends from the (0,0,0) in positive (x,y,0)-direction. All further mentions of x,y, and z refer to this coordinate system.

Material properties used in the simulation

Table 3.1 shows the parameters that are used to simulate the motion of a single particle. In all cases, walls and particle have the same parameters.

Table 3.1.: Parameters used in the simulation.

Name	Value
radius r	$0.0005\,\mathrm{m}$
density ϱ	$2500\,\mathrm{kg/m^3}$
Youngs Modulus Y	$10^6\,\mathrm{kg/(ms^2)}$
Normal dissipation A	$8.5 \cdot 10^{-6}\,\mathrm{s}$
Friction parameter μ_{pp}	0.7
Rolling friction μ_r	$8.5 \cdot 10^{-6}$
Tangential damping γ_t	0.007
Gravity $\mathbf{g}$	$-10\mathbf{e}_z\,\mathrm{m/s^2}$
timestep Δt	$8 \cdot 10^{-6}\,\mathrm{s}$

Since the motion of the box only occurs in x-direction, and there are no other forces acting in the y-direction, the phase space positions are given by the x-coordinate of the particle. The shaking amplitude is kept constant at $\mathcal{A} = 0.025\,\mathrm{m}$, and the shaking frequency is varied between $\nu_{\min} = 5\,\mathrm{Hz}$ and $\nu_{\max} = 29\,\mathrm{Hz}$.

3.3.1. Results

Due to high sliding friction, the particle will immediately start to roll. Sliding contact then only occurs for a short time when the particle reverses its motion.

Single particle without rolling friction

The coefficient of rolling friction is set to zero, $\mu_r = 0$, allowing the particle to roll indefinitely. It can immediately be seen, that the mean trajectory of the particle does not change with shaking frequency, but the particle fluctuates faster around its mean with increasing frequency (fig 3.7a). The velocity of the particle follows closely the velocity of the container, but is significantly lower, due to loss of energy from sliding friction and conversion of the linear velocity into angular velocity (fig 3.7b). Plotting the phase space of the particle motion shows periodic orbits (fig 3.8a), increasing in size with higher shaking frequency. Likewise, the particle energy increases (fig 3.8b), with the particle assuming maximum velocity midway between two reversal points of the container motion, and then decelerating due to the decelerating of the box.
Increasing the mass of the test particle by changing its radius with constant density results in the particle reacting slower to change in the agitation force, in accordance with the laws of inertia (fig 3.9).

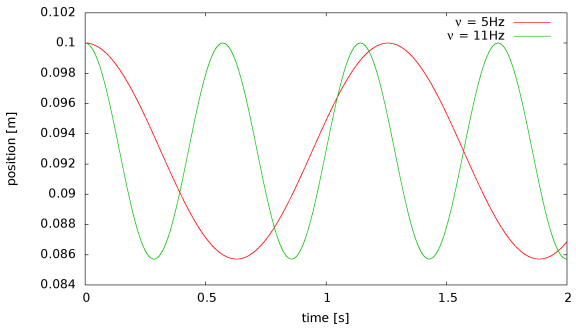

(a) Position without rolling friction

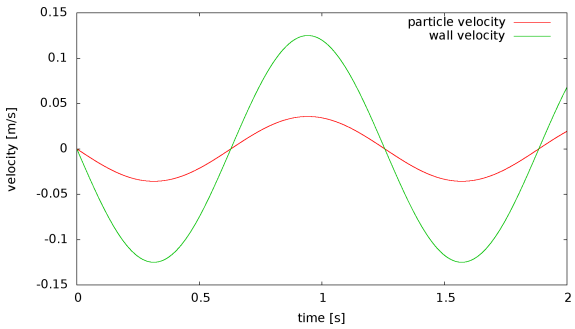

(b) Velocity without rolling friction

Figure 3.7.: (a): particle position for different shaking frequencies; (b): particle velocity compared to floor velocity at 5 Hz.

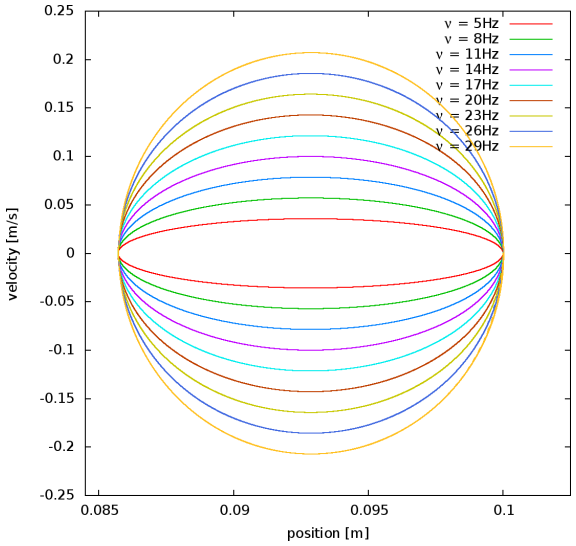

(a) Phase space

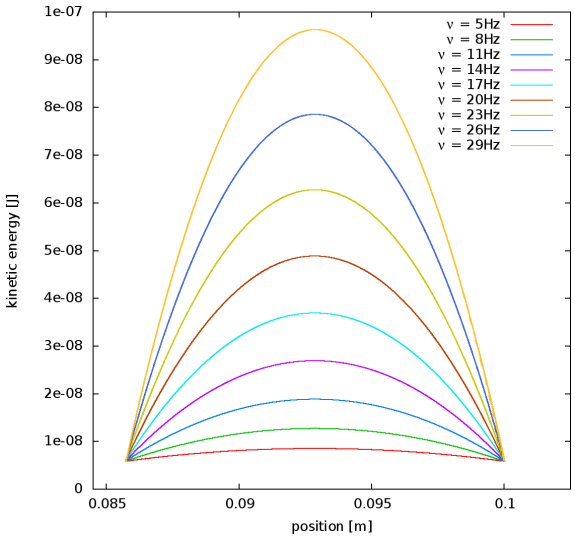

(b) Energy space

Figure 3.8.: Phase space and energy trajectories for a single particle on a horizontally shaken surface with different shaking frequencies.

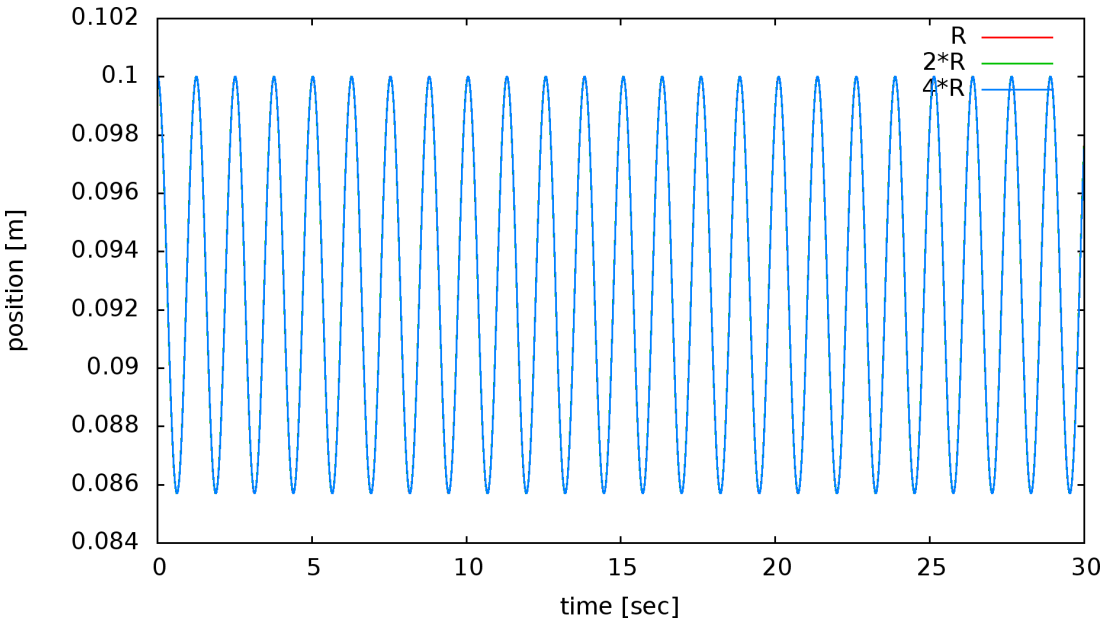

(a) Change of position

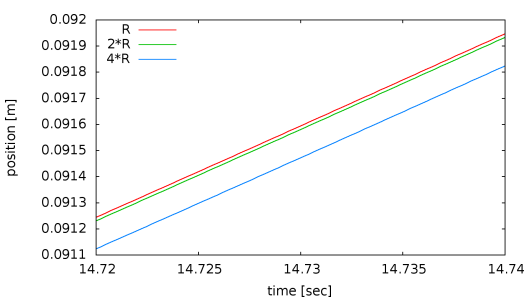

(b) Ascending part

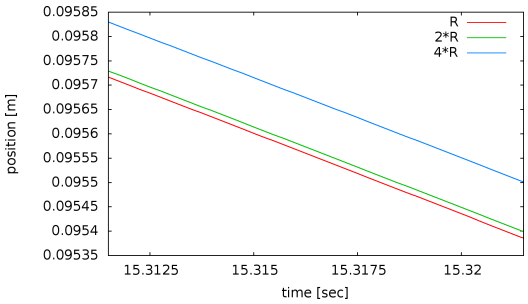

(c) Descending part

Figure 3.9.: Change of position of the particle with different masses and magnification of the ascending and descending parts of one oscillation period.

Single particle with rolling friction

Allowing rolling friction in the system slightly alters the behaviour of the particle.

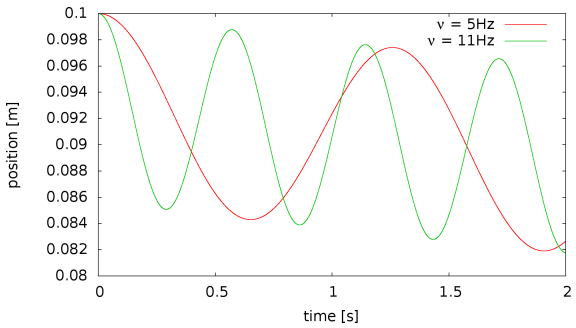

(a) Position with rolling friction

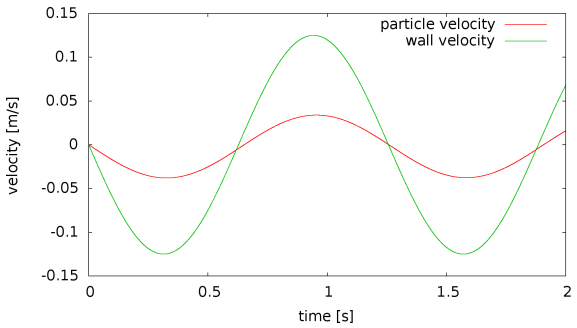

(b) Velocity with rolling friction

Figure 3.10.: Figure (a): particle position for different shaking frequencies; figure (b): particle velocity compared to floor velocity at 5Hz.

The particle is no longer trapped between two points in space, but moves into the direction of the initial trust, slowly approaching a stable position (fig 3.10a). This movement is caused by the inertia of the particle, that the agitation first has to overcome. Compared with the experiment, the round particle can move more easily, and thus overcome inertia earlier than the grains in the experiment. The shaking frequency of the box shows no influence on the mean trajectory of the particle, for different frequencies the particle follows the same path, only changing the speed by which it oscillates around the mean trajectory. Like the frictionless case, the velocity follows the container velocity, at a lower amplitude (fig 3.10b).
The phase space diagram shows, that the particle moves on a helical trajectory with decreasing change in position between two successive phases, approaching a stable orbit (fig 3.11a). Likewise the energy parabola moves along the space axis of phase space into a stable configuration (fig 3.11b).

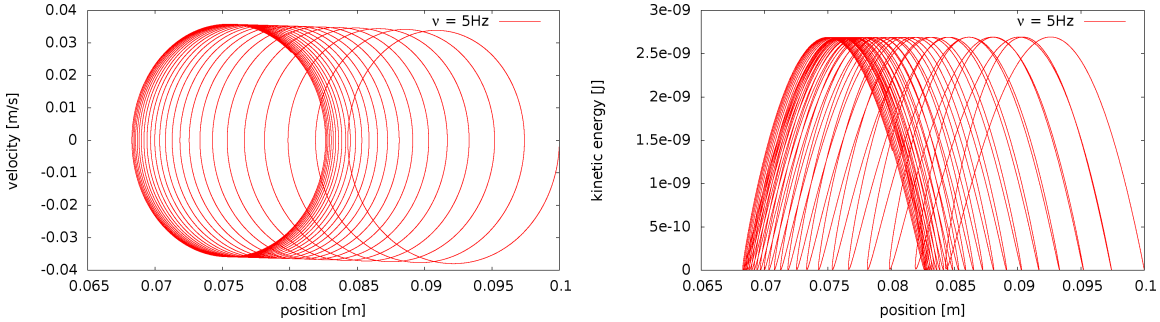

(a) Phase space trajectory for a single agitation frequency

(b) Energy space trajectory for a single agitation frequency

Figure 3.11.: Phase space trajectories for a single particle with rolling friction on a horizontally shaken surface.

Varying the frequency results in the particles following helical trajectories[2]. Increasing the agitation frequency increases the motion of the trajectories in velocity direction (fig 3.12), but leaves the motion in space-direction unchanged. All agitation frequencies lead to the particles approaching stable configurations in the same phase space region.

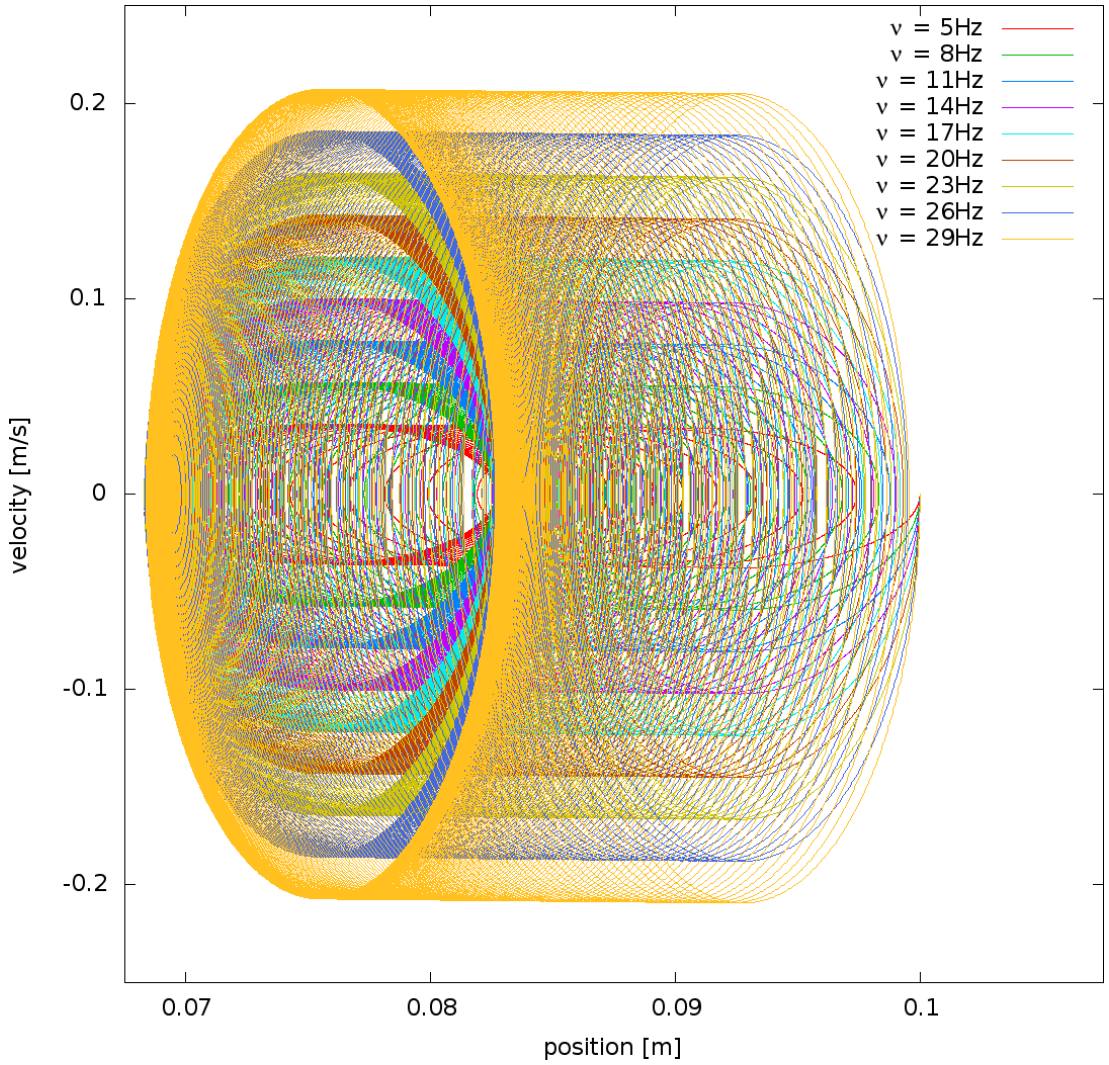

Figure 3.12.: Phase space trajectories for a single particle with different shaking frequencies.

[2]compare fig. 3.11a for the trajectory of a single agitation frequency.

3.4. Frustration effects for rolling particles [18]

Granular media in motion show a strong dissipative character mainly caused by normal and tangential damping. Inter-particle friction plays an important role, as it causes hysteresis phenomena like stick-slip. If three particles are in mutual contact, then at least one particle has to slide due to frustration by geometric constraints. The rotational modes of the particles organise in such a way, that frictional resistance causing the frustration is reduced [26, 42].

3.4.1. 1D-System

For an 1D array of closed packed hard cylinders, confined by horizontal forces at the ends of the chain and moving with constant acceleration $\dot{v}$ on a horizontal plane (fig 3.13) this effect was first studied by Radjai and Roux [21, 95, 26].

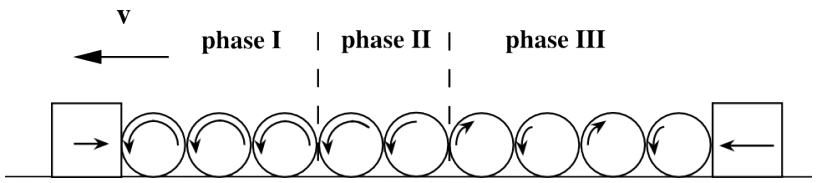

Figure 3.13.: Three phases in a one-dimensional array [95, 21].

The particles can roll or slide on the surface and are constrained on both sides with blocks, that can only slide. This array is pushed to the right. The constraints prevent the opening of contacts between any two cylinders, and the pushing force is chosen small enough, that all cylinders stay in contact with the floor. If all contacts are non-sliding, there will be no dissipation in the system. However, since the system is frustrated, at least one contact per particle has to slide. As example, consider two cylinders in contact with each other and the floor. If one cylinder is rotating clockwise with angular velocity ω, the other one has to rotate counter-clockwise with angular velocity $-\omega$. If then one of the cylinders is rolling on the plane with a velocity $\mathcal{V} = \omega R$, the other is forced to slide with a relative tangential velocity of $\mathcal{V}_t = 2\mathcal{V}$, which constricts its motion.
Radjai and Roux [21] found that the rotational modes organise themselves into three different domains, whose lengths depend on the horizontal acceleration, the applied horizontal stress and the frictional forces [21]. The domains are characterised as follows:

- In domain 1, the particles roll with an angular velocity corresponding to the imposed velocity, $\omega = \frac{R}{v}$. Here, friction stress on particle-plane contacts is activated and particle-particle contacts are sliding.

- Domain 2 is characterised by sliding contacts. Particles roll in the same direction as in domain 1, but with decreasing angular velocity along the array. In the

special case of constant translational velocity $\dot{\mathcal{V}} = 0$, mode 2 has vanishing length.

- Domain 3, next to the forcing block, contacts between particles are non-sliding, with neighbouring particles either counter-rotating or not rotating at all.

Later work by Khidas et. al. showed [95], that mode 2 can be described as a superposition of modes 1 and 3.

3.5. 3D Simulation of a horizontal submonolayer

To better understand the underlying mechanism of the pattern formation observed in the experiment (Section 2.2), the system is reproduced in a force-based molecular dynamics simulation. These systems are first run with three-dimensional dynamics, normal dissipation and particle-particle friction activated and limited in the $\pm y$-direction by walls, and then with various parameters deactivated. The system is found to no longer form clusters, once inter-particle friction is deactivated, suggesting that the dominant mechanism for stripe formation is jamming of particle-particle contacts, which results in the jammed particle getting locked to the floor and moving as pair until the motion of the floor is reversed and differences in experienced forces separate the particles again.
The first part of this section reviews the method used to create the simulation and introduces concepts to improve computational efficiency. The resulting program is then verified and conservation laws are checked. The third subsection details how the samples used in the simulations are prepared and gives an overview of the physical properties of the particles. The last part presents the results obtained in the simulations.

3.5.1. Simulation method [87, 43]

General Method

The simulation is a forced-based molecular dynamics simulation, that means, the particles are only influenced by the forces acting on them. The simulation is performed according to the following algorithm (fig 3.14):

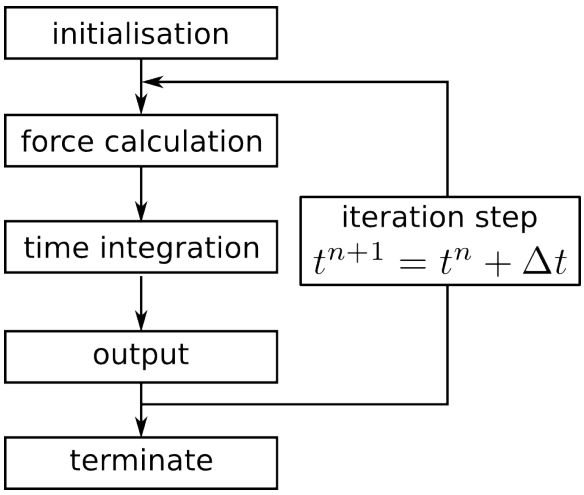

Figure 3.14.: graphical representation of the MD algorithm.

1. **Initialisation:**

(a) Read the coordinates ($\mathbf{r}_i$ and the derivatives) and material properties of the particle from an initialisation file.

(b) Read external parameters like the simulation time from a configuration file.

2. **Force calculation:**

   (a) Find interaction pairs.

   (b) Calculate the interaction force for all particles in contact.

   (c) Calculate the forces between the particles and the system walls.

3. **Time integration:**
   Calculate the new positions based on the forces acting on the particles.

4. **Output:**
   Write all phase space properties of the system into a file for later evaluation.

5. **Program termination:**
   The program is terminated after a predetermined time $t_{\text{Simulation}}$ or upon occurrence of a certain event. Otherwise the simulation is continued at step 2.

Force calculation

Forces that act on particles can either be long-ranged like gravitation, short-ranged like intermolecular forces or contact forces. Short ranged forces are usually modelled as long ranged with a cut-off radius after which their influence is neglected. To determine the total force acting upon any particle, it has to be checked which other particles lie within its influence radius. Particles that influence each other then exchange forces. The total force on one particle is the sum of all individual interactions plus the contribution from globally acting forces.
The simulation used in this work does not include ranged forces other than gravitation, particle interaction happens only via direct mechanical contact as given by the force laws in Section 3.2.2.

Numerical Integration of the Equations of motion [10]

The dynamics of the particles in the system are described by differential equations with initial values, the trajectories are determined by integrating the equations of motion. The standard methods to solve the integrals are finite-difference methods, which replace infinitesimal differentials like dx and dt with small but finite differences Δx and Δt, the differential equations become finite-difference equations. These finite-difference equations then can be processed by a computer to approximately solve the original integrals.
A variety of methods for numerical integration exists. The following subsections discuss the two methods that are used in this simulation in detail. For the linear motion of particles the advanced Verlet-algorithm is used, as it is the cheapest (lowest

order) algorithm while already considering second derivatives, that is available for dissipative systems. Additionally to the position it only requires the second derivative of the position. Due to the non orthogonality of the second derivatives in the rotation coordinates, using a second order integrator becomes complicated. This complexity is avoided by using the more simple Euler algorithm instead of the Verlet algorithm.

Euler Integrator The Euler integration method [43] is a Taylor expansion truncated after the first-order term

$$\mathbf{r}(t+\Delta t) = \mathbf{r}(t) + \Delta t\dot{\mathbf{r}}(t) + \mathcal{O}(\Delta t^2). \tag{3.22}$$

From the known or estimated value of $\mathbf{r}(t)$, the method estimates $\mathbf{r}(t+\Delta t)$ by extrapolating from $x(t)$ the straight line that has slope $d\mathbf{r}/dt$, evaluated at t. The velocity can be obtained via

$$\dot{\mathbf{r}}(t+\Delta t) = \dot{\mathbf{r}}(t) + \Delta t\ddot{\mathbf{r}}(t) + \mathcal{O}(\Delta t^2). \tag{3.23}$$

The Verlet Algorithm The Verlet algorithm [43, 17] is a third order integration scheme, combines two Taylor expansion of the coordinates $\mathbf{r}(t)$,

$$\mathbf{r}(t+\Delta t) = \mathbf{r}(t) + \Delta t\dot{\mathbf{r}}(t) + 0.5\Delta t^2\ddot{\mathbf{r}}(t) + \mathcal{O}(\Delta t^3) \tag{3.24}$$
$$\mathbf{r}(t-\Delta t) = \mathbf{r}(t) - \Delta t\dot{\mathbf{r}}(t) + 0.5\Delta t^2\ddot{\mathbf{r}}(t) - \mathcal{O}(\Delta t^3) \tag{3.25}$$

Adding these two equations and rearranging them results in

$$\mathbf{r}(t+\Delta t) = 2\mathbf{r}(t) - \mathbf{r}(t-\Delta t) + \ddot{\mathbf{r}}(t)\Delta t^2 + \mathcal{O}(\Delta t^4), \tag{3.26}$$

To estimate the velocities a central difference estimator is used,

$$\dot{\mathbf{r}}(t+\Delta t) = \frac{\mathbf{r}(t+\Delta t) - \mathbf{r}(t-\Delta t)}{2\Delta t} + \Delta t\ddot{\mathbf{r}}(t), \tag{3.27}$$

where $\ddot{\mathbf{r}}$ is the acceleration resulting from the forces acting upon the particle.
As this method requires information from two timesteps, it is not self starting. It has to be initialised for the first timestep, which is done via a backward Euler step

$$\mathbf{r}(t-\Delta t) = \mathbf{r}(t) - \Delta t(\mathbf{v} - \Delta t\ddot{\mathbf{r}}).$$

Simulation timestep

In section 3.2.5 the contact time of the particle-particle collisions is calculated. To properly resolve the collision while still maintaining low computational costs, the timestep is chosen to be 1/20 - 1/15 of the collision time.

Optimisation

The basic algorithm considers each pair of particles for the force calculation, meaning the complexity is of $\mathcal{O}(N^2)$. Since the forces between granular particles used in this simulation are contact based, only the closest neighbours of the particles need to be considered for interaction. This can be used to considerably increase the efficiency of computation.

Link-Cell-Algorithm The simulation area of size $lx \times ly \times lz$ is divided into $nx \times ny \times nz$ identical rectangular boxes of size $(lx/nx) \times (ly/ny) \times (lz/nz)$. The length of the boxes must be at least the diameter of the largest particles.
In the beginning of each timestep, all particles are assigned to a box with index (x, y, z). All particles in that box are counted. Particles in this box then only collide with particles in the same box, or with particles in neighbouring boxes. To avoid accounting the forces between particles in two different boxes twice only boxes logically after the current box are considered during the determination of the forces.

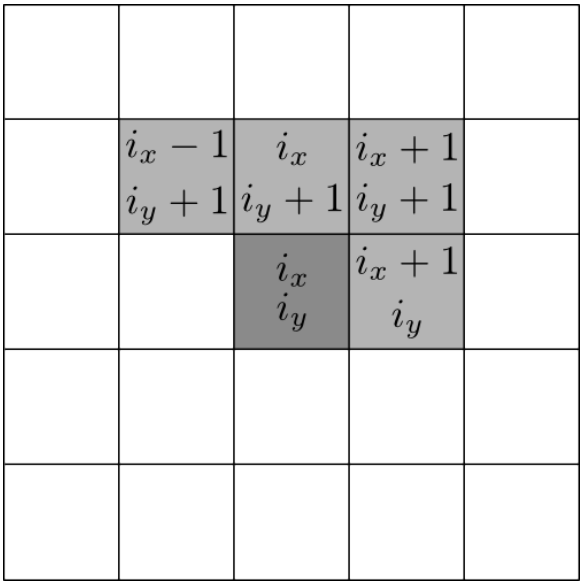

Figure 3.15.: 2D-example of the linkcell algorithm.

In this example, the current box is (i_x, i_y) and the neighbouring boxes for the force calculations are $(i_x + 1, i_y)$,$(i_x - 1, i_y + 1)$,$(i_x, i_y + 1)$ and $(i_x + 1, i_y + 1)$.

3.5.2. Verification

To verify the simulation, it is checked for consistency with conservation laws. One particle is shot in an head-on collision on an identical copy resting in a distance.

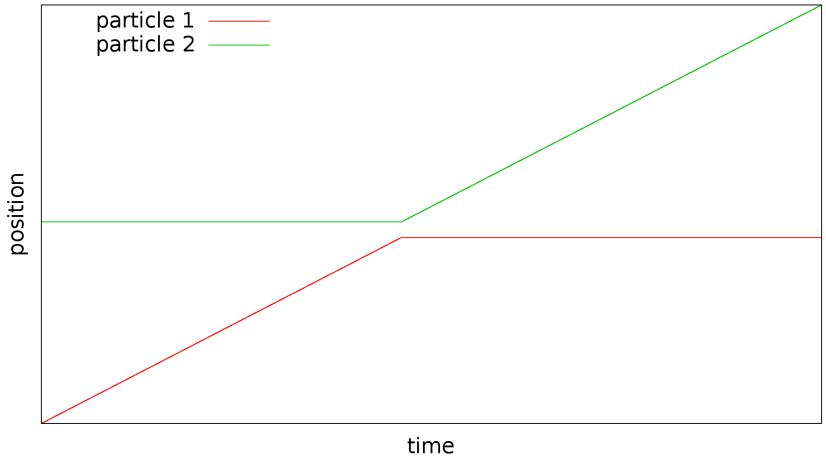

Figure 3.16.: Trajectories for two identical particles in a head on collision.

The collision occurs at about 3.8 seconds, the projectile comes to rest and the target starts to continue on the projectiles path, as required for conservation of momentum (fig 3.17).

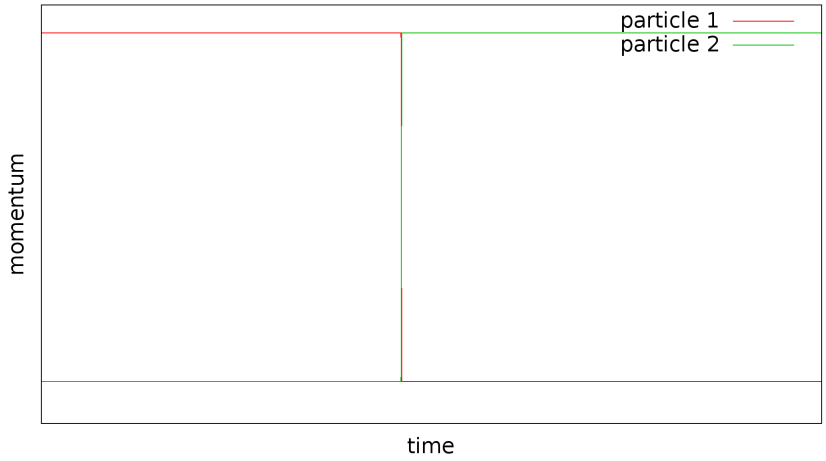

Figure 3.17.: Momenta transfer for projectile particle and target particle.

Using spheres without normal dissipation shows that energy in the system is conserved (fig 3.18).
If one particle leaves the designated simulation area, the program returns an area. This is done to conserve the particle number in the simulation.

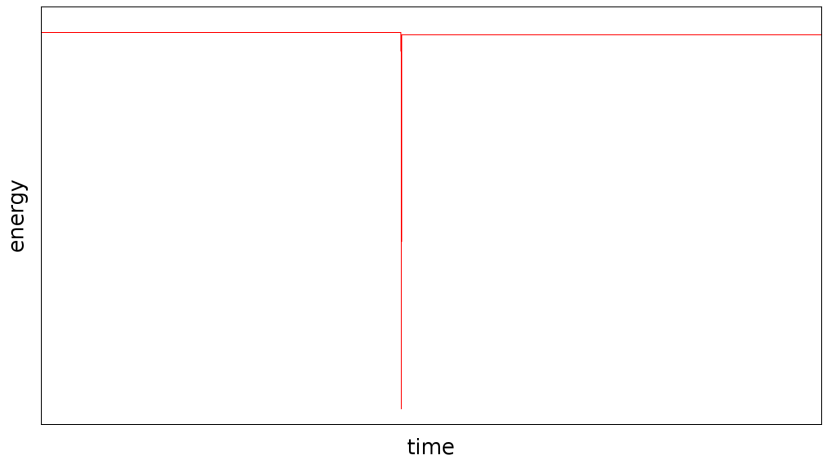

Figure 3.18.: Evolution of the total amount of kinetic energy in the two particle system.

A sphere rolling on a horizontal plate with an initial translational velocity will gradually lose its kinetic energy and eventually stop travelling due to friction from interaction with the plate. This is used as a simple test for the implementation of rolling friction. Initially the sphere is resting on the plate, and at time $t = 0$ starts to move with a translational velocity of $v_x = 0.05\frac{\mathrm{m}}{\mathrm{s}}$ but no angular velocity. The physical properties used for this test are the same as in Table 3.1, with the exception of μ_r, and the radius of the sphere is $r = 0.0005\,\mathrm{m}$. Figure 3.19 shows the distance covered by the sphere versus time.

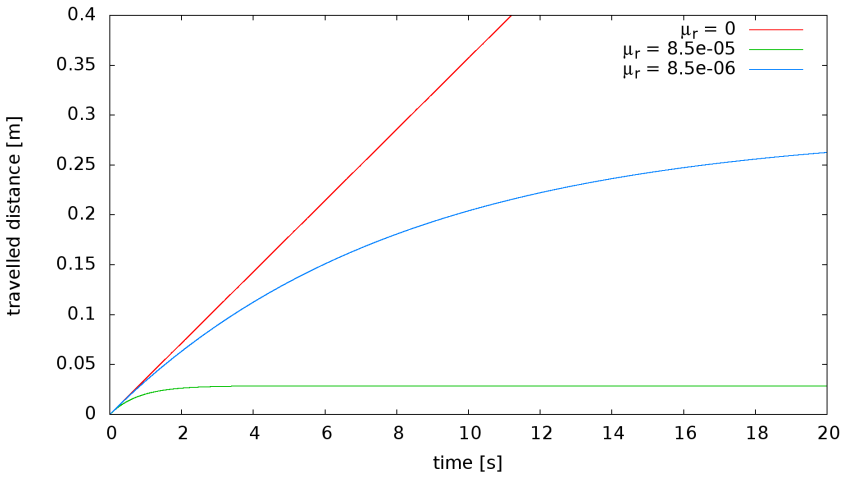

Figure 3.19.: Travelled distance of a 0.5 mm sphere moving on a horizontal plane with different rolling friction coefficients μ_r.

If no rolling friction is applied, no resistance is available to stop the rolling of the sphere, allowing it to move indefinitely, which is shown by the linear increase of the

travelled distance with time. Once rolling friction is introduced into the system, a friction torque arises, counteracting the rotational motion of the particle, thus stopping its motion after a finite time. As expected, the distance varies with μ_r, with higher coefficients halting the particle earlier.

3.5.3. Preparation of the samples

For the simulations, nine different samples are created and used in all configurations of the simulation. To create these samples, n particles with a random radius from an equal distribution between $r_{\min}$ and $r_{\max}$ (fig 3.20) according to table 3.2 are distributed on an (lx,ly)-lattice in one or more layers.

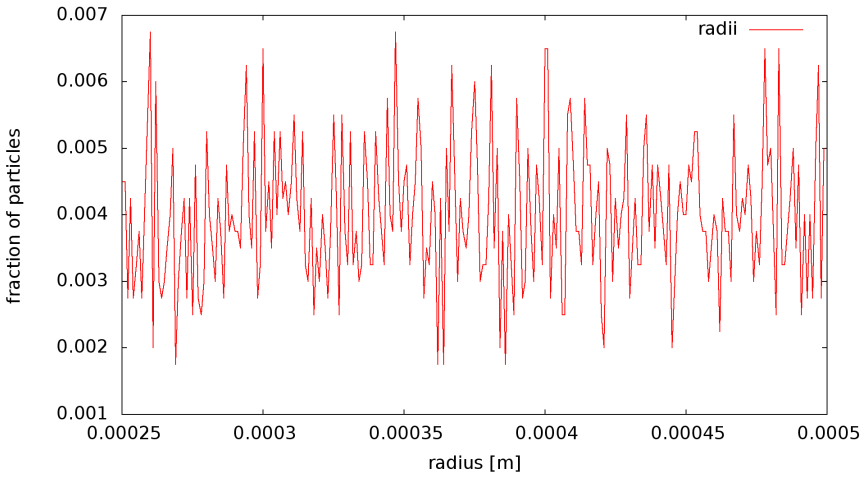

Figure 3.20.: Distribution of radii in one of the samples. The radius range is divided in 250 bins of length $1e^{-6}$ m.

These particles are attributed a random velocity in x- and y- direction from an equal distribution between $v_{\min}$ and $v_{\max}$. The particles then are placed inside the simulation box and move according to their velocities for 10 seconds. After that all linear and rotational velocities and accelerations are set to zero. The resulting positions are used as initial values for the actual simulation runs. Figure 3.21 shows an example of a system before the particle positions are distributed according to their velocities (fig 3.21a), and after (fig 3.21b).

Table 3.2.: ranges of particle radii and velocities

	minimum	maximum
radius [m]	0.00025	0.0005
velocity v_x, v_y[m/s]	-0.005	0.005

The box used in the simulations has a length of 0.4 m, a width of 0.02 m, and its height is limited to 0.1 m. In the y-direction, the box is limited by walls on both sides, in the x-direction periodic boundaries connect both sides of the box. The z-direction is limited by a wall on the ground, but open in positive direction.
The following simulations consist of $n = 4000$ particles. The different configurations are generated with the same limits, but different seeds for the randomisation. In each simulation the same initial configuration is used, i.e. figure 3.27a uses the same initial

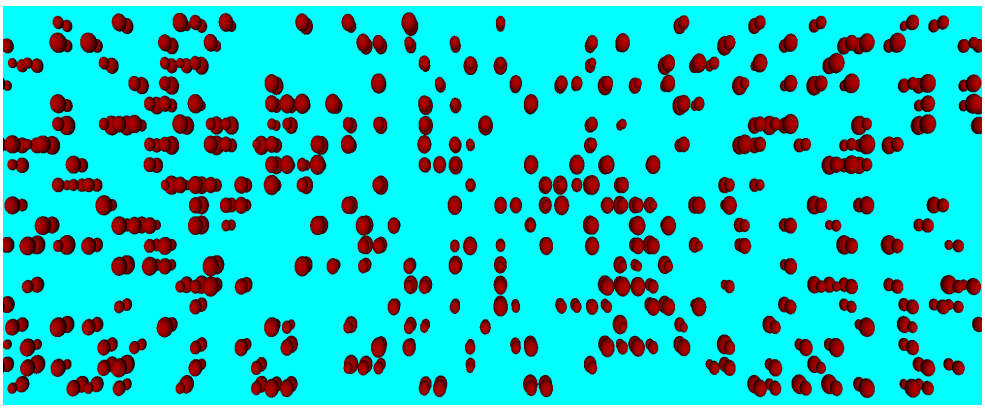

(a) Close-up of the particle positions before distributing, showing two layers in a grid structure.

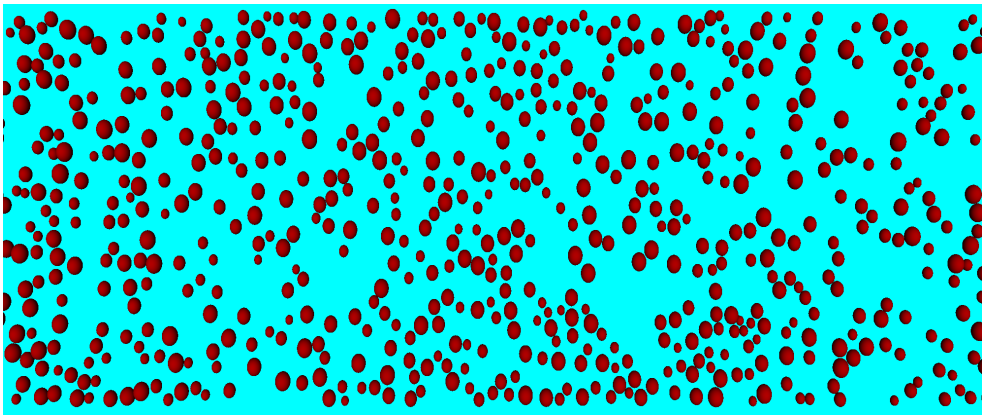

(b) Close-up of the particle positions after distributing, showing an isotropic arrangement.

Figure 3.21.: Comparison of samples before and after distributing the particle positions.

configuration as figure 3.29a. The particle properties given in table 3.3 are constant for all simulations, except for the one specified parameter that is deactivated in the respective simulation. The properties are chosen to approximate glass beads [69, 2]. To allow faster computation the Youngs modulus is reduced. Compared with the experiment, the biggest discrepancy is the form of the particles. In the experiment, the grains are of irregular form, in the simulation the particles are perfect spheres. Global values are given in table 3.4. They are kept constant through all simulations unless stated otherwise.

All map-plots in the following part show the evolution of the one-dimensional density profile over the length of the box, calculated according to the method described in appendix A. The colour of the figures displays the density fraction, the horizontal axis the length of the box, and the vertical axis the simulation time. Snapshots of the systems are taken every full period of the shaking motion at every second turning point.

Table 3.3.: physical properties of particles and walls

	mean radius	density	Youngs' modulus	dissipation
symbol [unit]	$\overline{R}$ [m]	ρ [kg/m^3]	Y [kg/ms^2]	A [s]
value	0.000375	2500	10^6	$8.5 \cdot 10^{-6}$
	friction	rolling friction	tangential damping	-
symbol [unit]	$\mu_{\text{pp/pw}}$ [1]	μ_r [s]	γ_t [Nsec/m]	-
value	0.7	$8.5 \cdot 10^{-6}$	0.007	-

Table 3.4.: global simulation parameters

	shaking frequency	shaking Amplitude	-
symbol [unit]	ν [1/s]	$\mathcal{A}$ [m]	-
value	20	0.025	-
	gravity	timestep	print step
symbol [unit]	g [m/s^2]	Δt [s]	n_{print} [1]
value	$-10 \parallel \mathbf{e}_z$	$8 \cdot 10^{-6}$	39270

3.5.4. Results

After the initialisation described in section 3.5.3, all particles are placed in one layer inside the simulation box, which is then shaken with an amplitude of 2.5 cm and a frequency of 20 Hz for 20 seconds. The samples end in state (fig 3.22), similar to the state observed in the experiment (fig 2.11).

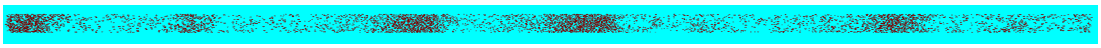

Figure 3.22.: Top-down view of the whole system of sample 1 after 20 seconds.

Figure 3.22 clearly shows the separation of the initial isotropic distribution into distinct bands of particles. The stripes show a dense front in direction of the current thrust from the system, and a gas-like tail following them. Within one stripe, particles are observed to jump and to roll upon each other (fig 3.23b).
Analysing the density profiles of the samples (fig 3.27) shows that stripe formation occurs spontaneously after 3-5 seconds, depending on the initial distribution of particles in the sample. As the different realisations show, the initial distribution has huge influence on number, position, size and orientation of the stripes, as well as their stability. Furthermore it can be seen, that even after the formation of the stripes, minor, short-lived stripes can arise from the gas-like medium between the stripes and either dissolve again into the medium or merge with the major stripes (e.g. 3.27c), possibly influenced by particle size. The number of stripes in all configurations in the last phase of the simulation is manually counted, based on a density threshold of 0.03/m. The average number of stripes after 20 seconds in a 0.4 m long system is found to be 4 ± 0.875.

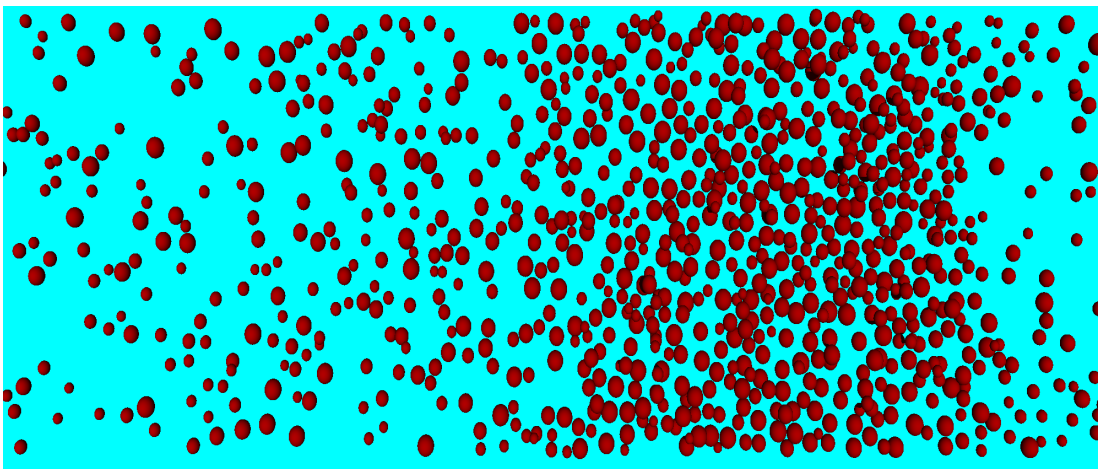

(a) Close-up view of one stripe of 3.22, top-down, focused on $x = 0.185\,\mathrm{m}$, showing the increased packing fraction within the stripe and the gas-like tail with decreasing packing fraction.

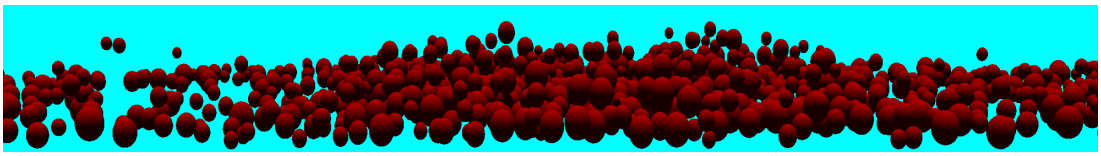

(b) Close-up view of 3.23a, from the side.

Figure 3.23.: Close-up view of sample 1, focused on the stripe at $x = 0.2\,\mathrm{m}$, after 20 seconds.

The trajectory of a single particle (particle 0 in system 3.27a) in the x-y-plane shows a irregular motion (3.24a). The particle starts its way at the blue cross mark. and in the beginning follows a regular oscillating path, with some light motion perpendicular to the shaking direction resulting from an early collision. The particle then deviates from this path, and, with higher velocity starts to move through the system. At some time its trajectory appears to be confined in the range of $x = [0.19 : 0.23]\,\mathrm{m}$ and $y = [0.011 : 0.02]\,\mathrm{m}$ and shows signs of confinement in $x = [0.24 : 0.28]\,\mathrm{m}$ in the same range of y. Both confinement areas correspond to stripes in the density profile.During the course of the simulation the particle explores the whole width of the box, though mainly stays in the upper half (fig 3.24a). The irregularity of motion shows itself in the particles phase space trajectory as well (fig 3.24b).
Larger particles colliding with smaller ones may be thrown into the air and follow a ballistic trajectory until they touch ground again. This happens at higher frequency in stripes, as the particle density is much higher there (fig 3.25).
The distribution of particle radii in the stripes during the last phase of the simulation shows an uniform distribution (fig 3.26) akin to the initial distribution of particles. The average radius in the stripes is $R_{\mathrm{avg}} \approx 0.0003760\,\mathrm{m}$. Compared to the whole system, this is a change of about 2.532 per cent, suggesting that size segregation plays no role in stripe formation.

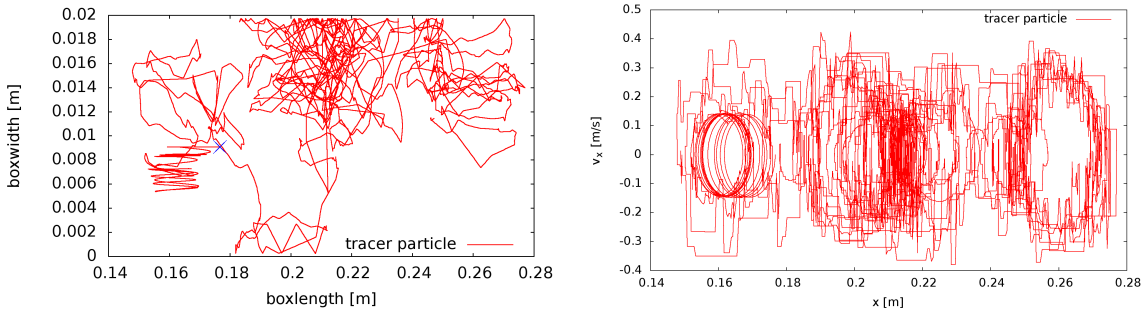

(a) Trajectory (b) Phase space

Figure 3.24.: Motion of a tracer particle within the system and the phase space trajectory of said tracer particle, limited to the x-coordinate of the system.

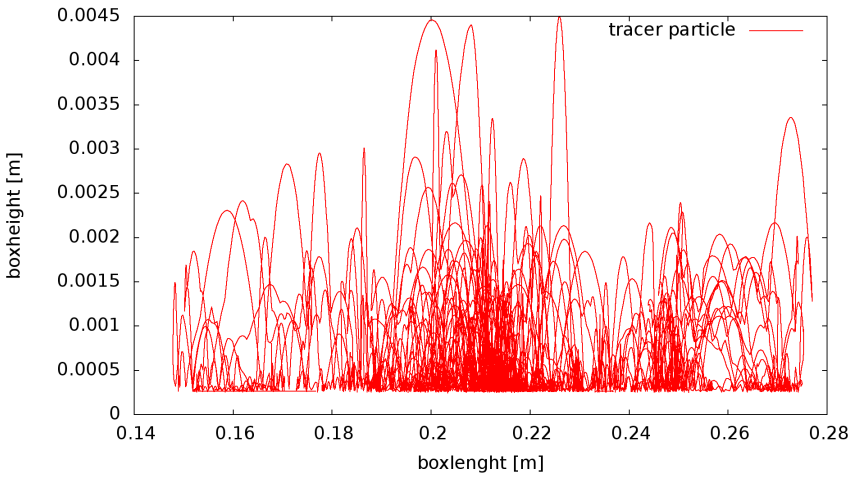

Figure 3.25.: Off-plane motion of the tracer particle. The radius of the particle is about 0.00026 m.

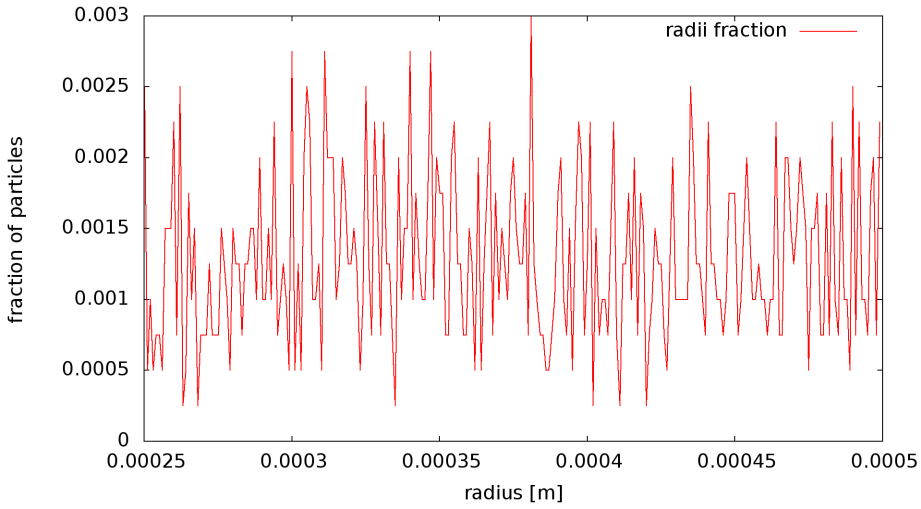

Figure 3.26.: Distribution of particle radii in the stripes at the end of the simulation in sample one. The other samples look identical, except for fluctuations and have been omitted for clarity.

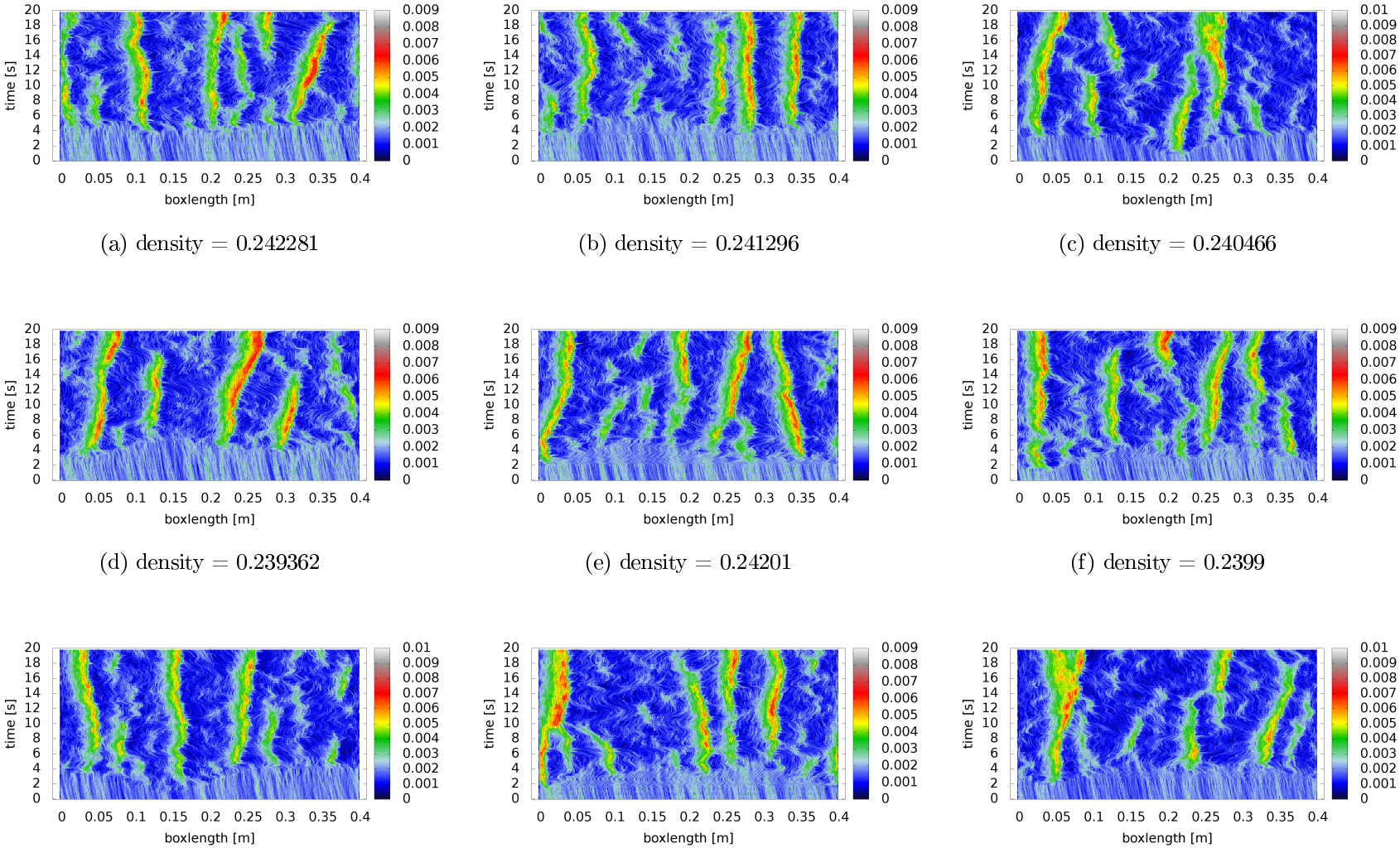

(a) density = 0.242281 (b) density = 0.241296 (c) density = 0.240466

(d) density = 0.239362 (e) density = 0.24201 (f) density = 0.2399

(g) density = 0.241577 (h) density = 0.240481 (i) density = 0.241144

Figure 3.27.: Temporal evolution of the density distribution for different initial configurations.

Influence of the friction

The simulation is repeated with the Coulomb coefficient of friction for particle-particle interaction set to zero, $\mu_{pp} = 0$. This makes particle-particle interaction smooth and prevents jamming of particles. All other parameters kept constant.
The density profile of the system (fig 3.29) immediately shows, that no stripe formation occurs, unlike in the reference case (fig 3.27). Instead the initial distribution remains for the most part, shifted slightly into the direction of the initial thrust of shaking, and then remaining stationary. The x-y-trajectory of the tracer particle (fig 3.28a) confirms, that with some weak interactions in ±y-direction, the particle essentially follows a periodic trajectory. The phase space trajectory of the tracer particle (fig: 3.28b) shows high similarity to the phase space motion of the single particle in 3.10a, suggesting the systems behaves largely like a collection of independent spheres.

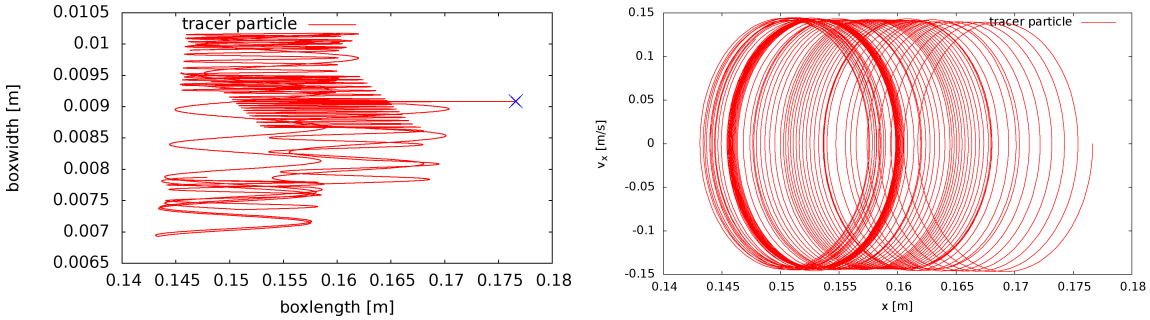

(a) Trajectory

(b) Phase space

Figure 3.28.: Trajectory and phase space motion of the tracer particle. The Phase space is limited to the x-coordinate of the system.

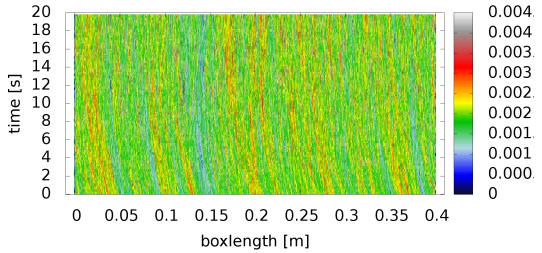

(a) density = 0.242281

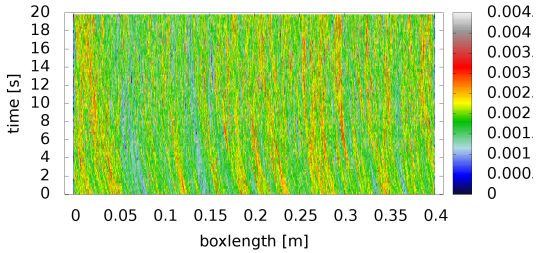

(b) density = 0.241296

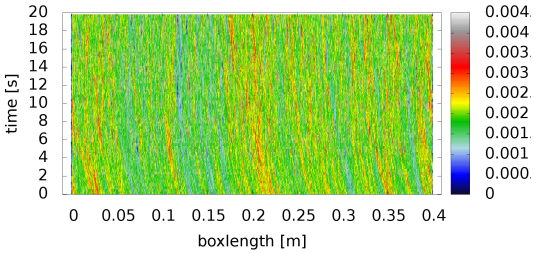

(c) density = 0.240466

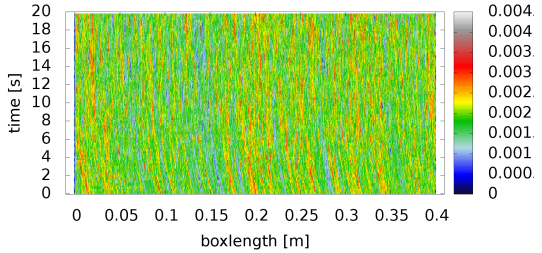

(d) density = 0.239362

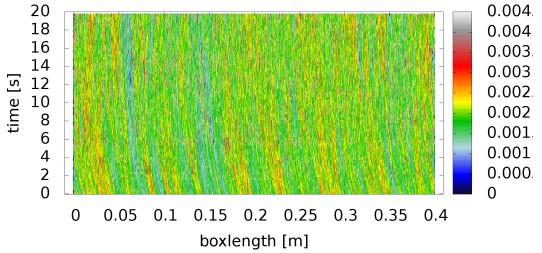

(e) density = 0.24201

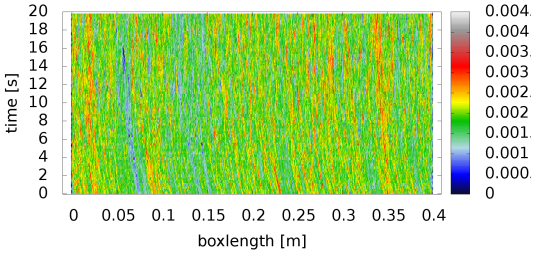

(f) density = 0.2399

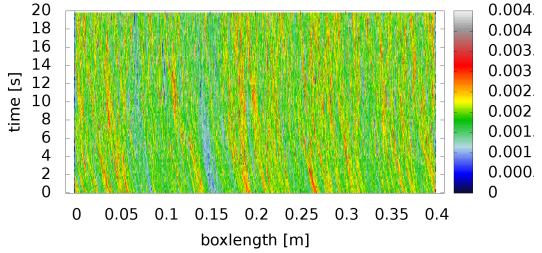

(g) density = 0.241577

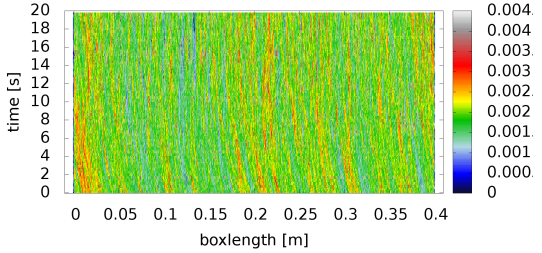

(h) density = 0.240481

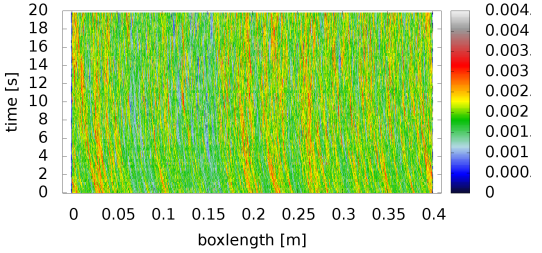

(i) density = 0.241144

Figure 3.29.: Evolution of the density distribution for different initial configurations.

Influence of shaking amplitude and frequency

The initial simulation is repeated for a larger range of forcing parameters ν and $\mathcal{A}$. Each combination of $(\nu, \mathcal{A})$ in figure 3.30 represents the evolution of the density during the first 15 seconds of the simulation. This duration is chosen, to allow evolution for the majority of the systems, and to be fast enough to process a multitude of configurations. Three major distinct regions can be identified (fig 3.31):

(a) Nothing happens in the low frequency - low amplitude corner,

(b) Stripes emerge from the medium frequency - medium amplitude to the upper low frequency - high amplitude corner,

(c) The system becomes gas-like in the high frequency - high amplitude corner corner

Clear stripe formation can be seen at intermediate driving frequencies and high driving amplitudes, where stripes are stable during the entire simulation and no fluctuations appear[3].
Between these three dominant regions, minor regions appear, that can not be clearly attributed to one of the big regions. These are

(1) A region with proto stripes between (a) and (b), likely to form clear stripes at a later point in time,

(2) Very weak and dilute stripes between (b) and (c) (top), being subject to too much agitation,

(3) Some sort of pseudo structures between (b) and (c) (bottom)

Figure 3.31 gives an abstract overview over the regions and their position in phase space. Regions (1)-(3) might be phase transitions between (a),(b), and (c), instead of being actual regions themselves. Especially the clear transition between $(17, 0.035)$ and $(20, 0.035)$.

[3] A good example of this is the configuration $(14, 0.035)$

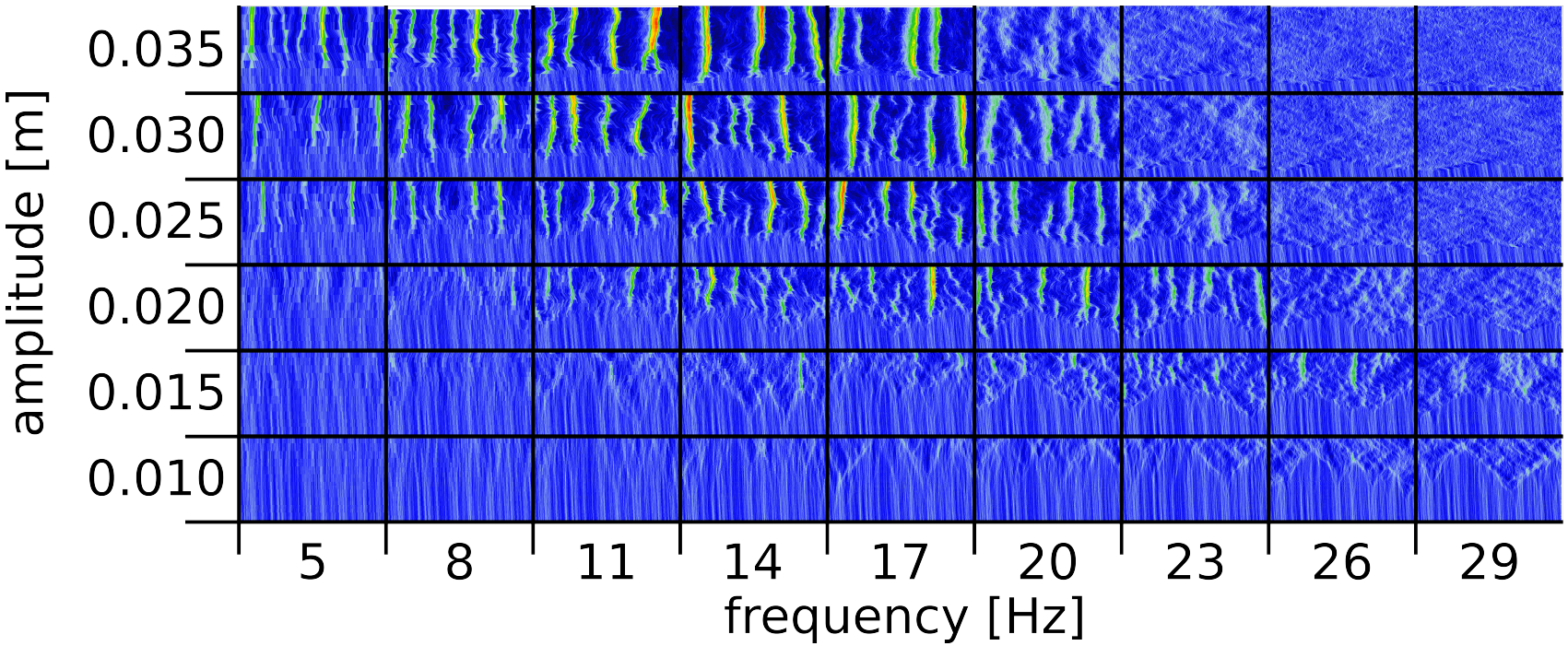

Figure 3.30.: Influence of amplitude and friction.

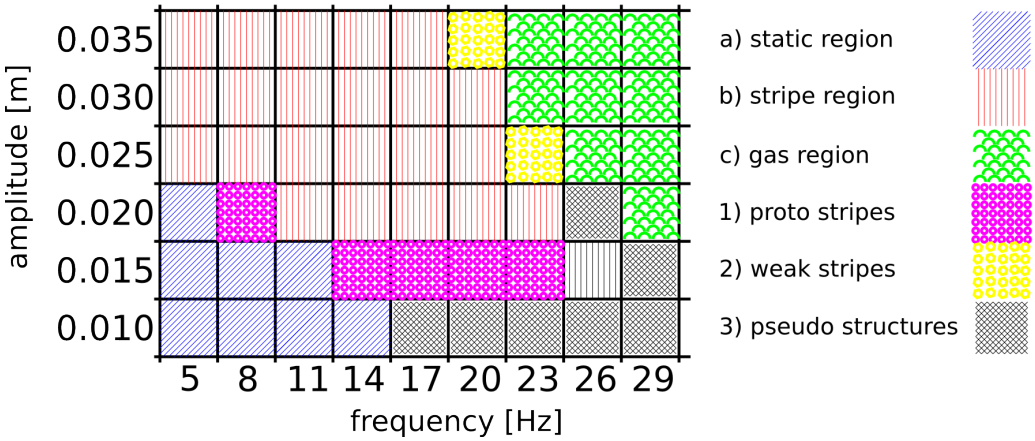

Figure 3.31.: Abstract representation of figure 3.30 to emphasise the different regions in phase space.

Influence of particle jumping

In these simulations the particles are confined to the ground. This is done by testing each particle i if it suffices the condition

$$z = \min(R_i, z). \tag{3.28}$$

While this violates Newtonian physics, it only serves as a test on jumping. The other parameters are kept the same as in the reference simulations.
As seen in the density profiles (fig 3.32), the system still forms stripes. Indeed, the mechanism of ballistic flight, that Strassburger et al. used in their cellular automaton 3.1 is not required for stripe formation. Opposed to the full model with particle jumping, this system takes longer to cluster, stripes occur after about 6-9 seconds. The stripes are generally smaller, but of higher density and show more short lived stripes appearing and disappearing during the simulation. The average number of stripes at the end of the simulation is 4 ± 1, based on a density threshold of 0.004/m. In the beginning, until about 5 seconds, the tracer particle moves with weak interaction in tangential direction, similar to the case of the frictionless particles (fig 3.33). The next seconds are spent in-between the stripes After about 16 seconds, the particle joins the newly emerging stripe at $x \approx 0.16\,\mathrm{m}$ and stays with it until the end of the simulation.

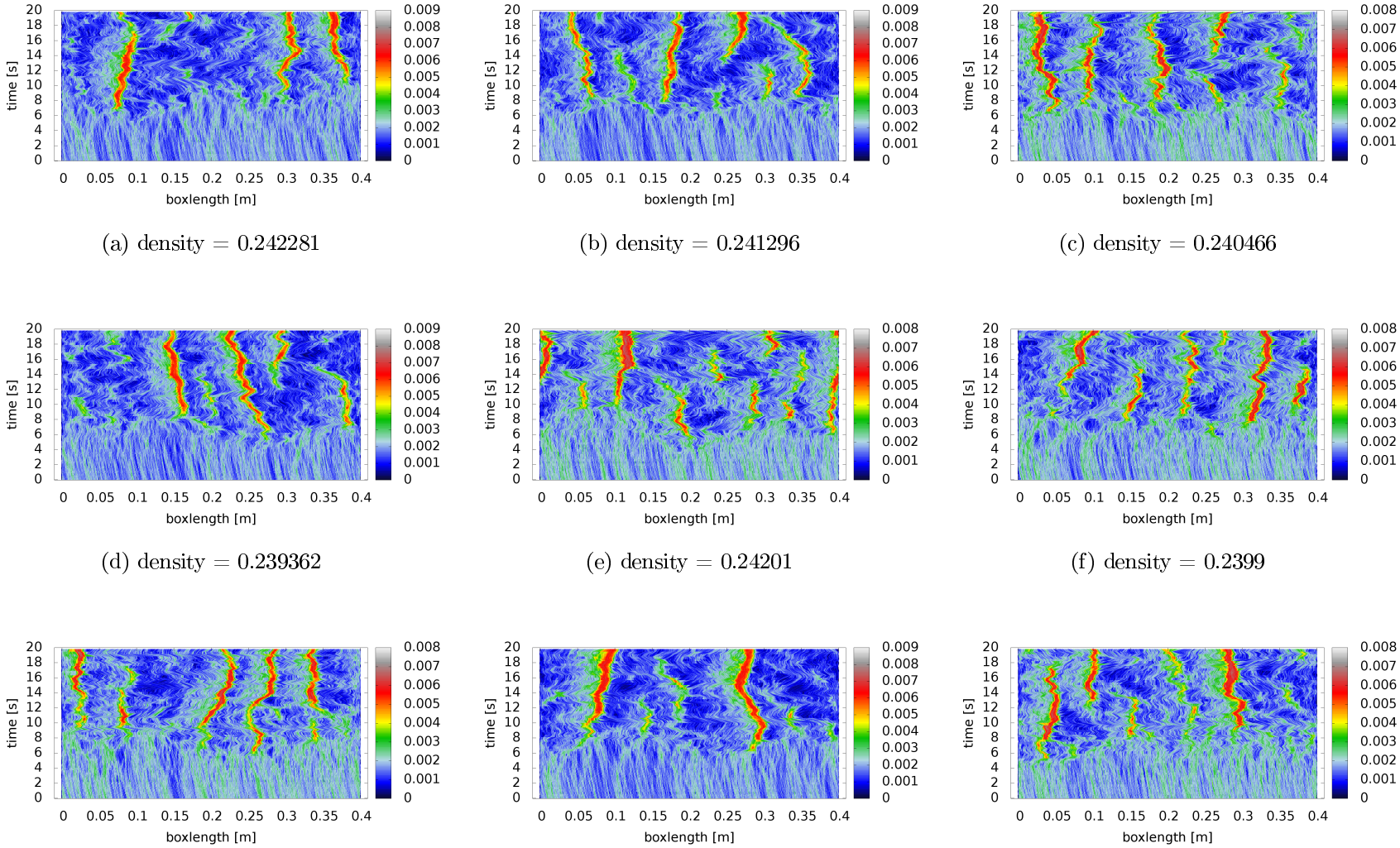

(a) density = 0.242281 (b) density = 0.241296 (c) density = 0.240466

(d) density = 0.239362 (e) density = 0.24201 (f) density = 0.2399

(g) density = 0.241577 (h) density = 0.240481 (i) density = 0.241144

Figure 3.32.: Temporal evolution of the density distribution for different initial configurations.

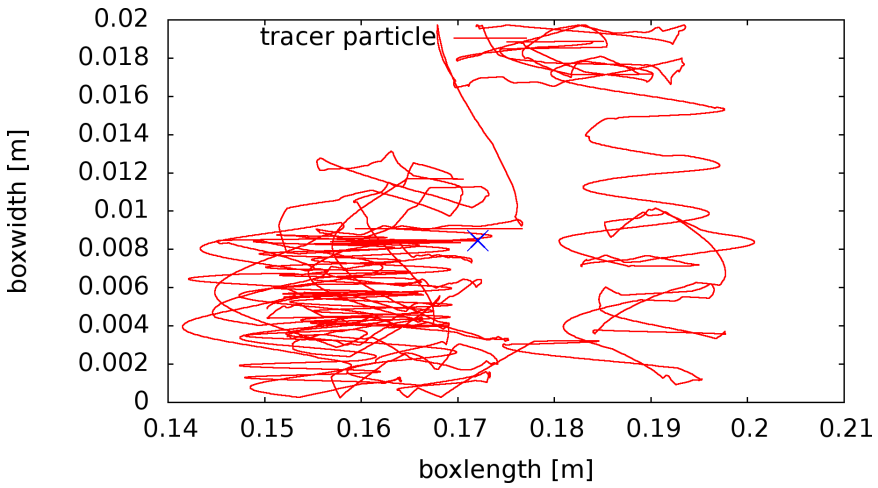

Figure 3.33.: Motion of a tracer particle in a two dimensional system.

Influence of the dissipation

In these simulations, the normal dissipation between particles is set to zero, $A_{pp} = 0$, i.e. the particle collisions now follow the classical Hertz law

$$F_{\mathrm{el}}^{n} = \frac{2Y\sqrt{R_{\mathrm{eff}}}}{3(1-\nu^2)}\xi^{3/2}. \tag{3.29}$$

The other parameters are kept the same as in the reference simulations.
Stripe formation sets in earlier than with normal dissipation, after about 2-4 seconds (fig 3.34). The stripes are larger, but less dense than in the damped case. The systems show, that the stripes undergo both merging and branching, i.e. one stripe splitting into two, more frequently than before. During a collision particles will not lose energy and thus separate with their initial velocities. However one of the particles always has to move against the shaking motion of the box, and consequently is stopped and turned back, remaining in close proximity to its former collision partner. The distance between the particles after the collision is larger than in the damped reference case. Consequently the stripes are broader and less dense. Over time, particles then accumulate with decreasing distances, until they jam and start sliding on the floor.
The average number of stripes at the end of the simulation is 4 ± 1, based on a density threshold of $0.003/\mathrm{m}$.
The tracer particle (fig 3.35) is absorbed by the stripe at $x \approx 0.1\,\mathrm{m}$ early in the simulation and stays within the stripe for most of the time. After about 12 seconds the particle briefly moves into the emerging stripe on the left side of the stripe before rejoining the original one.

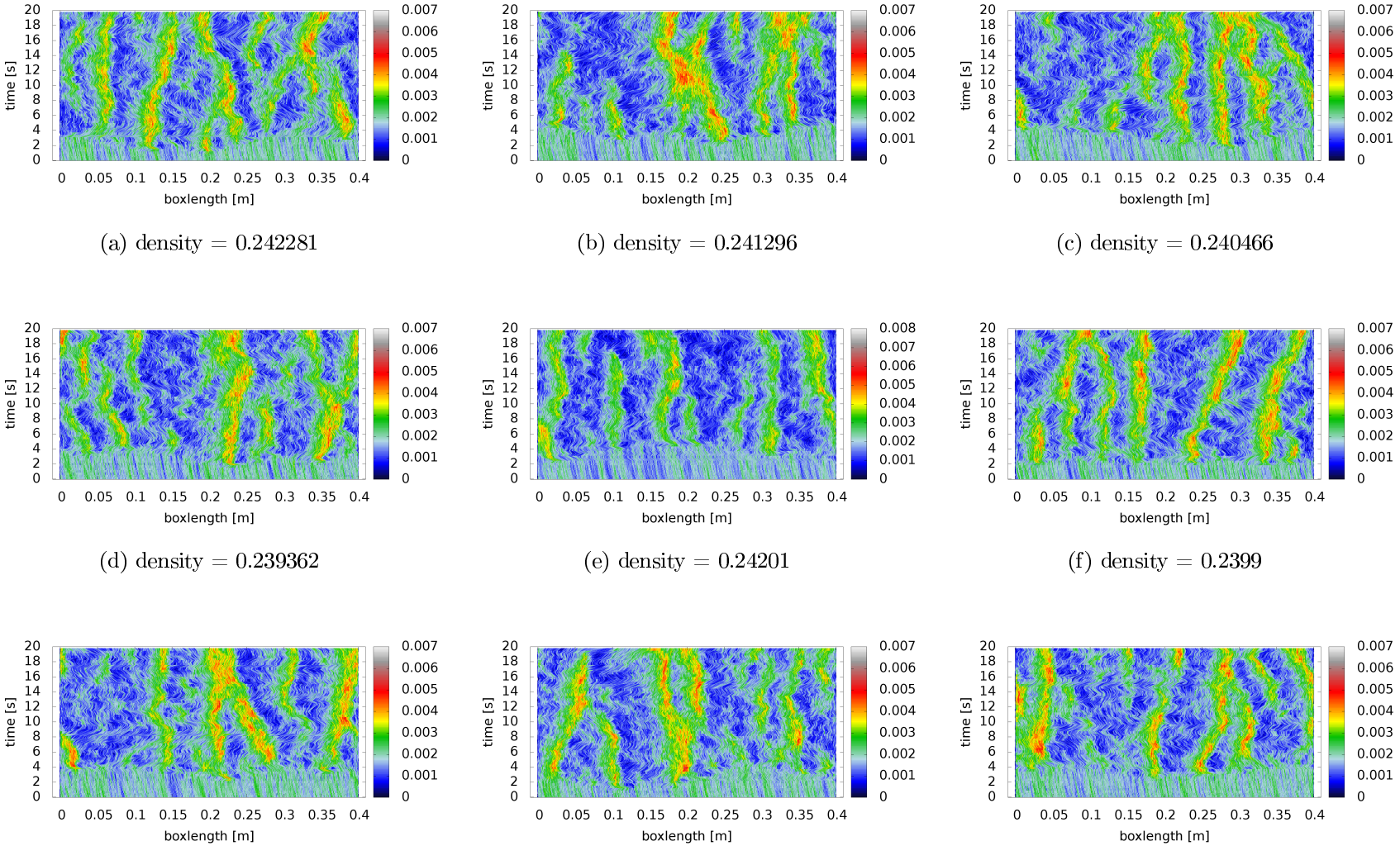

(a) density = 0.242281 (b) density = 0.241296 (c) density = 0.240466

(d) density = 0.239362 (e) density = 0.24201 (f) density = 0.2399

(g) density = 0.241577 (h) density = 0.240481 (i) density = 0.241144

Figure 3.34.: Evolution of the density distribution for different initial configurations in the undamped case.

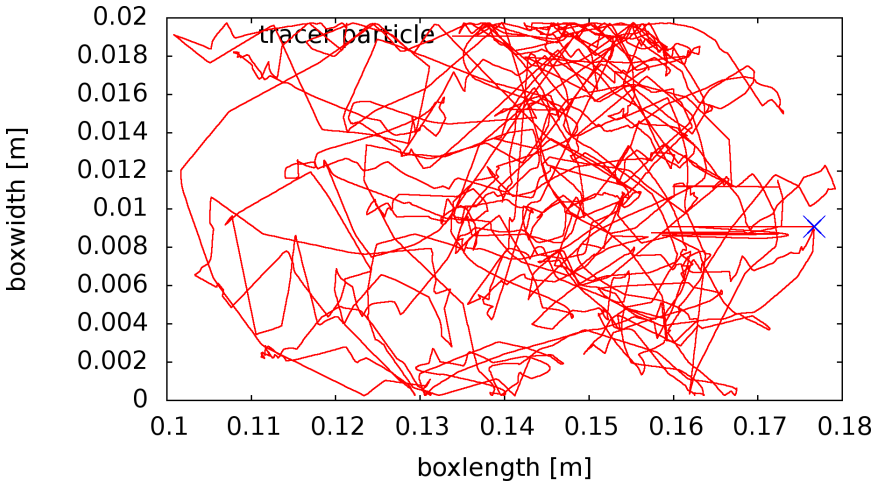

Figure 3.35.: Motion of a tracer particle in a dissipationless system.

Influence of the walls

Additional periodic boundaries in the y-direction are introduced. The simulations are then repeated.
Stripe formation occurs after about 4-6 seconds (fig 3.37), slightly later than in the reference case. More stripes form than in the initial case, but the stripes are smaller. More short lived stripes appear and disappear. It can be concluded, that walls are not critical for stripe formation. The additional damping caused by the particle-wall friction accelerates stripe formation, but it is not necessary for their formation.
The average number of stripes is 5 ± 1, based on a density threshold of 0.003 1/m.

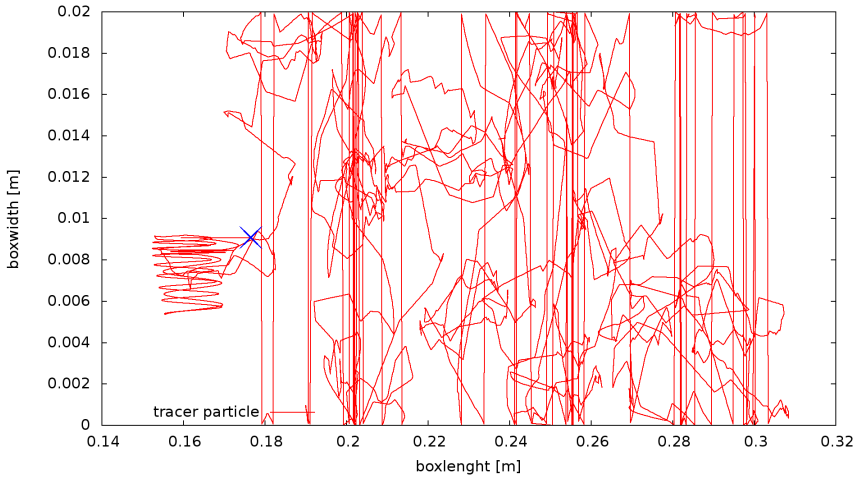

Figure 3.36.: Motion of the tracer particle in a wall-less system.

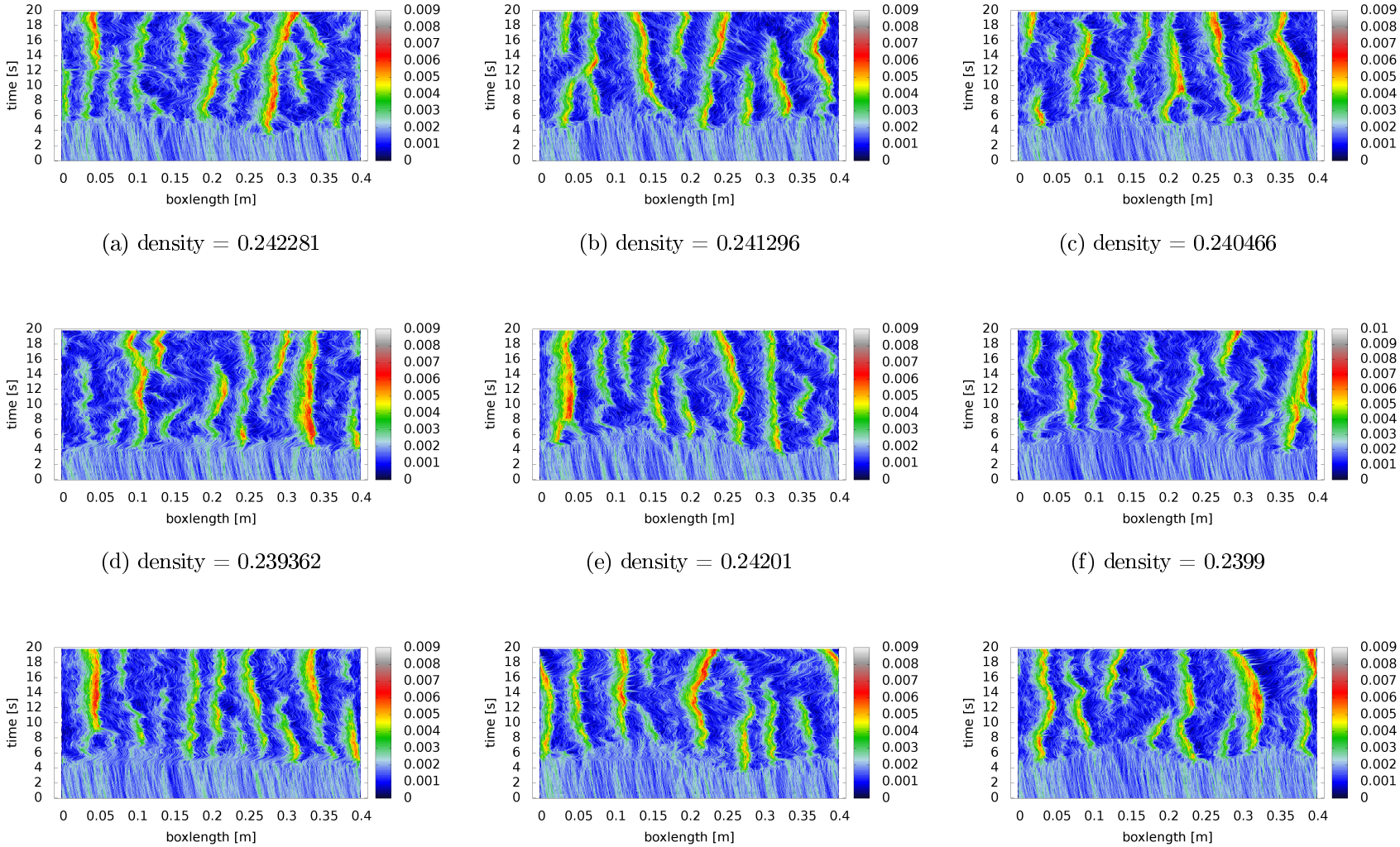

(a) density = 0.242281 (b) density = 0.241296 (c) density = 0.240466

(d) density = 0.239362 (e) density = 0.24201 (f) density = 0.2399

(g) density = 0.241577 (h) density = 0.240481 (i) density = 0.241144

Figure 3.37.: Evolution of the density distribution for different initial configurations in a twofold periodic system.

Comparison of the different systems

The x- and y- components of the position of the tracer particle are shown in figure 3.38a and 3.38b, respectively.

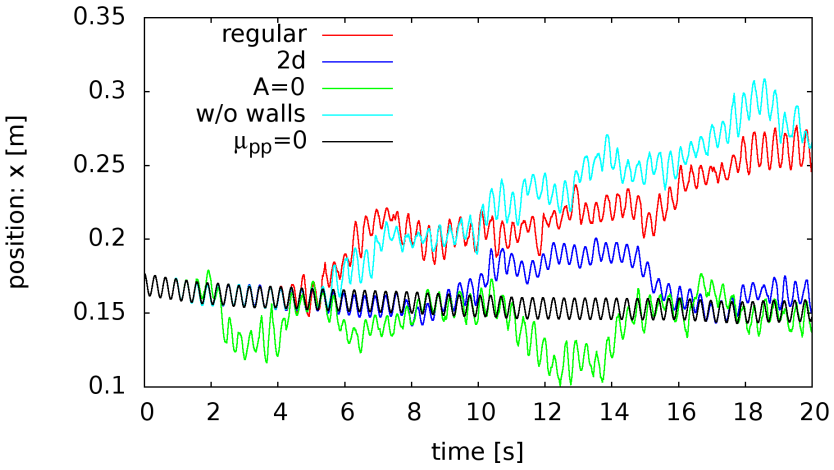

(a) x-trajectory

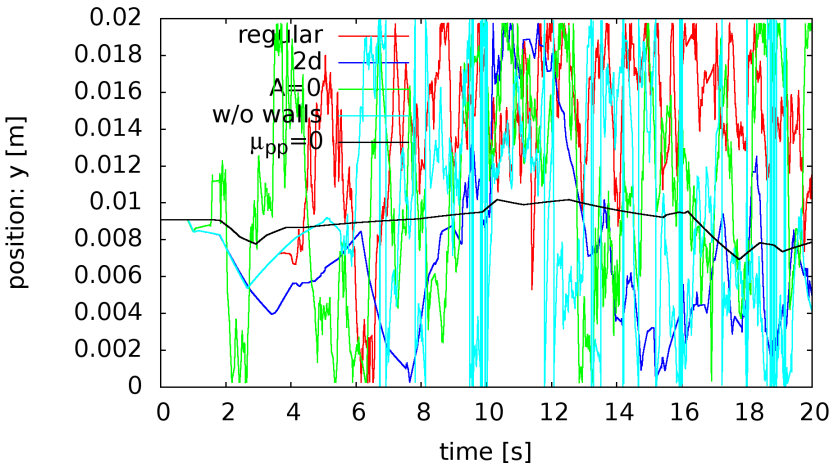

(b) y-trajectory

Figure 3.38.: x- and y-positions of the tracer particles.

In all systems but the frictionless one, the motion of the particle shows similar highly irregular behaviour with especially strong fluctuations in y. The tracer particle in the frictionless system shows the same behaviour as a single particle in the system with respect to its x-coordinate, and weak interaction in its y-coordinate, slowly fluctuation around its starting value.
For all samples of each system the mean square displacement, D, is calculated via the relation [90],

$$D = \frac{1}{2}\overline{r_i^2} \tag{3.30}$$

where r_i is the displacement of particle i between two successive periods,

$$r_i = |\mathbf{r}_j - \mathbf{r}_{j+1}| \tag{3.31}$$

and the average is taken over all particles in the sample. The displacement then is averaged over all samples of one simulation configuration. Figure 3.39 shows the averaged mean square displacement for the different simulations.

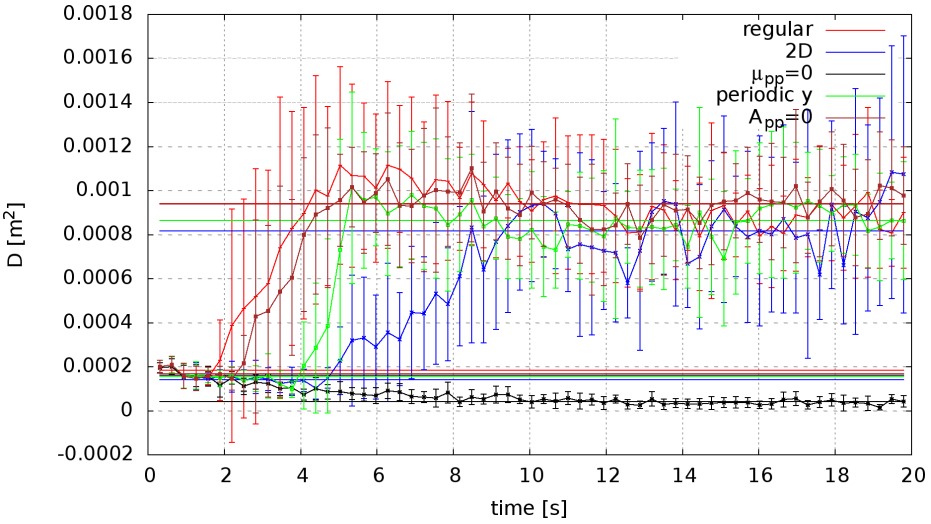

Figure 3.39.: Evolution of the mean square displacement for the different kinds of configurations.

During the first seconds, the value of D remains roughly constant for all systems. For each particular system, the best fit to the curve $D(t)$ is performed using the function $D(t) = a_1$ within the range [0,t]. the first and second column of Table 3.5 show the respective values of a_1 and t corresponding to each system. It can be seen, that a_1 is approximately the same in all cases, and has the average value $a_1 \approx (1.618e^{-4} \pm 1.543e^{-5})\,\mathrm{m}^2$.

Table 3.5.: a_1 (second column) and a_2 (fourth column) are the values of D obtained from the best fit to the simulation data using $D = a_{1,2}$ constant within the corresponding ranges of values of t (displayed in columns 1 and 3, respectively)

system	t-interval [s]	a_1[m^2]	t-interval [s]	a_2[m^2]
regular	[0 : 2]	$1.832e^{-4} \pm 1.369e^{-5}$	[4 : 20]	$9.401e^{-4} \pm 1.236e^{-5}$
2D	[0 : 5]	$1.419e^{-4} \pm 4.385e^{-6}$	[8 : 20]	$8.175e^{-4} \pm 1.982e^{-5}$
frictionless	[0 : 2.5]	$1.612e^{-4} \pm 1.086e^{-5}$	[8 : 20]	$4.248e^{-5} \pm 2.093e^{-6}$
periodic y	[0 : 4]	$1.543e^{-4} \pm 8.655e^{-6}$	[5 : 20]	$8.652e^{-4} \pm 1.056e^{-5}$
dissipation	[0 : 2.5]	$1.685e^{-4} \pm 9.540e^{-6}$	[4 : 20]	$9.387e^{-4} \pm 9.079e^{-6}$

For all systems, but for the one where particle interaction occurs without frictional forces the value of D starts to increase after a certain amount of time, thereafter

approaching a constant value, a_2. By performing the best fit using the ansatz $D(t) = a_2$ within a range of sufficiently large values of time, it is found that $a_2 \approx (8.904e^{-4} \pm 5.987e^{-5})\,\mathrm{m}^2$ (column three and four of Table 3.5). Indeed, the time at which the value $D \approx a_2$ is reached essentially equals the instant where stripes in the system begin to form. The fluctuations in the value of D around the constant value a_2 are associated with particle displacement between two stripes. These fluctuations suggest a correspondence with a gas-like state associated with particle motion in-between the stripes, where particles enter (leave) this state upon leaving (being incorporated to) a stripe.
Figure 3.40 shows, that the value of a_2 depends on the particle's radius; the smaller the particle, the larger the value of a_2.

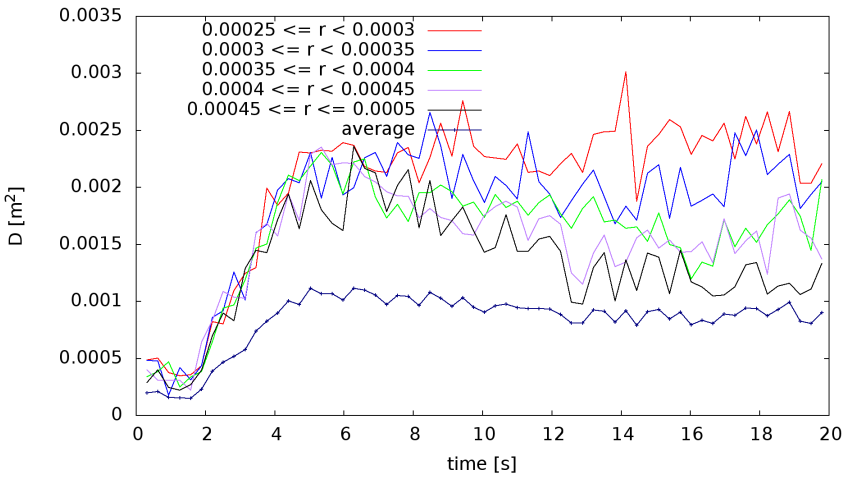

Figure 3.40.: Mean square displacement D as a function of time, for different values of particle radius, R. The evaluation is done exemplarily for the reference simulation, the other simulations follow the same pattern.

Influence of the packing fraction

To observe the influence of the packing fraction, the system is filled with different numbers of particles, while the size of the box remains constant. This leads to two-dimensional packing fractions of about 0.06, 0.12, 0.24, and 0.48, which again was determined as a two-dimensional packing fraction $\rho = \frac{Nr^2\pi}{lx \cdot ly}$. For each packing fraction one sample was created.

Table 3.6.: Number of particles per packing fraction

no. of particles	1000	2000	4000	8000
$\rho\,[1/\mathrm{m}^2]$	0.05807	0.1144	0.2297	0.4583

Packing fraction shows to hold a strong influence in stripe formation (fig 3.41), if the fraction is too low, particles have little chance to come into contact within reasonable time and thus can not form stripes. The system at low fractions, figure 3.41a, shows the behaviour of an ensemble of independent particles as shown in figure 3.10a. With increasing packing fraction particles become correlated and start deviating from the single particle trajectories, see figure 3.41b, and show traces of clustering towards the end of the observation window. Further increasing the fraction creates distinct stripes in the system, figure 3.41c, with traces of merging and branching[4] and then formation of massive structures with increased branching and merging of smaller stripes in the system 3.41d. The onset of structure formation happens much earlier, after a few oscillations cycles.

[4]also compare 3.27

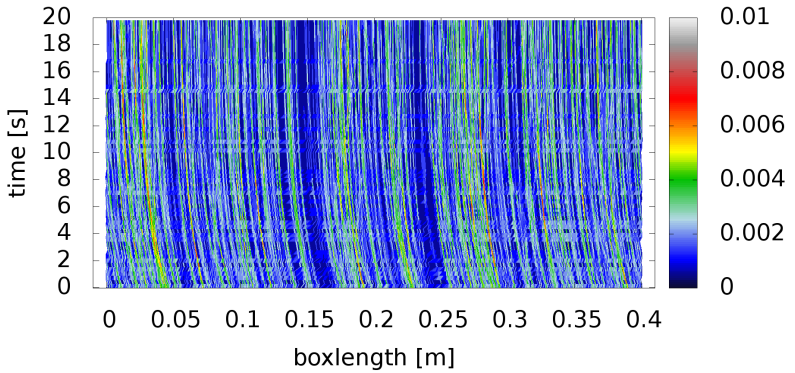

(a) packing fraction = 0.05807

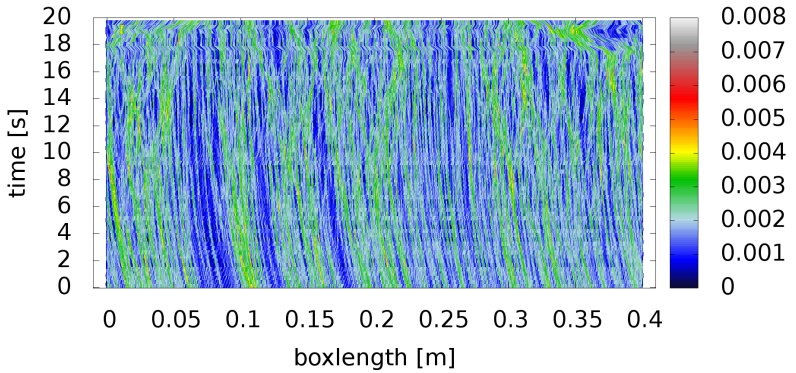

(b) packing fraction = 0.1144

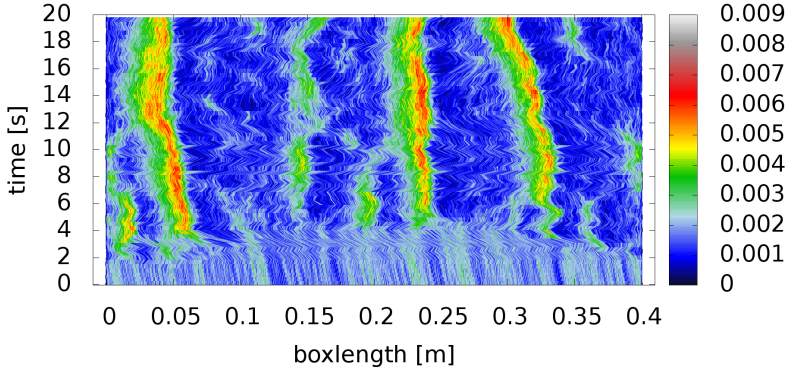

(c) packing fraction = 0.2297

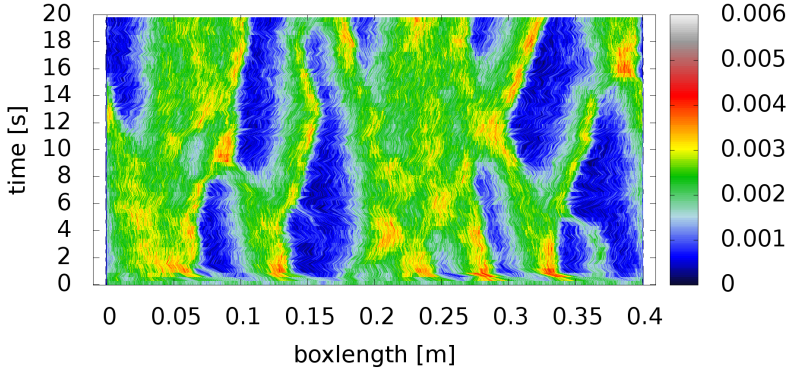

(d) packing fraction = 0.4583

Figure 3.41.: Evolution for systems with different packing fraction.

For each packing fraction, the mean square displacement is calculated.

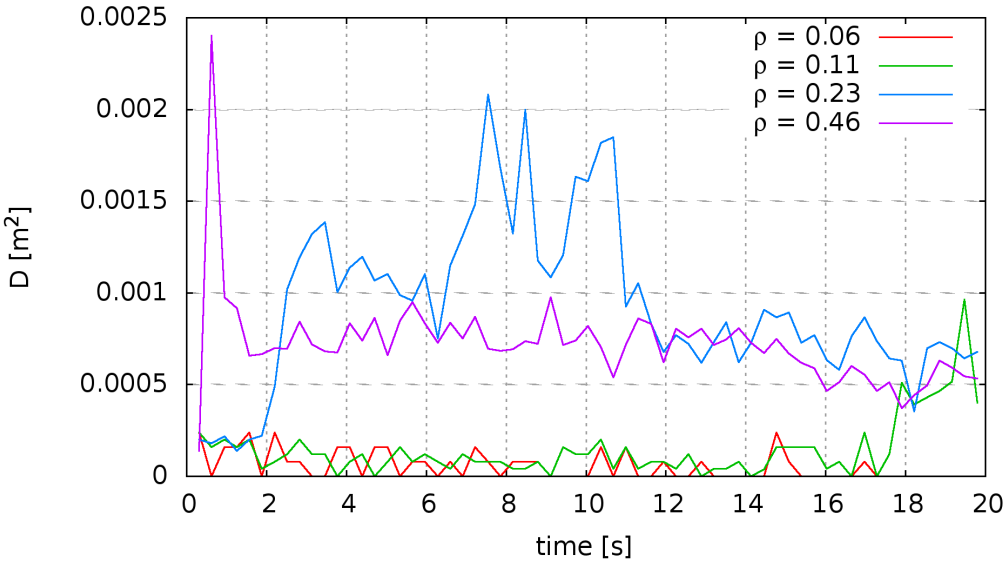

Figure 3.42.: Evolution of the mean square displacement for different packing fractions.

The huge spikes between 6 and 11 seconds in the $\rho = 0.2\,1/\mathrm{m}^2$-system correspond to breaking apart of a stripe and emerging of new stripe in the range $x = [0.14, 0.2]\,\mathrm{m}$ (figure 3.41c). In contrast, merging and branching in 3.41d does not seem to have any impact on the diffusion coefficient. For $\rho = 0.23\,\mathrm{m}^2$ and $\rho = 0.46\,\mathrm{m}^2$ the mean square displacement D takes a similar niveau quite fast, and towards the end ($t \geq 18s$) the system $\rho = 0.11\,\mathrm{m}^2$ seems to join this niveau. Combined with the previous results, this may indicate that for stripe forming systems, the diffusion coefficient assumes the same niveau, independent of external influences and packing fraction, except too dilute or dense systems.

3.5.5. Long term behaviour

To analyse the long term behaviour of the shaken monolayer, the initial setup is run for 2500 seconds. Its packing fraction is $\rho = 0.2299$, and the driving parameters are $\mathcal{A} = 0.025\,\mathrm{m}$ and $\nu = 20\,\mathrm{Hz}$.

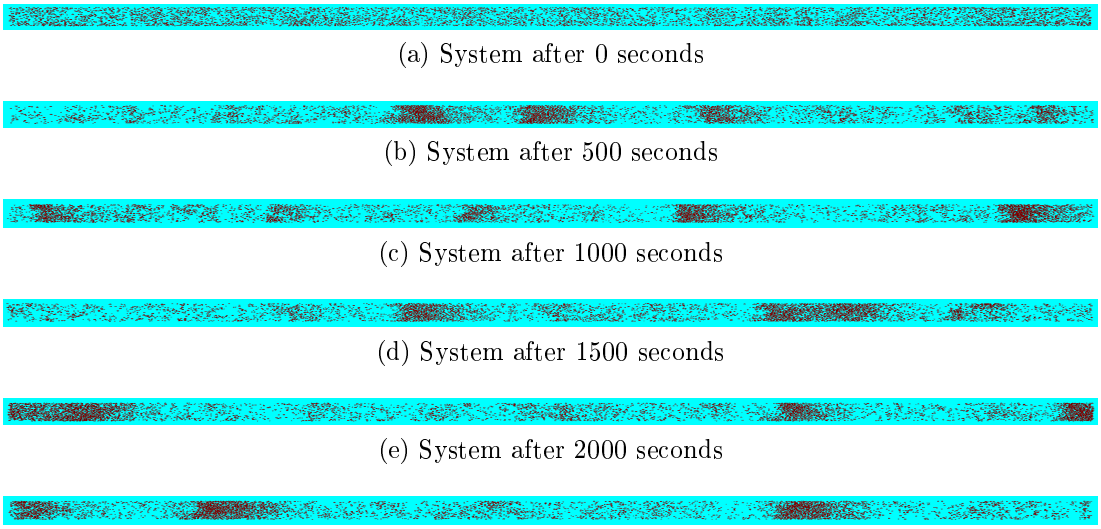

(a) System after 0 seconds

(b) System after 500 seconds

(c) System after 1000 seconds

(d) System after 1500 seconds

(e) System after 2000 seconds

(f) System after 2500 seconds

Figure 3.43.: Evolution of the system over 2500 seconds.

Analysing the density profile, it immediately becomes clear that the patterns are not stable, instead they break up after some time. There is always at least one major stripe in the system, accompanied by several minor clusters. The overall pattern appears to be self-similar with respect to time.
The motion of the tracer particle is recorded for the first 400 seconds (fig 3.44).

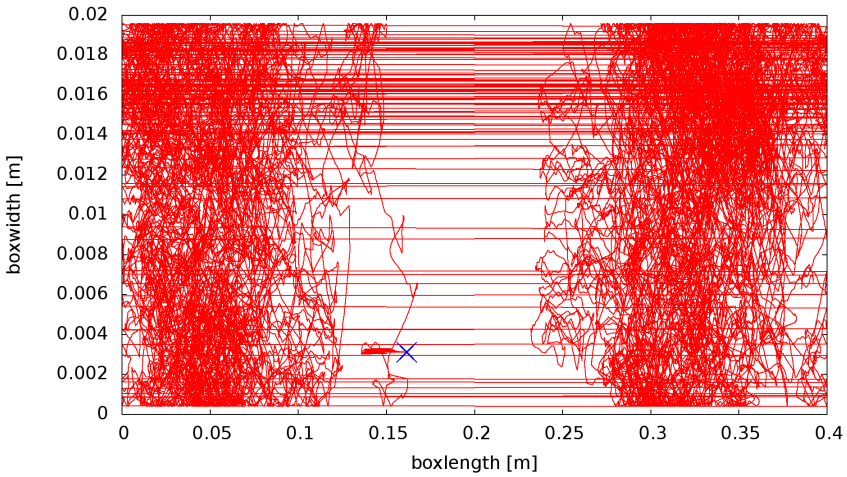

Figure 3.44.: Motion of the tracer particle in the first 400 seconds of the simulation.

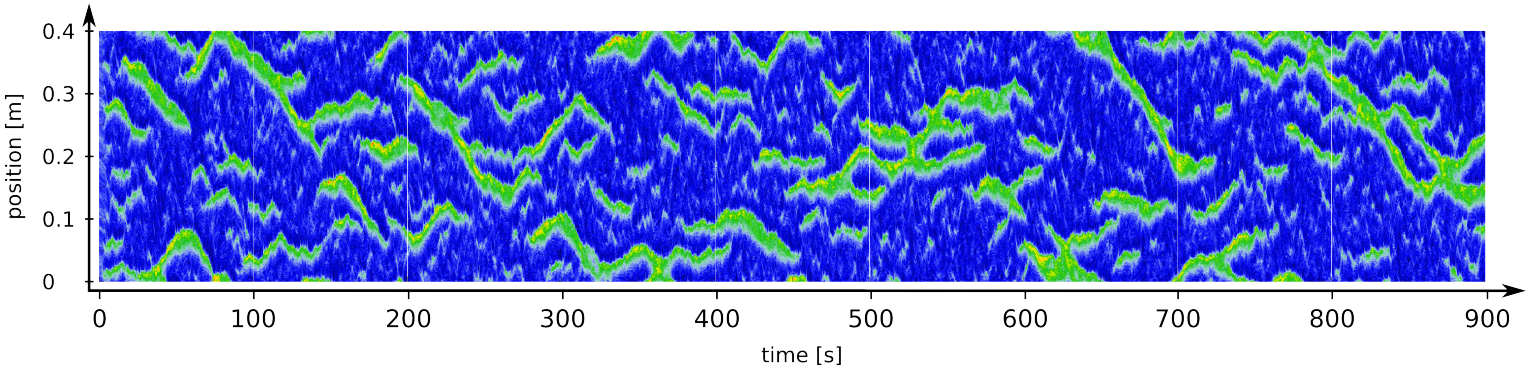

(a)

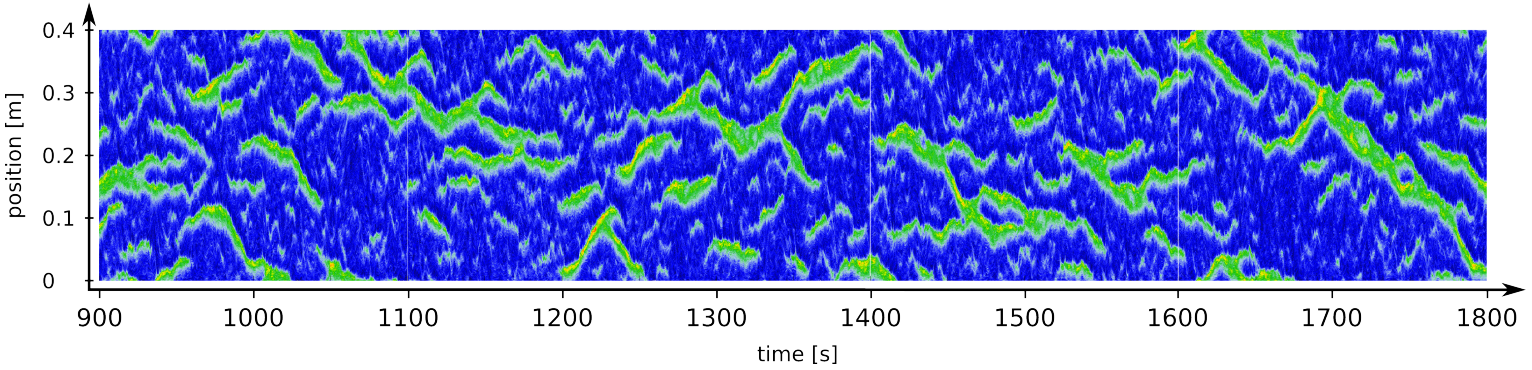

(b)

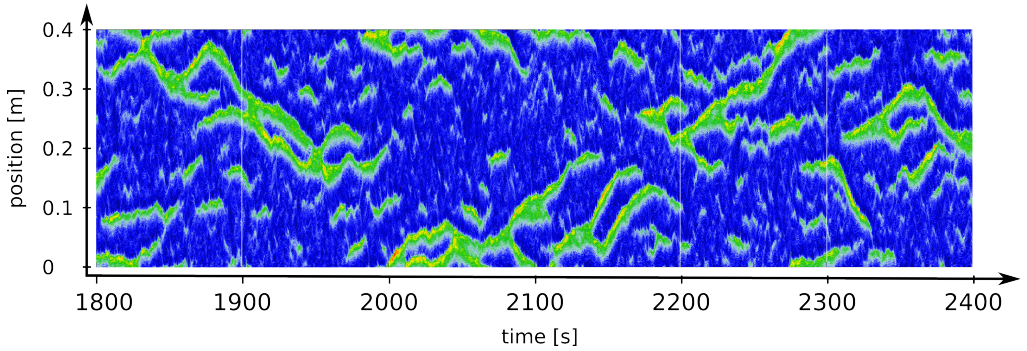

(c)

Figure 3.45.: Long term behaviour of the density distribution. For clarity the plot has been split.

The mean square displacement D, after the initial formation of the stripes, shows an undulating profile with two levels (fig 3.46).

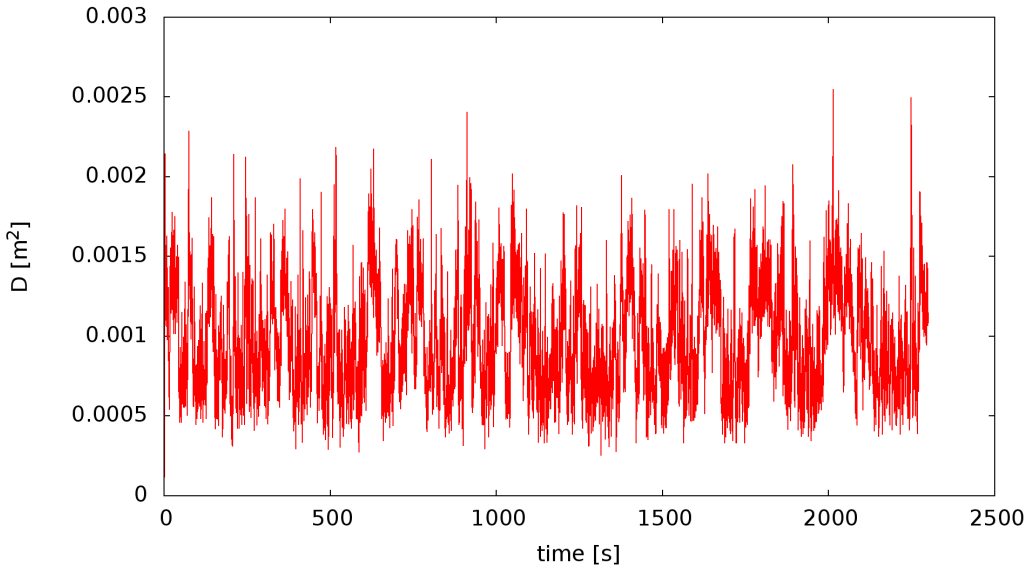

Figure 3.46.: Longterm evolution of the mean square displacement.

The autocorrelation function

$$C(t) = \sum_{t'=0}^{N-1} D(t)D(t+t'), \tag{3.32}$$

of the mean square displacement D alone shows no features, but the density profile suggest the existence of a maximum around $t = 100\,\mathrm{s}$ (fig 3.47), corresponding with the mean lifetime of the stripes.

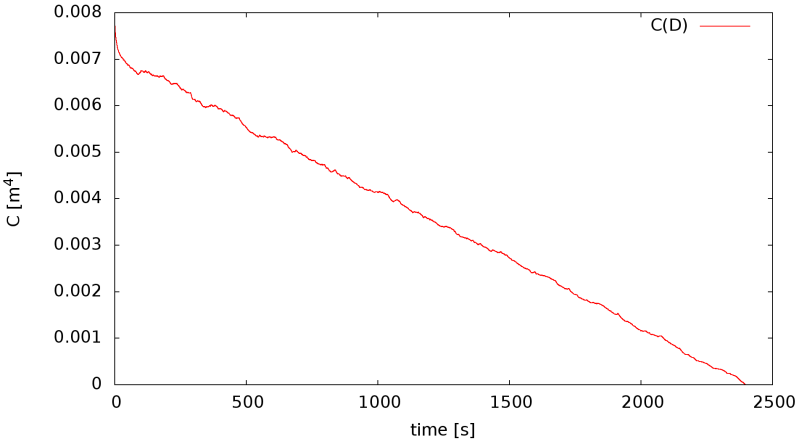

(a)

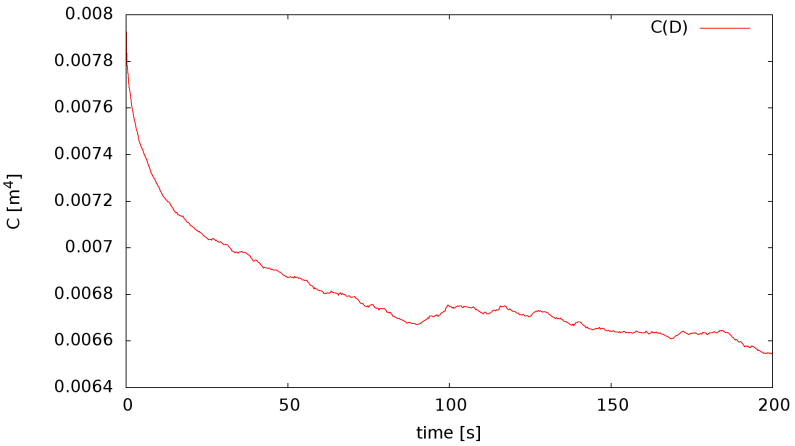

(b)

Figure 3.47.: Autocorrelation of the mean square displacement D.

4. Negative coefficient of normal restitution

Recently, negative values for the coefficient of normal restitution have been observed for oblique impacts of nanoparticles [52]. While colliding nanoparticles represent a highly specific system including e.g. adhesive forces or restructuring, we show that negative coefficients of normal restitution are an absolutely general phenomenon arising from plain geometry. Negative coefficients of normal restitution may be observed for *all* kinds of collisions which are governed by *finite* interaction forces. Whereas negative coefficients of normal restitution may appear quite artificial, they reveal a commonly neglected deficiency of the widely used hard sphere model.
This chapter was written in collaboration with Patric Müller and Thorsten Pöschel.

4.1. Introduction

Both, Kinetic Theory of granular matter, based on the Boltzmann equation [34, 66, 86], as well as highly efficient event-driven Molecular Dynamics (eMD) simulation of granular matter [8, 16, 87] are based on the hard sphere model (HSM) of particle collisions. Hard sphere collisions are characterized by delta-shaped interaction forces. While the particles instantaneously exchange momentum during a collision, their positions hence remain unchanged. Due to the instantaneous character of the collisions, the dynamics of a hard sphere system is represented by a *sequence* of *binary* collisions (events), which is the idea of eMD. As only momentum is transferred during a collision, each event is characterized by only two scalar values: The coefficient of normal restitution ε_n relating post- and precollisional normal part of the particles relative velocity and the coefficient of tangential restitution relating the corresponding tangential components. For two hard spheres i and j located at $\mathbf{r}_i$ and $\mathbf{r}_j$ travelling at velocities $\dot{\mathbf{r}}_i$ and $\dot{\mathbf{r}}_j$, the coefficient of normal restitution for hard spheres is, thus, defined by

$$\left(\dot{\mathbf{r}}'_i - \dot{\mathbf{r}}'_j\right) \cdot \hat{e}_r^{\,0} = -\varepsilon_n^{\mathrm{HS}} \left(\dot{\mathbf{r}}_i^0 - \dot{\mathbf{r}}_j^0\right) \cdot \hat{e}_r^0 \,, \tag{4.1}$$

where X^0 indicates the value of the quantity X at the moment of impact and X' the corresponding value at the instant of time τ, where the collision terminates. $\hat{e}_r \equiv (\mathbf{r}_j - \mathbf{r}_i)/\left|\mathbf{r}_j - \mathbf{r}_i\right|$ denotes the unit vector pointing from particle i to particle j. Note, that due to the instantaneous character of hard sphere collisions, the normal vector $\hat{e}_r$ remains unchanged during a collision ($\hat{e}'_r \equiv \hat{e}_r^0$, $\hat{e}_r^0$ on both sides of Eq. (4.1)). For soft sphere collisions characterized by finite interaction forces and finite contact durations this may be invalid: Oblique impacts may lead to a reorientation of the normal vector ($\hat{e}'_r \neq \hat{e}_r^0$). For soft spheres the coefficient of normal restitution is hence given by

$$\left(\dot{\mathbf{r}}'_i - \dot{\mathbf{r}}'_j\right) \cdot \hat{e}'_r = -\varepsilon_n \left(\dot{\mathbf{r}}_i^0 - \dot{\mathbf{r}}_j^0\right) \cdot \hat{e}_r^0 \,. \tag{4.2}$$

Disregarding some current approaches [76], the reorientation angle

$$\varphi' \equiv \cos^{-1}(\hat{e}_r^0 \cdot \hat{e}'_r) \tag{4.3}$$

is not available in classical eMD algorithms. It is commonly assumed to be negligible and the definition Eq. (4.1) is used without further consideration.

In textbooks, the coefficient of normal restitution $\varepsilon_n^{\mathrm{HS}}$ as defined in Eq. (4.1) is assumed to be a material constant attaining values ranging from zero to unity ($\varepsilon_n^{\mathrm{HS}} \in [0;1]$). Opposing this, it has been shown long time ago that the coefficient of normal restitution $\varepsilon_n^{\mathrm{HS}}$ may be a function of the impact velocity [13]. While more recent studies demonstrate that the coefficient of normal restitution may be a a fluctuating quantity [55] even exceeding unity [60, 32], it was still believed to not fall below zero. For oblique impacts of nanoclusters it was recently shown that the reorientation Eq. (4.3) may lead to negative values for the coefficient of normal restitution defined by Eq. (4.1) [52]. This surprising effect was attributed to the softness of nanoclusters leading to relatively long contact durations τ, which, in turn, may lead to a significant reorientation of the particles normal vector during a collision.
In this work we show that negative coefficients of normal restitution are not restricted to high speed impacts of nanoclusters. Quite the opposite, they are an absolutely general phenomenon which may appear for *all* collisions whose dynamics are governed by *finite* interaction forces leading to finite durations of contact. Provided *finite* contact duration, we show that the origin of the effect is plain geometry. Independent of material properties we *always* find a collision geometry leading to negative values of $\varepsilon_n^{\mathrm{HS}}$. To provide evidence for our findings we exemplarily discuss two specific interaction forces for spherical particles: The linear dashpot model and viscoelastic spheres. Additionally we address the influence of friction.

4.2. Collision of Smooth Spheres

For the collision of two smooth spheres with the masses m_i and m_j located at $\mathbf{r}_i$ and $\mathbf{r}_j$ it's reasonable to switch to center of mass and relative coordinates. The relative motion seperates from the center of mass motion and contains the entire collision details:

$$m_{\mathrm{eff}}\ddot{\mathbf{r}} = \mathbf{F}\,, \tag{4.4}$$

with the relative coordinate $\mathbf{r} \equiv \mathbf{r}_j - \mathbf{r}_i$ and the effective mass $m_{\mathrm{eff}} \equiv m_i m_j/(m_i+m_j)$. As described in [75], the interaction force $\mathbf{F}$ exclusively acts in the direction of the inter-center unit vector for frictionless collisions: $\mathbf{F} = F_n \hat{e}_r$. This implies that the particles rotation is not affected and (orbital) angular momentum is conserved during the collision. The complete collision hence takes place in a plane perpendicular to the conserved angular momentum $\mathbf{L}$

$$\mathbf{L} = m_{\mathrm{eff}}\, \mathbf{r} \times \dot{\mathbf{r}} \equiv L\hat{e}_L\,. \tag{4.5}$$

In this collision plane we rewrite the equation of motion Eq. (4.4) in polar coordinates $\{r, \varphi\}$ (see Fig. 4.1):

$$m_{\mathrm{eff}} r^2 \dot{\varphi} = L \tag{4.6a}$$

$$m_{\mathrm{eff}}\ddot{r} = F_c + F_n = m_{\mathrm{eff}} r\dot{\varphi}^2 + F_n\,, \tag{4.6b}$$

with the centrifugal force F_c. Together with the inital conditions

$$r(0) = r^0\,, \qquad \dot{r}(0) = \dot{r}^0\,, \qquad \varphi(0) = 0\,, \tag{4.7}$$

Eq. (4.6) fully describes the collision dynamics for an arbitrary normal force F_n. The collision terminates at time $t = \tau$ where [88, 89]

$$\dot{r}(\tau) > 0 \quad \text{and} \quad F_n = 0. \tag{4.8}$$

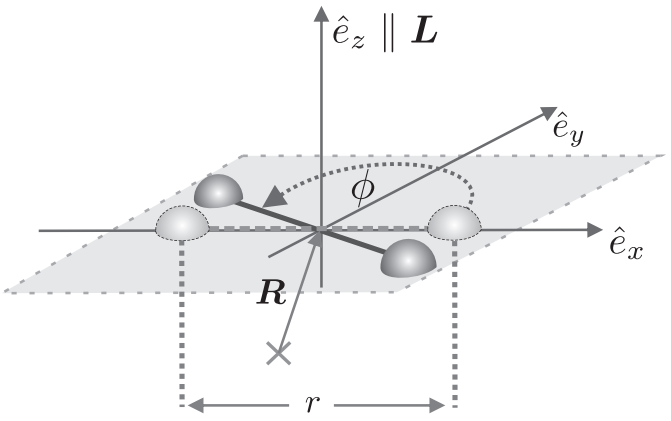

Figure 4.1.: Illustration of the used polar coordinates (see text)

4.3. Negative Values for the Coefficient of Normal Restitution

Expressed in the polar coordinates described in Sec. 4.2 the relative vector $\mathbf{r}$ and the corresponding relative velocity $\dot{\mathbf{r}}$ are given by

$$\mathbf{r} = r\hat{e}_r \quad \text{and} \quad \dot{\mathbf{r}} = \dot{r}\hat{e}_r + r\dot{\varphi}\hat{e}_\varphi \quad \text{respectively,} \tag{4.9}$$

where

$$\hat{e}_r = \begin{pmatrix} \cos\varphi \\ \sin\varphi \\ 0 \end{pmatrix} \quad \text{and} \quad \hat{e}_\varphi = \begin{pmatrix} -\sin\varphi \\ \cos\varphi \\ 0 \end{pmatrix}. \tag{4.10}$$

With this the coefficient of normal restitution according to the hard sphere definition Eq. (4.1) reads

$$\varepsilon_n^{\mathrm{HS}} = \underbrace{-\frac{\dot{r}'}{\dot{r}^0}}_{>0}\cos\varphi' + \underbrace{\frac{r'\dot{\varphi}'}{\dot{r}^0}}_{\leq 0}\sin\varphi' \tag{4.11}$$

using polar coordinates.

As at the beginning of a collision the particles are approaching and seperating at the end of the collision, the factor for the cosine term needs to be positive. By definition the angular velocity is positive at the end of the collision as well as the distance between both particles. As the particles are approaching at the beginning of the collision, we have $\dot{r}^0 < 0$ and the factor for the sine-term is always negative. This implies that negative values for $\varepsilon_n^{\mathrm{HS}}$ are possible *exclusively* for finite reorientations φ'.
For *any* finite interaction force, the contact duration τ is finite. In this case Eq. (4.6a) indicates that finite rotation angles are unavoidable for non-zero (orbital) angular momentum L. Which, according to Eq. (4.5), is fulfilled as soon a $\mathbf{r}$ and $\dot{\mathbf{r}}$ are not parallel. This implies, that negative values for the coefficient of normal restitution have to be expected for *any* eccentric collision governed by finite interaction forces.

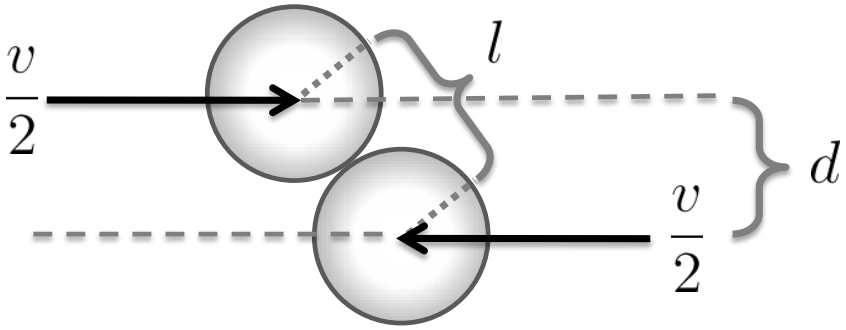

Figure 4.2.: Eccentric binary collision of spheres.

As described in Sec. 4.2 the collision of two frictionless spheres *always* takes place in a plane. It's hence possible to fix the collision scenario shown in Fig. 4.2 without loss of generality, which allows for a more vivid description of the impact eccentricity

$$e \equiv \frac{d}{l} \,. \tag{4.12}$$

From the definition of the angular momentum $\mathbf{L}$ (Eq. (4.5)) and geometry, we find

$$L = m_{\mathrm{eff}}\, dv \quad \text{and} \quad \dot{r}^0 = -v\sqrt{1-e^2} \tag{4.13}$$

for the collision setup shown in Fig. 4.2. As L is conserved Eq. (4.6a) yields

$$r\dot{\varphi} = \frac{d\, v}{r} \tag{4.14}$$

and the factor of the sine-term in Eq. (4.11) thus reads

$$\frac{r'\dot{\varphi}'}{\dot{r}^0} = -\frac{d}{r'\sqrt{1-e^2}} \,. \tag{4.15}$$

For elastic particles we have $r = r' = l$ and, of course, $\varepsilon_n = 1$ (see Eq. (4.2)) which implies $\dot{r}^0 = -\dot{r}'$. With this, Eq. (4.11) facilitates to

$$\varepsilon_n^{\mathrm{HS}} = \cos\varphi' - \frac{1}{\sqrt{(1/e)^2 - 1}} \sin\varphi' \,. \tag{4.16}$$

Fig. 4.3 shows $\varepsilon_n^{\mathrm{HS}}$ for elastic particles as a function of the reorientation angle φ' (Eq. (4.3)).

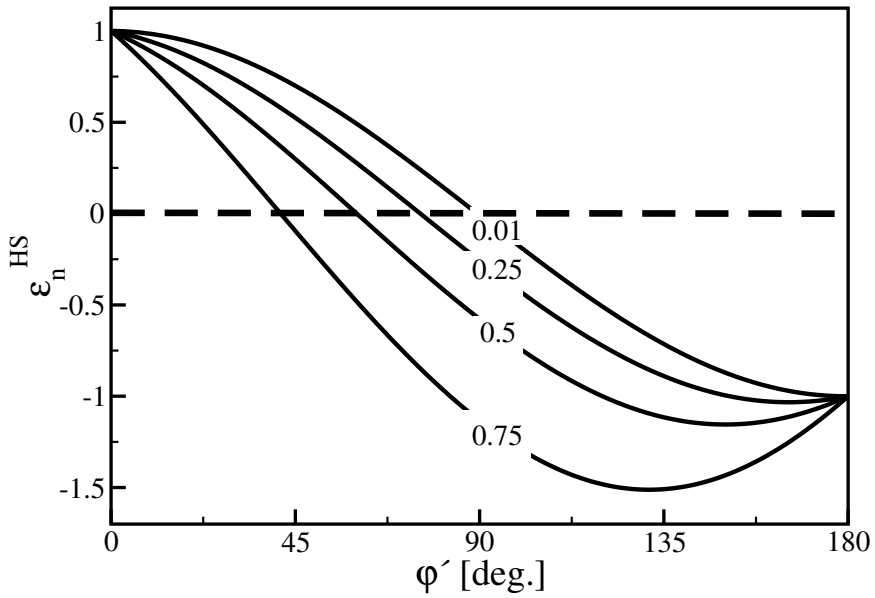

Figure 4.3.: Coefficient of normal restitution $\varepsilon_n^{\mathrm{HS}}$ (hard sphere definition, Eq. (4.1)) of elastic particles as a function of the reorientation angle φ' for various impact eccentricities $e \equiv d/l$ (see Eq. (4.16)). Labels: Impact eccentricity e.

If the hard sphere definition Eq. (4.1) for the coefficient of normal restitution is applied to oblique collisions of soft spheres characterized by *finite* interaction forces and, as a consequence, *finite* contact durations, Fig. 4.3 reveals two effects:

1. $\varepsilon_n^{\mathrm{HS}}$ is not a constant. Even for elastic particles. Besides material properties and impact velocity, it depends on the impact eccentricity and hence on the collision geometry.

2. Depending on the impact eccentricity, $\varepsilon_n^{\mathrm{HS}}$ may attain negative values for *any* reorientation angle φ'.

Fig. 4.3 indicates that for a fixed impact eccentricity the value of $\varepsilon_n^{\mathrm{HS}}$ and especially its sign, are governed by the reorientation angle φ'. This raises the following question: Given an specific interaction force model governed by a set of parameters as well as impact velocity and eccentricity, what reorientation angle is to be expected? To answer this question we refer to Fig. 4.4. The curves shown there are exemplary. They have been obtained for a special force model and a special set of system parameters. Note that in spite of that the following discussion and concepts hold true for *any finite* interaction force.
Two contacting spheres form dumbbell-shaped body. As soon as the impact is eccentric ($e > 0$), this dumbbell starts rotating around its center of mass with an

angular velocity $\dot{\varphi}$ corresponding to the conserved angular momentum $\mathbf{L}$. The angular momentum increases linearly with the impact eccentricity e (dashed line in the intermediate panel of Fig. 4.4). According to Eq. (4.6a) this implies that $\dot{\varphi}$ is also growing with the impact eccentricity. Eq. (4.14) yields

$$\dot{\varphi} = \frac{dv}{r^2}. \tag{4.17}$$

If we assume small deformations, $r \approx l$, we have

$$\dot{\varphi} = \text{const.} \equiv \omega = e\,\frac{v}{l}. \tag{4.18}$$

This angular velocity, in turn, serves for finite reorientation angles φ' if only the contact duration is finite, which of course, holds for *all* finite interaction forces. For typical normal force models the contact duration is independent of the normal component of the impact velocity $|\dot{r}^0|$ (linear dashpot model Sec. 4.4.1) or a decreasing function of $|\dot{r}^0|$ (viscoelastic spheres Sec. 4.4.2). As $|\dot{r}^0|$ is a decreasing function of the impact eccentricity e (Eq. (4.13), top panel in Fig. 4.4, solid line), the contact duration is a decreasing function of the impact eccentricity (top panel in Fig. 4.4, dashed line)). Additionally, the rotation velocity is growing with the impact eccentricity. This serves for larger, effectively repulsive, centrifugal forces shortening the contact duration furthermore. Hence even for the linear dashpot model, the contact duration τ (see Eq. (4.8)) decreases with growing eccentricity. The resulting reorientation angle φ' as a function of the impact eccentricity is shown in the intermediate panel of Fig. 4.4. For $0 < e \lessapprox 0.8$ the increasing rotation velocity dominates, making φ' an increasing function of e. For $0.8 \lessapprox e < 1$, φ' decreases because the decrease of the contact duration becomes governing. According to Fig. 4.3, $\varepsilon_n^{\mathrm{HS}}$ is a monotonically decreasing function of φ' for reasonably small φ'. At first glance, $\varepsilon_n^{\mathrm{HS}}(e)$ should hence be decreasing for $0 < e \lessapprox 0.8$ and increasing for $0.8 \lessapprox e < 1$ respectively. But as also shown in Fig. 4.3 the slope of $\varepsilon_n^{\mathrm{HS}}$ becomes more and more negative for growing impact eccentricities e, which, in turn, overcompensates the decreasing reorientation angle for $0.8 \lessapprox e < 1$. As a result, $\varepsilon_n^{\mathrm{HS}}$ is a monotonically decreasing function of the impact eccentricity e (Fig. 4.3, lower panel, solid line). Even for completely elastic particles ($\varepsilon_n = const. = 1$, Fig. 4.3, lower panel, dashed line).
As a consequence of Eq. (4.8) the contact duration decreases with inelasticity. That is the reorientation angle decreases and hence the difference between ε_n and $\varepsilon_n^{\mathrm{HS}}(e)$ also reduces. The slope $\varepsilon_n^{\mathrm{HS}}(e)$ is thus reduced when compared to the corresponding undamped curve. For central impacts ($\varphi' = 0$) the hard sphere definition of the normal coefficient of restitution Eq. (4.1) degenerates to its general definition Eq. (4.2):

$$\varepsilon_n^{\mathrm{HS}} = -\frac{\dot{r}'}{\dot{r}^0}\,, \tag{4.19}$$

wich, of course, is smaller than unity for inelastic collisions and decreases with growing inelasticity. That is, the $\varepsilon_n^{\mathrm{HS}}(e)$-curves for very inelastic systems always lie below the corresponding ones for lower inelasticty. As these curves additionaly have different

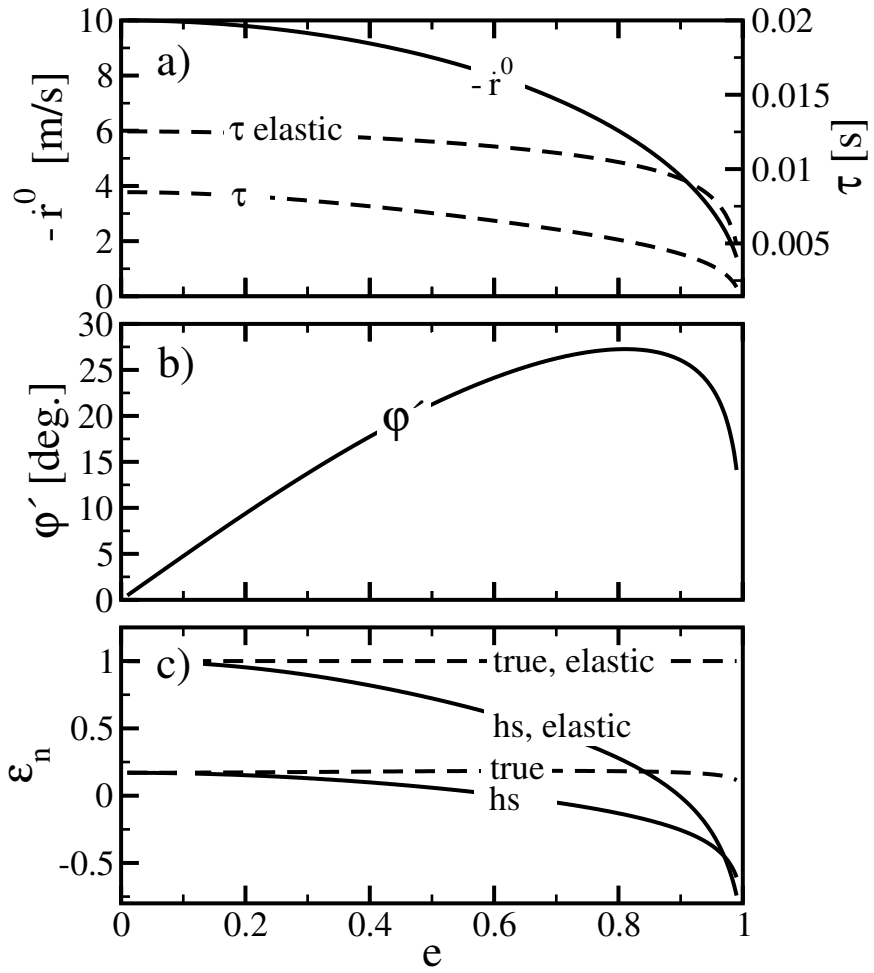

Figure 4.4.: Abscissa of all panels: Impact eccentricity $e \equiv d/l$. **a)** Left ordinate: Normal component $\dot{r}^0$ of the relative velocity of the two colliding spheres at the instant of impact. Right ordinate: Contact duration τ **b)** Left ordinate: Rotation φ' of the normal vector $\hat{e}_r$ at the end of the collision. **c)** Coefficient of Normal Restitution ε_n. Solid line: Hard sphere definition Eq. (4.1). Dashed line: Ratio of post- and precollisional normal component of the particles relative velocity Eq. (4.2). **Normal force model:** Linear Dashpot (see Sec. 4.4.1). **Parameters:** $k = 1.5e05$ N/m, $R = 0.1$ m, $\rho = 1140.0$ kg/m^3, $v = 10.0$ m/s, $\gamma = 0.0$ kg/s (elastic particles), $\gamma = 1000.0$ kg/s (lower/upper panel)

slopes they may eventually intersect for some impact eccentricity e (Fig. 4.3, lower panel).

Summing up we have: Two colliding particles form a dumbbell-shaped object. For oblique impacts this dumbbell rotates as long as the particles are in contact. As the contact duration is finite for all finite interaction forces, we have finite rotation angles for all eccentric impacts governed by finite interaction forces. Assuming small

deformations, the value of the reorientation angle φ' is determined by the ratio μ of the contact duration τ and the time $T_{\text{rot}} = 2\pi/\omega$ the dumbbell would need for a full rotation:

$$\mu \equiv \frac{\tau\omega}{2\pi}\,, \quad \varphi' = \mu\, 2\pi\,. \tag{4.20}$$

In turn, the coefficient of normal restitution according to the hard sphere definition Eq. (4.1) varies with the reorientation angle and, thus, depends on the collision geometry. Along these lines, even negative values for $\varepsilon_n^{\text{HS}}$ are *always* possible: Independent of the interaction force model and the system parameters we always find a critical impact eccentricity from which on we have $\varepsilon_n^{\text{HS}} < 0$.
In the next section we illustrate our findings for two widely used interaction force models. For booth models we present exhaustive parameter studies. These highlight negative values $\varepsilon_n^{\text{HS}}$, or more general the geometry dependence of $\varepsilon_n^{\text{HS}}$, as a significant, far reaching effect.

4.4. Simulation Results

4.4.1. Linear Dashpot Model

Within the linear dashpot model, the normal component of the interaction force is given by

$$F_n = k(l - r) - \gamma\dot{r} \tag{4.21}$$

(see [49, 87]). Neglecting centrifugal forces ($e = 0$), for elastic collisions, $\gamma = 0$, the contact duration τ reads

$$\tau = 2\pi\sqrt{m_{\text{eff}}/k}. \tag{4.22}$$

If we further assume small deformations ($r \approx l$), according to Eq. (4.20) we have

$$\mu = e\,\frac{v}{l}\sqrt{\frac{m_{\text{eff}}}{k}} \tag{4.23}$$

and the reorientation angle is approximately given by

$$\varphi' = \mu\, 2\pi = 2\pi\, e\frac{v}{l}\sqrt{\frac{m_{\text{eff}}}{k}}\,. \tag{4.24}$$

According to Fig. 4.3, $\varepsilon_n^{\text{HS}}$ is a monotonically decreasing function of the reorientation φ' for fixed impact eccentricities and reasonable rotation angles $\varphi' \in [0°, 90°]$. That is, for elastic particles, the difference of $\varepsilon_n^{\text{HS}}$ from $\varepsilon_n = 1$ increases with the reorientation angle φ'. Together with the core statement of Sec. 4.3 that $\varepsilon_n^{\text{HS}}$ is a decreasing function of the impact eccentricity e, we now use Eq. (4.24) to discus Fig. 4.5 and Fig. 4.6.
The lower panel of Fig. 4.5 displays $\varepsilon_n^{\text{HS}}(e)$ for various spring constants k for elastic particles. As predicted by Eq. (4.24), the difference of $\varepsilon_n^{\text{HS}}(e)$ from $\varepsilon_n = 1$ grows with decreasing k. The upper panel shows $\varepsilon_n^{\text{HS}}(e)$ for fixed k but various damping

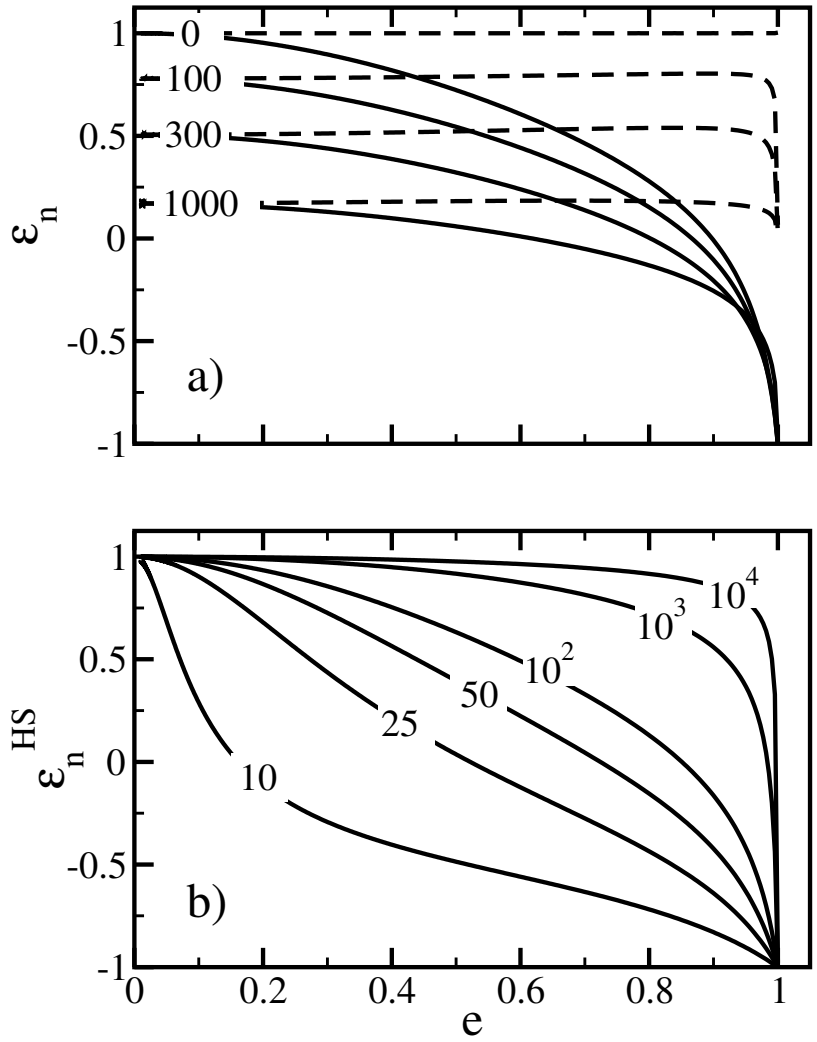

Figure 4.5.: Abscissa of both panels: Impact eccentricity $e \equiv d/l$. **a)** Ordinate: Coefficient of normal restitution according to the hard sphere definition (solid lines) and the ratio of post- and precollisional normal component of the particles relative velocity (dashed lines) for various damping constants γ. Labels: γ [kg/s]. **b)** Ordinate: Coefficient of Normal Restitution ε_n (hard sphere definition) for various spring constants k. Labels: k [N/m]. **Normal force model:** Linear Dashpot. **Parameters:** $k = 1.5e05$ N/m (top panel), $R = 0.1$ m, $\rho = 1140.0$ kg/m^3, $v = 10.0$ m/s, $\gamma = 0.0$ kg/s (elastic particles, lower panel)

coefficients γ. It exemplifies the influence of damping detailed in Sec. 4.3 (Fig. 4.4, lower panel).

The same line of reasoning explains Fig. 4.6. According to Eq. (4.24), the reorientation angle grows with the impact velocity. The $\varepsilon_n^{\mathrm{HS}}(e)$-curves for higher impact velocity hence attain smaller values than those for lower impact velocities (see Fig. 4.6, top panel). As $l = 2R$, where R indicates the particle radius, the reorientation angle

increases with growing l or R respectively, as well as with growing material densities ρ ($m_{\text{eff}} \propto \rho$). The $\varepsilon_n^{\text{HS}}(e)$-curves for higher R or ρ thus display smaller values than the curves for the corresponding lower values (see Fig. 4.6, bottom/intermediate panel).

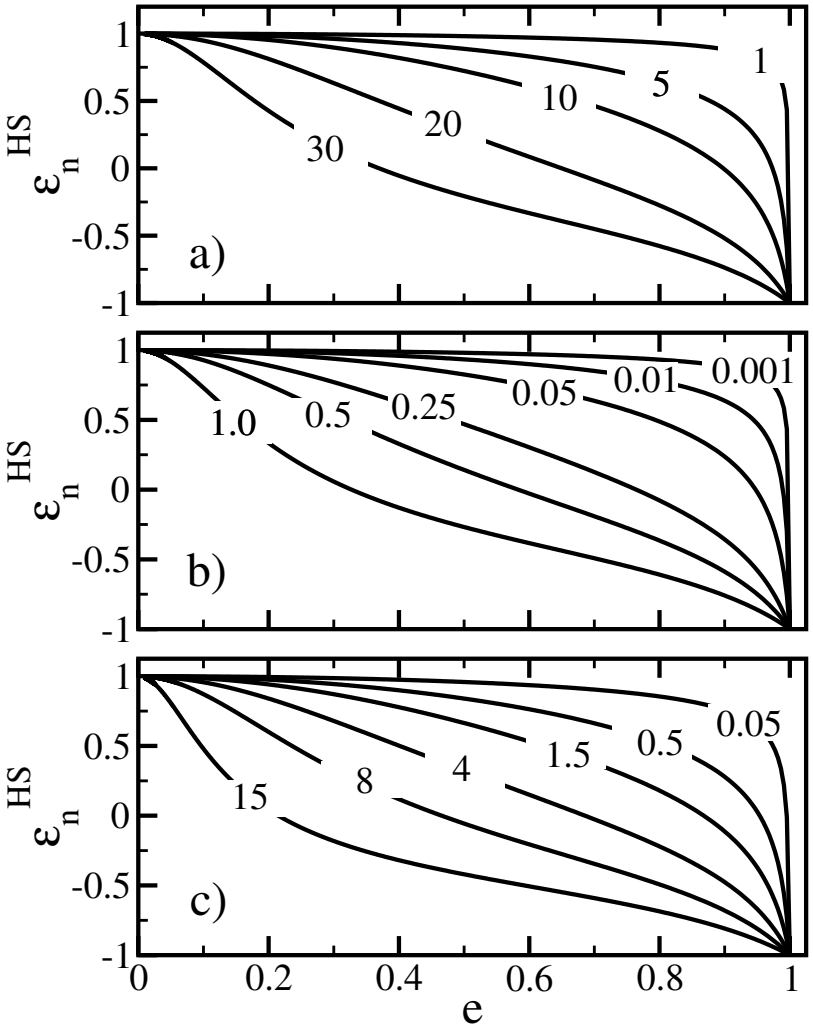

Figure 4.6.: Abscissa of all panels: Impact eccentricity $e \equiv d/l$. Ordinate of all panels: Coefficient of Normal Restitution ε_n (hard sphere definition) **a)** $\varepsilon_n(e)$ for various impact velocities v. Labels: v [m/s]. **b)** $\varepsilon_n(e)$ for various particle radii R. Labels: R [m]. **c)** $\varepsilon_n(e)$ for various densities ρ. Labels: ρ [10^3 kg/m^3]. **Normal force model:** Linear Dashpot. **Parameters:** $k = 1.5e05$ N/m, $R = 0.1$ m (bottom/top panel), $\rho = 1140.0$ kg/m^3 (intermediate/top panel), $v = 10.0$ m/s (bottom/intermediate panel), $\gamma = 0.0$ kg/s (elastic particles)

4.4.2. Viscoelastic Spheres

This section is along the lines of Sec. 4.4.1. Only the normal force model is now changed to the one of viscoelastic spheres [64]:

$$F_n = F_n^{\mathrm{el}} + F_n^{\mathrm{dis}} = \rho_{\mathrm{el}}(l-r)^{3/2} - \frac{3}{2}A\rho_{\mathrm{el}}\dot{r}\sqrt{l-r}\,, \tag{4.25}$$

where

$$\rho_{\mathrm{el}} \equiv \frac{2Y\sqrt{R_{\mathrm{eff}}}}{3(1-\nu^2)} \tag{4.26}$$

and Y, ν and R_{eff} denote the Young's modulus, the Poisson's ratio and the effective radius $R_{\mathrm{eff}} = R_iR_j/(R_i+R_j)$, respectively. The elastic part F_n^{el} of this widely used [31, 3, 49] collision model is given by the Hertz' contact force of two colliding elastic spheres [30]. The dissipative part, F_n^{dis}, was first motivated in [25] and then rigorously derived in [64] and [92], where only the approach in [64] leads to an analytic expression for the parameter A, being a function of the elastic and viscous material parameters.

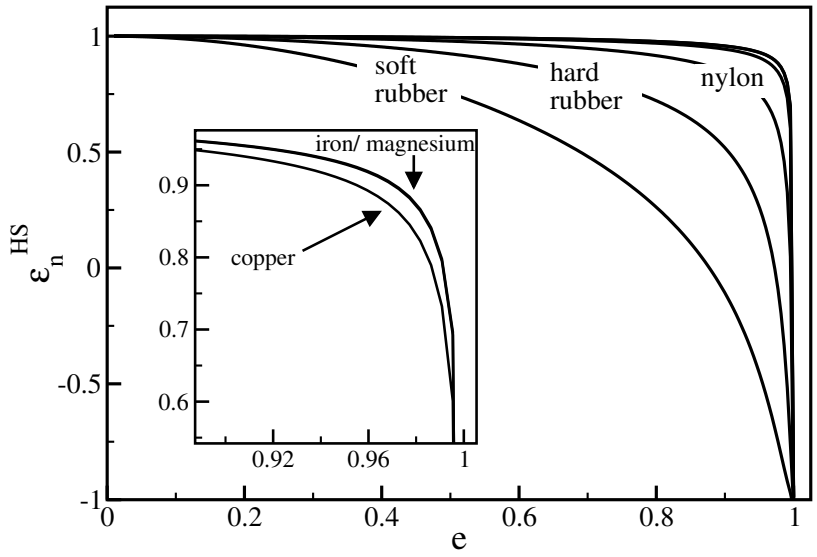

Figure 4.7.: Coefficient of Normal Restitution ε_n (hard sphere definition) for various materials. The inset shows a magnification of the main panel. **Normal force model:** Viscoelastic spheres. **Parameters:** Material parameters as indicated in Tab. 4.1. $R = 0.1$ m, $v = 10.0$ m/s, $A = 0.0$ s (elastic particles)

Fig. 4.7 displays the coefficient of normal restitution $\varepsilon_n^{\mathrm{HS}}$ according to its hard sphere definition as a function of the impact eccentricity e for various real life materials. Extending the statements of [52] it illustrates that negative values for $\varepsilon_n^{\mathrm{HS}}$ are not restricted to high speed collision of nanoclusters including adhesive forces. The effect is also significant for *common* collisions of *macroscopic* particles consisting of *common* materials.

Disregarding centrifugal forces, the contact duration reads

$$\tau = R\frac{\left[\sqrt{2}\pi\rho(1-\nu^2)\right]^{\frac{2}{5}}}{Y^{\frac{2}{5}}\left(-\dot{r}^0\right)^{\frac{1}{5}}} \tag{4.27}$$

for completely elastic collisions ($A = 0$) [89]. According to Eq. (4.20), again assuming small deformations ($r \approx l$) and additionally using Eq. (4.13) we find

$$\varphi' = \frac{\pi^{\frac{2}{5}}}{2^{\frac{4}{5}}}\,\frac{e}{\left(\sqrt{1-e^2}\right)^{\frac{1}{5}}}\,v^{\frac{4}{5}}\,\left[\frac{\rho\,(1-\nu^2)}{Y}\right]^{\frac{2}{5}}\,. \tag{4.28}$$

Just like in Sec. 4.4.1 we now use Eq. (4.28) to discuss the simulation results Fig. 4.8 and Fig. 4.9. According to Sec. 4.3 the coefficient of normal restitution $\varepsilon_n^{\mathrm{HS}}$ (hard sphere definition), is a monotonically decreasing function of the impact eccentricity e. According to Fig. 4.3, the $\varepsilon_n^{\mathrm{HS}}$-curves for parameters leading to large reorientation angles φ' always attain smaller values than these for parameters leading to smaller φ', for reasonably small reorientation angles. With this in mind, Eq. (4.28) easily explains the top panel of Fig. 4.8 and all panels of Fig. 4.9. Note that for common materials, the Poisson's ratio ν is of minor importance. It only becomes influencing for highly auxetic materials ($\nu \approx -1$, top panel of Fig. 4.9).

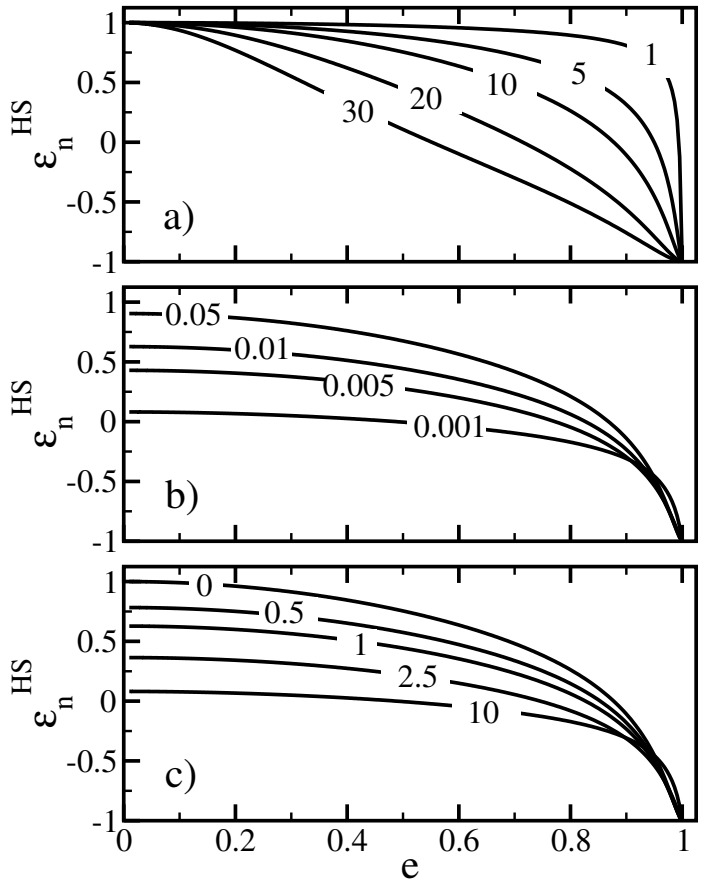

Figure 4.8.: Abscissa of all panels: Impact eccentricity $e \equiv d/l$. Ordinate of all panels: Coefficient of Normal Restitution ε_n (hard sphere definition) **a)** $\varepsilon_n(e)$ for various impact velocities v. Labels: v[m/s]. **b)** $\varepsilon_n(e)$ for various particle radii R. Labels: R [m]. **c)** $\varepsilon_n(e)$ for various dissipative constants A. Labels: A [10^{-3} s]. **Normal force model:** Viscoelastic spheres. **Parameters:** Material: Soft silicon rubber (see Tab. 4.1). $R = 0.1$ m (bottom/top panel), $v = 10.0$ m/s (bottom/intermediate panel), $A = 0.0$ s (top panel,elastic particles), $A = 1.0 \cdot 10^{-4}$ s (intermediate panel)

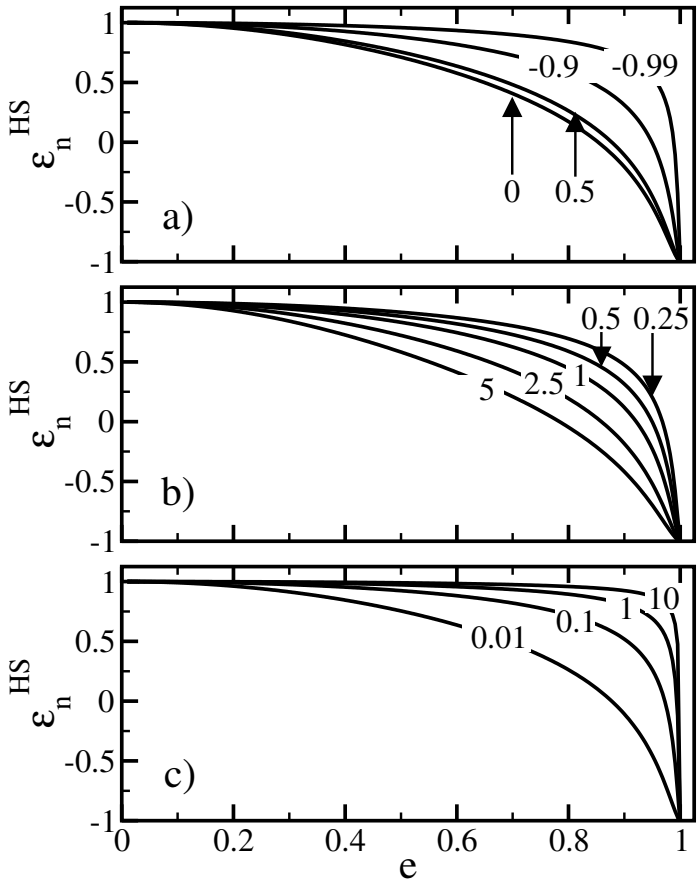

Figure 4.9.: Abscissa of all panels: Impact eccentricity $e \equiv d/l$. Ordinate of all panels: Coefficient of Normal Restitution ε_n (hard sphere definition) **a)** $\varepsilon_n(e)$ for various Poisson's ratios ν. Labels: ν. **b)** $\varepsilon_n(e)$ for various densities ρ. Labels: ρ [10^3 kg/m^3]. **c)** $\varepsilon_n(e)$ for various Young's modulus Y. Labels: Y [GPa]. **Normal force model:** Viscoelastic spheres. **Parameters:** $R = 0.1$ m, $Y = 0.01$ GPa (intermediate/top panel), $\rho = 2.0e3$ kg/m^3 (bottom/top panel), $\nu = 0.5$ (bottom/intermediate panel) $v = 10.0$ m/s, $A = 0.0$ s (elastic particles)

The lower panel of Fig. 4.8 again illustrates the influence of damping already described in Sec. 4.3 and Sec. 4.4.1. Interestingly Eq. (4.28) indicates that the reorientation angel and hence the value of $\varepsilon_n^{\mathrm{HS}}$ does not depend on the particle radius for elastic particles. For finite inelasticity A, the particle radius again influences via l and ρ_{el}. Hence, changing the particle radius of inelastic particles, has the same impact as changing the inelasticity itself (Fig. 4.8, intermediate panel).

Material	Youngs Modulus [GaP]	Density [kg/m^3]	Poisson's Ratio
Iron	200.0	7870.0	0.291
Copper	110.0	8930.0	0.343
Magnesium	44.0	1740.0	0.35
Nylon	1.0	1020.0	0.4
Silicon rubber (hard)	0.1	2000.0	0.5
Silicon rubber (soft)	0.01	2000.0	0.5

Table 4.1.: Mechanical Properties of the used materials. Taken from [1]

4.5. The Role of Friction

So far we only considered smooth spheres where the interaction force between to colliding particles exclusively acts in normal direction ($\mathbf{F} = F_n \hat{e}_r$). In this section we address the influence of friction which acting in tangential direction ($\mathbf{F} = F_n \hat{e}_r + F_t \hat{e}_\varphi$). With this, the particles may exchange (intrinsic) angular momentum and we have two further degrees of freedom: The particles orientation Φ_i and the corresponding angular velocities $\dot{\Phi}_i$. Assuming no particle rotation at the instant of impact ($\dot{\Phi}_i^0 = 0$) the complete collision still takes place in a plane (see Sec. 4.2). This allows to stick with the notation of Sec. 4.2 as well as with the collision setup Fig. 4.2 without loss of generality. Including friction and hence tangential forces, the complete collision dynamics is governed by

$$\begin{aligned} \ddot{r} &= r\dot{\varphi}^2 + \frac{F_n}{m_{\text{eff}}} \\ \ddot{\varphi} &= -2\frac{\dot{r}\dot{\varphi}}{r} + \frac{F_t}{r m_{\text{eff}}} \\ \ddot{\Phi}_1 &= -\frac{1}{I_1}\frac{r}{2}F_t\,, \quad \ddot{\Phi}_2 = \frac{1}{I_2}\frac{r}{2}F_t\,, \end{aligned} \tag{4.29}$$

where $I_i = \frac{2}{5} m_i R_i^2$ is the moment of inertia of the corresponding sphere i. The corresponding initial conditions read

$$\begin{aligned} &r(0) = r^0\,, \quad \dot{r}(0) = \dot{r}^0\,, \quad \varphi(0) = 0\,, \\ &\dot{\varphi}(0) = \dot{\varphi}^0 = e\frac{v}{l}\,, \quad \Phi_i(0) = 0\,, \quad \dot{\Phi}_i(0) = 0\,. \end{aligned} \tag{4.30}$$

If we assume an infinite tangential force, the particles stick together on impact and a dumbbell shaped object is formed, where the particles themselves rotate at the same angular velocity as the whole dumbbell. The moment of inertia of this dumbbell (with respect to an axis through its center of mass, perpendicular to its axis of symmetry) reads $I_{\text{frict}} = \frac{14}{5} m R^2$, if we further assume identical particles. For smooth spheres (i.e. $\dot{\Phi}_i = 0$) the corresponding moment of inertia of the dumbbell is given by $I_{\text{smooth}} = 2mR^2$. As the total angular momentum L, consisting of orbital angular momentum of the two particles and the particle spin (intrinsic angular momentum), is conserved during the collision, the rotation speed of the dumbbell $\dot{\varphi}^0$ differs for smooth spheres and frictional spheres respectively. The ratio of both values reads

$$\frac{\dot{\varphi}^0_{\text{frict}}}{\dot{\varphi}^0_{\text{smooth}}} = \frac{I_{\text{smooth}}}{I_{\text{frict}}} = \frac{10}{14} \approx 0.71\,. \tag{4.31}$$

That is, for frictional particles, the rotation speed is reduced to approximately 70% of the corresponding rotational speed for smooth spheres. As the contact duration is only marginally affected by friction, this implies reduced reorientation angles in the case of friction: $\varphi'_{\text{frict}} \approx 0.71\, \varphi'_{\text{smooth}}$. This, in turn, implies that the difference of the $\varepsilon_n^{\text{HS}}(e)$ curves to the expected value $\varepsilon_n(e) = 1$ is smaller for the frictional

particles when compared to the case of smooth spheres. While *still being present*, the effect of negative coefficients of normal restitution is hence shifted to higher impact eccentricities by friction.
To illustrate these findings, as a particular tangential force, we discuss the model by Cundall and Strack where the tangential component of the impact is modeled by a linear spring elongating according to the tangential displacement, whose influence is limited by
Coulomb's friction law [68]:

$$F_t = -\text{sign}\left(v_{\text{rel,t}}\right) \cdot \min\left(\left|k^t \zeta\right|, \mu^t \left|F_n\right|\right) \ , \tag{4.32}$$

where

$$v_{\text{rel,t}} = r\dot{\varphi} + \frac{r}{2}\left(\dot{\Phi}_1 - \dot{\Phi}_2\right) \tag{4.33}$$

and

$$\zeta(t) = \int_{t'=0}^{t} v_{\text{rel,t}}\left(t'\right) \mathrm{d}t'. \tag{4.34}$$

k^t is the stiffness of the tangential spring and μ^t the friction parameter. Fig. 4.10

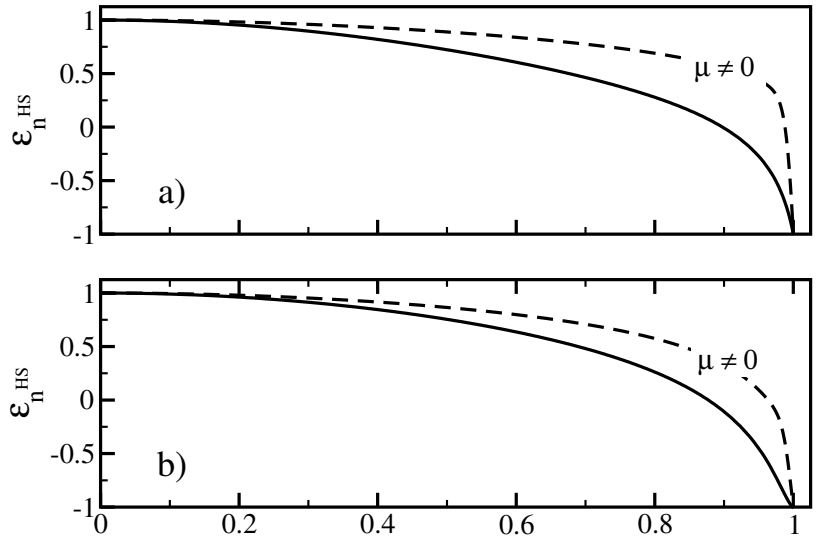

Figure 4.10.: Abscissa of both panels: Impact eccentricity $e \equiv d/l$. Ordinate of both panels: Coefficient of Normal Restitution ε_n (hard sphere definition). Influence of friction: Solid lines: Smooth spheres/no friction ($\mu = 0$). Dashed lines: friction included ($\mu \neq 0$). **a) Normal force model:** Linear dashpot. **Parameters:** $k^t = 1.0e05$ N/m, $\mu^t = 1.0e8$, $k = 1.5e05$ N/m, $R = 0.1$ m, $\rho = 1140.0$ kg/m^3, $v = 10.0$ m/s, $\gamma = 0.0$ kg/s (elastic particles) **b) Normal force model:** Viscoelastic spheres. **Parameters:** Soft silicon rubber (see Tab. 4.1) $k^t = 1.0e05$ N/m, $\mu^t = 1.0e8$ $R = 0.1$ m, $A = 0.0$ s (elastic collision), $v = 10.0$ m/s

displays the influence of friction for the two normal force models discussed before: The

linear dashpot model (upper panel) and viscoleastic spheres (lower panel). In both cases the above mechanism describes the result. Friction reduces the reorientation angle and hence the difference to the expected value of the coefficient of normal restitution $\varepsilon_n = 1$ is reduced.

4.6. Summary

During an instantaneous collision of hard spheres, the concerned particles exchange momentum while their positions remain unchanged. The full collision is hence described by two scalar values relating pre- and postcollisional particle velocities: The coefficient of normal and tangential restitution. Consequently, particle motion is not considered in the definition of these characteristic quantities.
As the hard sphere model claims to be a good approximation for the collision of spheres consisting of real life material, the values of the coefficients of restitution need to be determined according to the hard sphere definition, either experimentally (e.g. [20]) or theoretically by integration of verified interaction force laws (e.g. [89]). This has been done extensively for *central* impacts, realizing that the coefficients of restitution depend on the impact velocity and, thus, are no pure material properties. Assuming molecular chaos, most collisions in a granular system are eccentric. Within eMD or Kinetic Theory of granular matter, the hard sphere concept of the coefficient of restitution is hence frequently applied to oblique impacts without further consideration. Recently, for the very specific collision of nanoclusters [52], it was shown that this may be questionable. Using the hard sphere definition for measuring the coefficient of normal restitution lead to surprising results: Besides the impact velocity, the coefficient of normal restitution depend on the impact eccentricity, or, in other words, on the impact geometry. In the course of this geometry dependency, even negative values for the coefficient of normal restitution are attainable, which, of course, are not valid within eMD or Kinetic Theory.
In this work we have shown that both, the geometry dependency as well as negative values of the coefficient of normal restitution are not a peculiarity of colliding nanoclusters. Quite the opposite: The described effects are unavoidable for all kinds of collisions governed by finite interaction forces. For various force models, they are prominent for a huge parameter space, ranging orders of magnitude. Our work hence points towards sever deficiencies of the widely used hard sphere model. It calls for a simple criterion which allows to access the correctness of the hard sphere model and for more sophisticated collision rules including particle reorientation.

A. Appendix: Density distribution

In this appendix, the method used to determine the one-dimensional density field of a given distribution of particles, is discussed. This method in contrast to most others does not require the system to be spatially discretised by binning, but instead provides a scale free distribution.
In any two dimensional set of particles, each particle can be identified by two points in space, its position minus the radius r_- and its position plus the radius r_+, marking the beginning and the end of the particle (fig A.1 a). These two points then are assigned -1 for r_+ and $+1$ for r_-, which creates a distribution of ± 1's in any direction of the system (fig A.1 b). Those values then are summed up, beginning in one side of the system. That means, if any particles share a common range in the summation direction, the value in this range is increased by one for every particle in this range, and decreased if the overlap is gone (fig A.1 c). The result is a one-dimensional, binning free distribution of particle numbers.

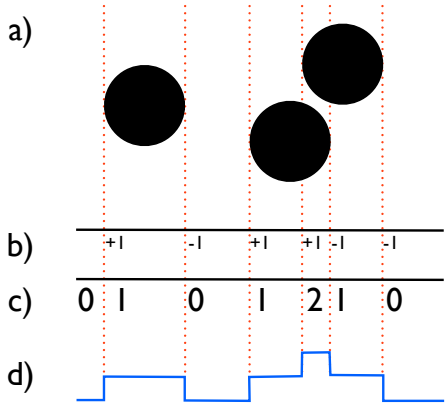

Figure A.1.: Schematic view of the calculation of the one-dimensional particle density

B. Acknowledgements

First of all, I wish to thank Prof. Dr. Thorsten Pöschel and Dr. Gerd Schröder-Turk for introducing me to granular media.
I want to thank Dr. Marcus Bannerman and Severin Strobl for their support, their help with creating the simulation and constructive suggestions in writing the thesis.
Furthermore, I owe thanks to Achim Sack, Jonathan Kollmer and Michael Heckel for their help with the experiment and carefully reading and commenting this thesis.
I am also grateful to Dr. Eric Ribeiro Parteli, Dr. Dan Serero, Patric Müller and Martin Tupy for helpful discussions and carefully reading and commenting this thesis.

Bibliography

[1] `http://www.matweb.com/`, 2012.

[2] `http://www.roymech.co.uk/Useful_Tables/Tribology/co_of_frict.htm`, 2012.

[3] A.B.Stevens and C.M.Hrenya. Comparison of soft-sphere models to measurements of collision properties during normal impacts. *Powder Technology*, 154:99, 2005.

[4] A.D.Rosato, K.J.Strandburg, F.Prinz, and R.H.Swendsen. Why the brazil-nuts are on top: Size segregation of particulate matter by shaking. *Phys. Rev. Lett.*, 58:1038, 1987.

[5] A.Kudrolli. Size separation in vibrated granular matter. *Rep. Prog. Phys.*, 67:209, 2004.

[6] A.Samadani and A.Kudrolli. Angle of repose and segregation in cohesive granular matter. *Phys. Rev. E*, 64:051301, 2001.

[7] A.Samadani, A.Pradhan, and A.Kudrolli. Size segregation of granular matter in silo discharges. *Phys. Rev. E*, 60:7203, 1999.

[8] B.D.Lubachevsky. How to simulate billards and similar systems. *J. Comp. Phys.*, 94(2):255, 1991.

[9] B.Drossel and T.Prellberg. Dynamics of a single particle in a horizontally shaken box. *Europhhys. J. B*, 1:533, 1998.

[10] B.J.Alder and T.E.Wainwright. Studies in molecular dynamics. 1. general method. *J. Chem. Phys.*, page 459, 1959.

[11] C.Huan, X.Yang, D.Candela, R.W.Mair, and R.L.Walsworth. Nmr experiments on a three-dimensional vibrofluidized granular medium. *Phys. Rev. E*, 69:41302, 2004.

[12] C.M.Pooley and J.M.Yeomans. Stripe formation in differentially forced binary systems. *Phys. Rev. Lett.*, 93:118001, 2004.

[13] C.V.Raman. The photographic study of impact at minimal velocities. *Phys. Rev.*, 12:442–447, 1918.

[14] D.C.Hong. Condensation of hard spheres under gravity. *Physica A*, 271:192, 1999.

[15] D.C.Hong, P.V.Quinn, and S.Luding. The reverse brazil-nut problem: Competition between percolation and condensation. *Phys. Rev. Lett.*, 86:3423, 2001.

[16] D.C.Rapaport. The event scheduling problem in molecular dynamic simulation. *Journal of Computational Physics*, 34:184, 1980.

[17] D.C.Rapaport. *The Art of Molecular Dynamics Simulation*. Cambridge University Press, 2009.

[18] D.Wolf. Friction in granular media. In H.J.Herrmann, J.-P.Hovi, and S.Luding, editors, *Physics of Dry Granular Media*, page 441. Kluwer Academic Publishers, 1998.

[19] EngineersHandbook.com. Coefficient of friction reference table, 2012. [Online; accessed 12-January-2012].

[20] F.G.Bridges, A.Hatzes, and D. N. C.Lin. Structure, stability and evolution of saturn's rings. *Nature*, 309:333–335, May 1984.

[21] F.Radjai and S.Roux. Friction-induced self-organization of a one-dimensional array of particles. *Phys. Rev. E*, 51:6177, 1995.

[22] G.Baumann, I.Jánosi, and D.E.Wolf. Surface properties and flow of granular material in a twodimensional rotating drum model. *Phys. Rev. E*, 51:1879, 1995.

[23] G.H.Ristow. Particle mass segregation in a two-dimensional rotating drum. *Europhys. Lett.*, 28:97, 1994.

[24] G.H.Ristow. *Pattern Formation in Granular Media*. Springer-Verlag, 2000.

[25] G.Kuwabara and K.Kono. Restitution coefficient in a collision between two spheres. *Jpn. J. Appl. Phys*, 26:1230, 1987.

[26] G.Schliecker, Y.Khidas, M.Ammi, and J.-C.Messager. Collective response of an array of rotating particles to fluctuating confining forces. *Phys. Rev. E*, 62:744, 2000.

[27] G.Strassburger, A.Betat, M.A.Scherer, and I.Rehberg. Pattern formation by horizontal vibration of granular material. In D.E.Wolf, M.Schreckenberg, and A.Bachem, editors, *Workshop on Traffic and Granular Flow*, pages 329–334. World Scientific, October 9-11 1995.

[28] H.A.Makse and H.J.Herrmann. Microscopic model for granular stratification and segregation. *Europhys. Lett.*, 43:1, 1998.

[29] H.A.Makse, S.Havlin, P.R.King, and H.E.Stanley. Spontaneous stratification in granular mixtures. *Nature*, 386:379, 1997.

[30] H.Hertz. Über die Berührung fester elastischer Körper. *J. f. reine u. angewandte Math.*, 92:156, 1882.

[31] H.Kruggel-Emden, E.Simek, S.Rickelt, S.Wirtz, and V.Scherer. Review and extension of normal force modelsfor the discrete element method. *Powder Technology*, 171:157, 2007.

[32] H.Kuninaka and H.Hayakawa. Anomalous behavior of the coefficient of normal restitution in oblique impact. *Phys. Rev. Let.*, 93:154301, 2004.

[33] H.M.Jaeger, S.R.Nagel, and R.P.Behringer. The physics of granular materials. *Physics Today*, 49:32, 1996.

[34] I.Goldhirsch. Rapid granular flow. *Ann. Rev. Fluid Mech.*, 35:267, 2003.

[35] I.S.Aranson and L.S.Tsimring. Patterns and collective behaviour in granular media: Theoretical concepts. *Rev. Mod. Phys.*, 78:641, 2006.

[36] I.S.Aranson and L.S.Tsimring. *Granular Patterns.* Oxford University Press, 2009.

[37] J.B.Knight, E.E.Ehrichs, V.Yu.Kuperman, J.K.Flint, H.M.Jaeger, and S.R.Nagel. Experimental study of granular convection. *Phys. Rev. E*, 54:5726, 1996.

[38] J.B.Knight, H.M.Jaeger, and S.R.Nagel. Vibration induced size separation in granular media: The convection connection. *Phys. Rev. Lett.*, 70:3728, 1993.

[39] J.C.Williams. The segregation of particluate materials: A review. *Powder Technol.*, 15:245–251, 1976.

[40] J.Duran. *Sands, Powders, and Grains.* Springer-Verlag, 2000.

[41] J.Grimm and W.Grimm. *Kinder- und Hausmärchen*, volume 3. Reclam, 1986.

[42] H. J.Herrmann, G.Mantica, and D.Bessis. Space-filling bearings. *Phys. Rev. Lett.*, 65:3223, 1990.

[43] J.M.Haile. *Molecular Dynamics Simulation.* Wiley Professional Paperback Edition, 1997.

[44] J.M.Hill. The double-shearing velocity equations for dilatant shear-index granular materials. In N.A.Fleck and A.C.E.Cocks, editors, *Symposium on Mechanics of Granular and Porous Materials*, pages 251–262. Kluwer Academic Publishers, 1997.

[45] J.M.N.T.Gray and A.R.Thornton. A theory for particle size segregation in shallow granular free-surface flows. *Proc. R. Soc. Lond. A*, 461:1447, 2005.

[46] J.M.N.T.Gray and K.Hutter. Pattern formation in granular avalanches. *Continuum Mech. Thermodyn.*, 9:341, 1997.

[47] J.M.Ottino and D.V.Khakhar. Mixing and segregation of granular materials. *Ann. Rev. Fluid Mech.*, 32:55, 2000.

[48] J.P.Koeppe, M.Enz, and J.Kakalios. Phase diagram for avalanche stratification of granular media. *Phys. Rev. E*, 58:4104, 1998.

[49] J.Schäfer, S.Dippel, and D.E.Wolf. Force schemes in simulations of granular materials. *J. Phys. I France*, 6:5, 1996.

[50] K.Choo, T.C.A.Molteno, and S.W.Morris. Travelling granular segregation patterns in a long drum mixer. *Phys. Rev. Lett.*, 79:2975, 1997.

[51] K.Feitosa and N.Menon. Breakdown of energy equipartition in a 2d binary vibrated granular gas. *Phys. Rev. Lett.*, 88:198301, 2002.

[52] K.Saitoh, A.Bodrova, H.Hayakawa, and N.Brilliantov. Negative normal restitution coefficient found in simulation of nanocluster collisions. *Phys. Rev. Lett.*, 105:238001, 2010.

[53] L.D.Landau and E.M.Lifschitz. *Lehrbuch der theoretischen Physik 1: Mechanik.* Wissenschaftlicher Verlag Harri Deutsch, 14. edition edition, 2004.

[54] M.H.Cooke, D.J.Stephens, and J.Bridgwater. Powder mixing - a literature survey. *Powder Technol.*, 15:1, 1976.

[55] M.Montaine, M.Heckel, C.Krülle, and T.Schwagerand T.Pöschel. Coefficient of restitution as a fluctuating quantity. *Phys. Rev. E*, 84:041306, 2011.

[56] M.P.Allen, D.Frenkel, and J.Talbot. Molecular dynamics simulation using hard particles. *Computer Physics Reports*, 9:301–353, 1989.

[57] M.P.Allen and D.J.Tildesley. *Computer Simulation of Liquids.* Oxford University Press, 1987.

[58] M.P.Ciamarra, A.Conigli, and M.Nicodemi. Shear instabilities in granular mixtures. *Phys. Rev. Lett.*, 94:188001, 2005.

[59] M.P.Ciamarra, A.Coniglio, and M.Nicodemi. Phenomenology and theory of horizontally oscillated granular mixtures. *Europhys. J. E*, 22:227, 2007.

[60] M.Y.Louge and M.E.Adams. Anomalous behavior of normal kinematic restitution in the oblique impacts of a hard sphere on an elastoplastic plate. *Phys. Rev. E*, 65:021303, 2002.

[61] M. N.Bannerman, R.Sargant, and L.Lue. An $o(n)$ general event-driven simulator: DYNAMO. *J. Comp. Chem.*, in press, 2011.

[62] N.Burtally, P. J.King, M.R.Swift, and M. Leaper. Dynamical behaviour of fine granular glass/bronze mixtures under vertical vibration. *Granular Matter*, 5:57, 2003.

[63] N.Burtally, P.J.King, and M.R.Swift. Spontaneous air-driven separation in vertically vibrated fine granular mixtures. *Science*, 295:1877, 2002.

[64] N.V.Brilliantov, F.Spahn, J.M.Hertzsch, and T.Pöschel. A model for collisions in granular gases. *Phys. Rev. E*, 53:5382, 1996.

[65] N.V.Brilliantov and T.Pöschel. Rolling friction of a viscous sphere on a hard plane. *Europhys. Lett.*, 42(5):511, 1998.

[66] N.V.Brilliantov and T.Pöschel. *Kinetic Theory of Granular Gases*. Oxford Graduate Texts, 2004.

[67] O.Zik, D.Levine, S.G.Lipson, S.Shtrikman, and J.Stavans. Rotationally induced segregation of granular material in a horizontal rotating cylinder. *Phys. Rev. Lett.*, 73:644, 94.

[68] P.A.Cundall and O.D.L.Strack. A discrete numerical model for granular assemblies. *Géotechnique*, 29(1):47–65, March 1979.

[69] P.Gondret, M.Lance, and L.Petit. Bouncing motion of spherical particles in fluids. *Phys. Fluids*, 14:643, 2002.

[70] P.K.Haff and B.T.Werner. Computer simulation of the mechanical sorting of grains. *Powder Technol.*, 48:239, 1986.

[71] P.M.Reis, G.Ehrhardt, A.Stephenson, and T.Mullin. Gases, liquids and crystals in granular segregation. *Europhys. Lett.*, 66:357, 2004.

[72] P.M.Reis and T.Mullin. Granular segregation as a critical phenomenon. *Phys. Rev. Lett.*, 89:244301, 2002.

[73] P.M.Reis, T.Sykes, and T.Mullin. Phases of granular segregation in a binary mixture. *Phys. Rev. E*, 74:051306, 2006.

[74] P.Müller and T.Pöschel. Collision of viscoelastic spheres: Compact expressions for the coefficient of restitution. *Phys. Rev. E*, in press, 2011.

[75] P.Müller and T.Pöschel. Oblique impact of frictionless spheres- on the limitations of hard sphere models for granular dynamics. *Granular Matter*, submitted, 2012.

[76] P. P.Müller and T.Pöschel. *in preparation*, 2011.

[77] P.Sánchez, M.R.Swift, and P.J.King. Stripe formation in granular mixtures due to the differential influence of drag. *Phys. Rev. Lett.*, 93:184302, 2004.

[78] R.A.Bagnold. Experiments on a gravity-free dispersion of large solid spheres in a newtonian fluid under shear. *Proc. R. Soc. Lond. A*, 225:49, 1954.

[79] R.M.Iverson. The physics of debris flow. *Rev.Geophys.*, 35:245, 1997.

[80] S.Asakura and F.Oosawa. Interaction between particles suspended in solutions off macromolecules. *J. Polymer Sci.*, 33:183, 1958.

[81] S.B.Savage. Disorder, diffusion, and structure formation in granular flows. In D.Bideau and A.Hansen, editors, *Disorder and granular media*, volume 3, pages 255–285. North Holland, 1993.

[82] S.B.Savage and C.K.K.Lun. Particle size segregation in inclined chute flow of dry cohesionless granular solids. *J. Fluid Mech.*, 189:311, 1988.

[83] S.S.Hsiau and M.L.Hunt. Granular thermal diffusion in flows of binary-sized mixtures. *Acta Mechanica*, 114:121, 1996.

[84] T.Mullin. Coarsening of self-organized clusters in binary mixtures of particles. *Phys. Rev. Lett.*, 84:4741, 2000.

[85] T.Pöschel. *Dynamik granularer Systeme*. Humboldt-Universität zu Berlin, 1998.

[86] T.Pöschel and N.Brilliantov, editors. *Granular Gas Dynamics*. Lecture Notes in Physics. Springer, Berlin, 2003.

[87] T.Pöschel and T.Schwager. *Computational Granular Dynamics*. Springer-Verlag, 2005.

[88] T.Schwager and T.Pöschel. Coefficient of restitution and linear–dashpot model revisited. *Granular Matter*, 9:465, 2007.

[89] T.Schwager and T.Pöschel. Coefficient of restitution for viscoelastic spheres: The effect of delayed recovery. *Phys. Rev. E*, 78:051304–1, 2008.

[90] T.Tél and M.Gruiz. *Chaotic Dynamics*. Cambridge University Press, 2006.

[91] V.Becker, T.Schwager, and T.Pöschel. Coefficient of tangential restitution for the linear dashpot model. *Phys. Rev. E*, 77:011304, 2008.

[92] W.A.M.Morgado and I.Oppenheim. Energy dissipation for quasielastic granular particle collisions. *Phys. Rev. E*, 55:1940, 1997.

[93] W.Cooke, S.Warr, J.M.Huntley, and R.C.Ball. Particle size segregation in a two-dimensional bed undergoing vertical vibration. *Phys. Rev. Lett.*, 53:2812, 1996.

[94] Y.C.Zhou, B.D.Wright, R.Y.Yang, B.H.Xu, and A.B.Yu. Rolling friction in the dynamic simulation of sandpile formation. *Physica A*, 269:536, 1999.

[95] Y.Khidas, G.Schliecker, M.Ammi, J.-C.Messager, and R.Delannay. Rotational modes in a 1d array of cylinders under shear stress. *Europhys. Lett.*, 50:587, 2000.

Erklärung:
Hiermit versichere ich, dass ich diese Arbeit selbstständig und nur unter Verwendung der angegebenen Quellen und Hilfsmittel verfasst habe.

Erlangen, den 26.Januar 2012,
Dominik Krengel